Chemical Science

ROYAL SOCIETY OF CHEMISTRY

REVIEW

View Article Online
View Journal | View Issue



Cite this: *Chem. Sci.*, 2026, **17**, 7875

# Porous organic polymers based on carbon–carbon coupling reaction: synthesis and applications

Yifan Li, Jingyuan Zhao, Dongtao Liu * and Guangshan Zhu *

Porous organic polymers (POPs) are a class of materials formed by covalent bonding, which possess large specific surface area, good physical and chemical stability, and strong designability. Among these, POPs constructed through carbon–carbon coupling, including conjugated microporous polymers (CMPs), porous aromatic frameworks (PAFs), hypercrosslinked porous polymers (HCPs), and porous polymer networks (PPNs), generally show higher stability than those connected by reversible covalent bonds. These POPs can retain their structural stability even under harsh chemical conditions. This remarkable stability enables them to undergo diverse chemical functionalization modifications, thereby endowing them with broad application prospects that align more closely with practical requirements. Carbon–carbon coupling reactions are the core synthetic strategy for constructing POPs, mainly including classic reaction types such as Ullmann coupling, Sonogashira–Hagihara cross-coupling, Suzuki–Miyaura cross-coupling, Heck cross-coupling, Eglinton coupling, and Friedel–Crafts alkylation reaction. These reactions correspondingly enable the formation of five types of carbon–carbon bonds *via* coupling reactions, including $C(sp^2)$–C(sp), $C(sp^2)$–$C(sp^2)$, C(sp)–C(sp), $C(sp^2)$–$C(sp^3)$, and $C(sp^3)$–$C(sp^3)$. By precisely regulating monomer structures, catalyst systems, and reaction conditions, key parameters of POPs such as pore size, specific surface area, and surface chemical properties can be directionally designed, thereby obtaining material structures that meet specific application requirements. POPs have been attracting wide attention because of their excellent performances in gas adsorption, gas separation, catalysis, electrochemistry, and many other fields. Moving forward, carbon–carbon coupling reactions have unique potential in expanding the structural diversity of POPs and developing new functional porous materials, representing a promising direction for focused exploration in the field of POP synthesis.

Received 7th February 2026
Accepted 23rd March 2026

DOI: 10.1039/d6sc01090c

rsc.li/chemical-science



## 1 Introduction

In the dynamically evolving field of materials science, POPs have emerged as a class of functional materials with exceptional potential for application. POPs are a kind of organic porous material with microporous or mesoporous structures, typically composed of C, H, O, N, B, and other elements.[1] This distinctive composition imparts an array of advantageous properties, including excellent physical and chemical stability, large specific surface areas, intricate pore structures, low skeletal densities, and flexible frameworks. These characteristics place POPs at the forefront of research across diverse fields, such as gas adsorption, gas separation, catalysis, electrochemistry and other fields. POPs can be categorized based on their structural characteristics into several classes, including conjugated microporous polymers (CMPs),[2] porous aromatic frameworks (PAFs),[3] hypercrosslinked porous polymers (HCPs),[4] intrinsic microporous polymers (PIMs),[5] covalent organic frameworks (COFs),[6] and covalent triazine frameworks (CTFs).[7] Compared with metal–organic frameworks (MOFs), POPs exhibit particularly prominent advantages. Firstly, POPs possess excellent chemical stability. Their framework structures are mainly composed of covalent bonds with high bond energy, and this intrinsic characteristic endows the materials with superior chemical tolerance, enabling them to maintain the integrity and stability of the framework structure in harsh corrosive environments such as acids, alkalis, and organic solvents. Secondly, POPs have strong structural and functional designability. Benefiting from the diversity of organic synthetic chemistry, the building units and connection modes of POPs can be flexibly regulated. We can not only achieve the directional design of the framework structure through precise synthetic strategies, but also conveniently introduce specific functional groups, thereby realizing the accurate matching of "structure–function". In addition, POPs usually have lower density and higher specific surface area, which are crucial for applications such as gas adsorption, separation, and energy storage.

Based on the diversity of organic chemistry, there are numerous synthetic routes for the preparation of POPs. POPs constructed *via* carbon–carbon (C–C) coupling reactions exhibit remarkable advantages in the field of materials science, which

*Department of Chemistry, Northeast Normal University, Changchun, Jilin 130024, P. R. China. E-mail: liudt737@nenu.edu.cn; zhugs100@nenu.edu.cn*

are mainly reflected in their highly tunable structures, excellent stability, and broad application potential. Currently, the relevant carbon–carbon coupling reactions, such as C($sp^2$)–C(sp) coupling, C($sp^2$)–C($sp^2$) coupling, C(sp)–C(sp) coupling, C($sp^2$)–C($sp^3$) coupling, and C($sp^3$)–C($sp^3$) coupling, offer diverse strategies for constructing POPs with distinct structures and functions. The principal coupling reactions utilized in the preparation of POPs are the Sonogashira–Hagihara coupling reaction, Yamamoto-type Ullmann coupling reaction, Suzuki–Miyaura cross-coupling reaction, oxidative Eglinton coupling reaction, Glaser coupling reaction and so on. As a core synthetic strategy for constructing POPs, C–C coupling reactions have become the key technical support for advancing POPs from basic research to practical applications, owing to their advantages of high reaction controllability, broad structural regulation dimensions, and superior product stability.

Firstly, the C($sp^2$)–C(sp) coupling, represented by the Sonogashira–Hagihara cross-coupling reaction, enables the efficient synthesis of alkynyl-containing CMPs from aryl halide and terminal alkyne monomers under a palladium/copper salt catalytic system. Featuring mild reaction conditions and high selectivity, this reaction allows precise regulation of the specific surface area, pore structure, and gas adsorption performance of materials by adjusting chain length and functional groups. The resulting products exhibit excellent chemical stability and gas adsorption selectivity. For instance, the Cooper group first used 1,3,5-triethynylbenzene and 1,4-diiodobenzene as monomers to synthesize CMP-1 *via* this reaction; CMP-1 has a specific surface area of 834 $m^2\ g^{-1}$ and exhibits excellent performance in $H_2$ adsorption and $CO_2$ capture.[2] The C($sp^2$)–C($sp^2$) coupling, which includes Yamamoto-type Ullmann coupling, Suzuki–Miyaura cross-coupling, and others, serves as an important approach for constructing highly stable POPs. The Yamamoto-type Ullmann reaction uses $Ni(COD)_2$ as a catalyst and can construct rigid aromatic frameworks. For example, the PAF-1 synthesized by the Zhu group has a specific surface area of 5600 $m^2\ g^{-1}$ and a $H_2$ adsorption capacity of 7.0 wt% at 77 K and 48 bar, setting a record for POP hydrogen storage performance at that time.[3] The Suzuki–Miyaura reaction is renowned for its mild reaction conditions (room temperature to 100 °C) and broad substrate compatibility, enabling the targeted synthesis of functionalized POPs. For instance, PAF-70-$NH_2$, modified with amino groups, can efficiently immobilize large-sized catalysts, significantly improving catalyst utilization and cycling stability in heterogeneous catalysis.[8] The C(sp)–C(sp) coupling, centered on oxidative coupling and Glaser coupling, facilitates the polymerization of terminal alkyne monomers into alkynyl-linked CMPs under palladium/copper or copper salt catalysis. These products possess outstanding thermal stability and show significant potential in gas separation and photocatalysis. The Cooper group polymerized 1,3,5-triethynylbenzene into homo-coupled microporous polymers (HCMPs) *via* terminal alkyne oxidative self-coupling. HCPMs have a specific surface area exceeding 800 $m^2\ g^{-1}$ and exhibit $H_2$ adsorption capacities of 107 $cm^3\ g^{-1}$ and 131 $cm^3\ g^{-1}$, respectively, at 77.3 K and 1.13 bar, demonstrating promising gas storage potential.[9] Glaser coupling, using CuCl as a catalyst and pyridine as a base, enables low-cost synthesis of butadiynyl-based CMPs. For example, TPM-BD-CMP achieves a $CO_2$ adsorption capacity of 3.78 mmol $g^{-1}$ at 273 K and 1 bar and possesses *in situ* gel-forming properties, facilitating material processing and application.[10] The C($sp^2$)–C($sp^3$) coupling, exemplified by the Friedel–Crafts alkylation reaction, constructs HCPs through the coupling of aromatic hydrocarbons and haloalkanes. This method offers abundant raw materials, mild reaction conditions, and flexible regulation of material pore structures, demonstrating excellent performance in gas storage and pollutant adsorption. The "solvent knitting" strategy developed by the Tan group is based on this reaction. The resulting SHCP-3 achieves a $CO_2$ adsorption capacity of 4.84 mmol $g^{-1}$ at 273 K and 1 bar, the highest value reported so far in the HCP field. Additionally, this method uses readily available raw materials and mild reaction conditions, showing potential for large-scale production.[11] The C($sp^3$)–C($sp^3$) coupling was previously limited by the low reactivity of $sp^3$-hybridized carbons. However, recent breakthroughs in nickel bis(1,5-cyclooctadiene) ($Ni(COD)_2$) or sodium catalytic systems have successfully enabled its application in POP synthesis. This has led to the preparation of highly crystalline linear polymers, flexible PAFs (*e.g.*, PAF-64/65/66),[12] and pure alkane-based porous polyadamantane (PPA), which exhibit exceptional performance in methane storage and alkane separation.

POPs prepared *via* C–C coupling reactions have demonstrated excellent application performance in multiple fields. In gas adsorption, PPN-4 achieves a $H_2$ adsorption capacity of 8.34 wt% at 77 K and 55 bar,[13] owing to its large specific surface area and well-defined pore structure. POPs also hold broad development prospects in the field of gas separation. NUT-15 has a $CO_2/CH_4$ selectivity of 12.4 (273 K). Through pore chemistry modification,[14] iPAF-28 achieves a $C_2H_2/C_2H_4$ selectivity of 15.4, far exceeding that of unmodified PAF-28 (1.8).[15] In catalysis, CP-CMP10, the first organic photocatalyst for hydrogen evolution driven primarily by visible light, exhibits a hydrogen evolution rate under visible light 30 times higher than that under ultraviolet light;[16] FeP-CMP achieves a turnover number (TON) of 97 320 in thioether oxidation reactions and can be scaled up to gram-level applications.[17] In electrochemistry, GeDA,[18] used as an anode for sodium-ion batteries, delivers a specific discharge capacity of 349 mAh $g^{-1}$ at 200 mA $g^{-1}$ and retains 112 mAh $g^{-1}$ after 5000 cycles at 5 A $g^{-1}$. The PAF-142-based composite electrolyte has a $Li^+$ conductivity of $8.77 \times 10^{-4}$ S $cm^{-1}$, enabling stable cycling of symmetric batteries for 8500 cycles.[19]

The research on POPs based on carbon–carbon coupling reactions is a rapidly expanding and highly promising field. In recent years, scholars have made significant contributions to the research on the construction of porous organic polymer *via* C–C coupling reactions. This review aims to comprehensively summarize the recent progress in the synthesis, properties, and applications of POPs prepared by carbon–carbon coupling reactions, providing valuable insights for further research and development in this field.

## 2 Design principles and synthesis of POPs

POPs, as a class of multifunctional materials, have found extensive applications in gas adsorption, catalysis, energy storage, and other fields. Their synthesis primarily relies on C–C coupling reactions (Fig. 1). This review systematically summarizes the applications and characteristics of five key types of C–C coupling reactions in the synthesis of POPs. Various C–C coupling reactions provide versatile tools for the structural design and functional regulation of POPs. Future research will focus on optimizing catalytic systems, expanding the range of monomers, and promoting the practical application of these materials in energy and environmental fields.

### 2.1 C($sp^2$)–C(sp) coupling reaction

The construction of POPs *via* C($sp^2$)–C(sp) coupling reactions represents a research hotspot and key direction in the field of materials science.[20–22] Their synthetic strategies feature high flexibility, enabling precise regulation of the molecular structure, pore size distribution, and chemical properties of the materials (Table 1). By virtue of the coupling reaction between $sp^2$-hybridized carbon atoms and sp-hybridized carbon atoms, such POPs usually incorporate alkynyl functional units, thereby forming rigid porous network structures with high specific surface area, excellent thermochemical stability, and well-defined chemical composition. Among the construction methods for such POPs, the Sonogashira–Hagihara cross-coupling reaction is widely applied and highly efficient. It can selectively introduce alkynyl bonds, facilitate the formation of highly cross-linked porous frameworks among molecular chains, and serve as one of the core approaches for preparing such materials. Typically, this reaction uses aryl halides (or alkenyl halides) and terminal alkynes as substrates, proceeding in a system consisting of a palladium catalyst (*e.g.*, tetrakis(triphenylphosphine)palladium, $Pd[P(C_6H_5)_3]_4$) as the core catalytic component, a copper salt (*e.g.*, CuI) as the cocatalyst, and an organic amine (*e.g.*, triethylamine, piperidine) as the base, ultimately yielding aryl alkynes (or alkenyl alkynes) as products (Fig. 2a). Owing to its mild reaction conditions and excellent selectivity, this reaction has become an important technical route for synthesizing alkynyl-functionalized POPs. The aforementioned unique structural and physicochemical properties endow these POPs with outstanding application performance in multiple cutting-edge technological fields, demonstrating broad application prospects. In the field of gas adsorption and separation, these POPs act as efficient $CO_2$ capture materials by virtue of their tunable pore sizes and abundant alkynyl active sites, enabling the high-efficiency separation and purification of mixed gases such as $CO_2/N_2$ and olefins, and thus holding significant application value in the field of low-carbon environmental protection. In the field of catalysis, as high-performance heterogeneous catalyst supports or catalytic active centers, these POPs play a crucial role in photocatalysis, heterogeneous catalysis, and electrochemical catalysis. In particular, they exhibit unique advantages and enormous application potential in reactions such as $CO_2$ resource conversion and fine organic synthesis. In addition, benefiting from their porous structure and functionalizable modification characteristics, these POPs also show highly attractive application prospects in interdisciplinary fields including environmental remediation (*e.g.*, efficient removal of pollutants from water and soil), energy storage (*e.g.*, electrode materials for lithium-ion batteries and supercapacitors), and biomedicine (*e.g.*, targeted drug delivery and biosensing), emerging as an important material platform for interdisciplinary research across multiple fields.

In 2007, Cooper *et al.*[2] successfully synthesized a series of CMPs (CMP-1 to CMP-4) *via* palladium-catalyzed Sonogashira–Hagihara cross-coupling reaction (Fig. 2b), confirming that ordered structure is not a prerequisite for the precise regulation

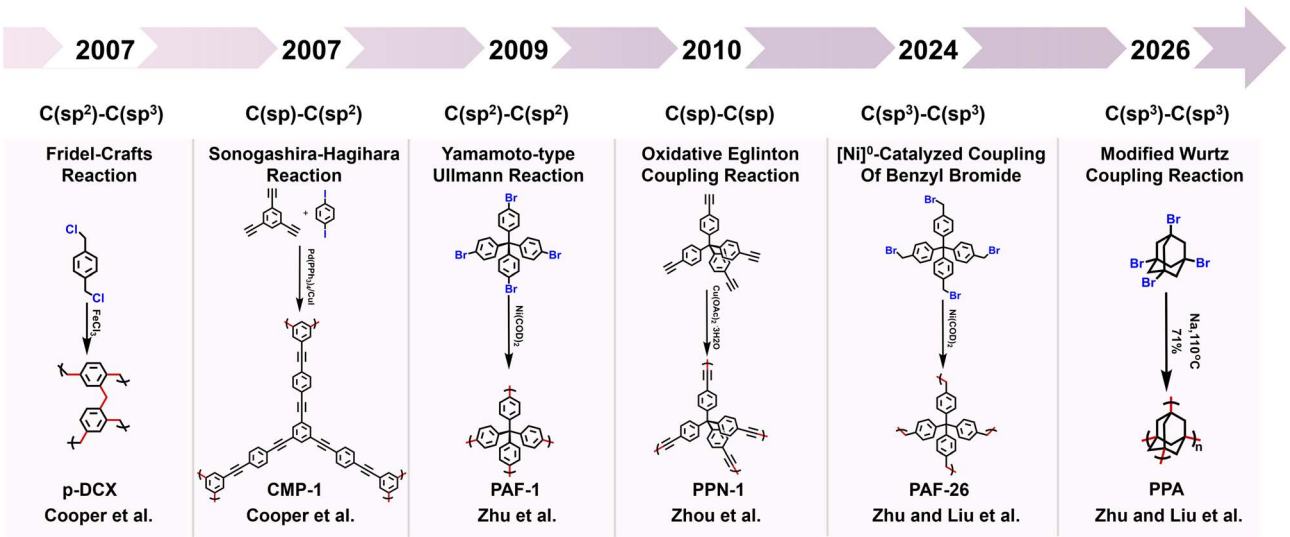


Fig. 1 Timeline of POPs constructed by carbon–carbon coupling reactions.

Table 1 A summary of building units and frameworks using C($sp^2$)–C(sp) coupling

| Common name | Building units | | Proposed structures | Ref. |
|---|---|---|---|---|
| CMP-0 | 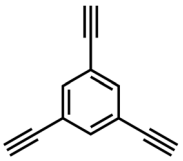 | 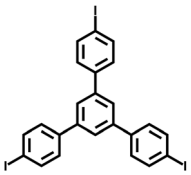 | 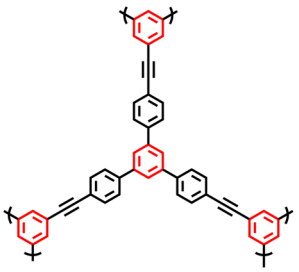 | 24 |
| CMP-1 | 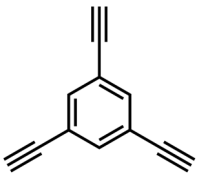 | 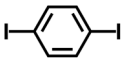 | 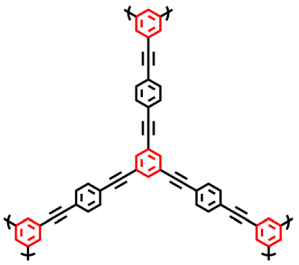 | 2 |
| CMP-2 | 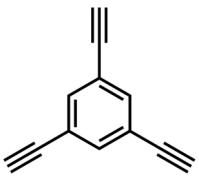 | 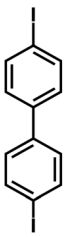 | 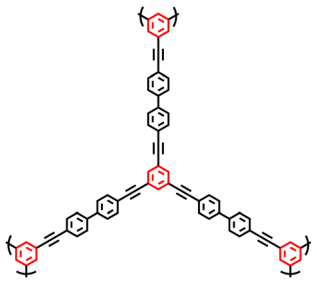 | 2 |
| CMP-3 | 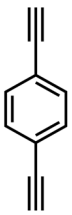 | 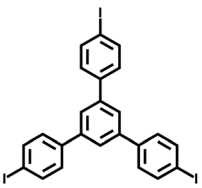 | 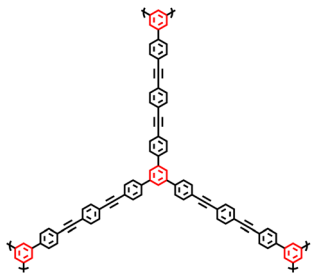 | 2 |
| CMP-4 | 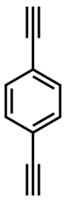 | 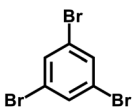  | 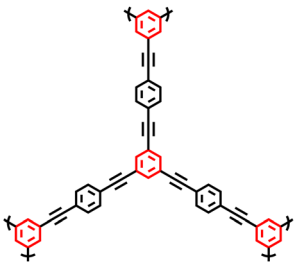 | 2 |
| CMP-5 | 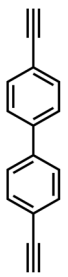 | 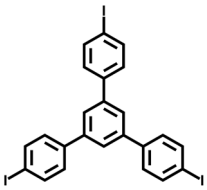 | 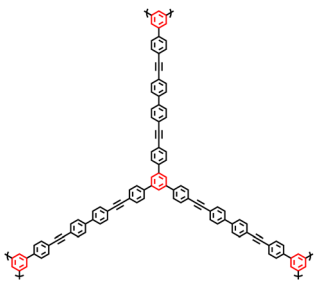 | 24 |

Table 1 (*Contd.*)

| Common name | Building units | | Proposed structures | Ref. |
|---|---|---|---|---|
| NCMP-0 | 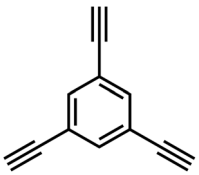 | 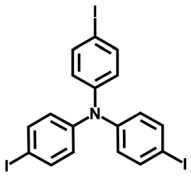 | 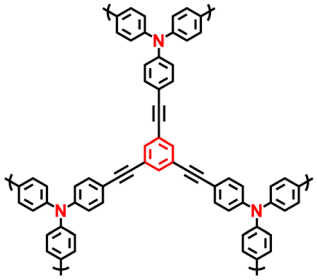 | 25 |
| NCMP-1 | 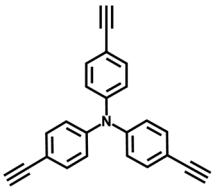 | 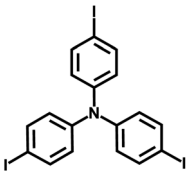 | 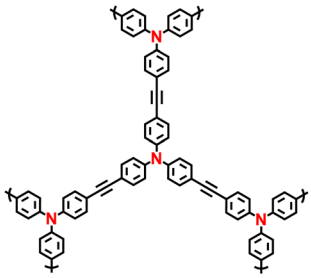 | 25 |
| NCMP-2 | 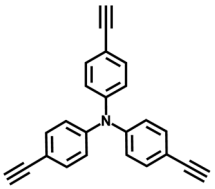 | 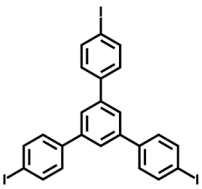 | 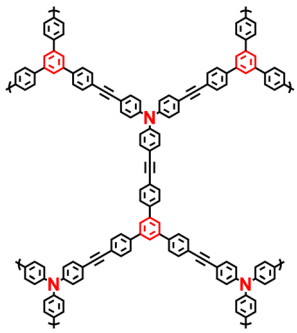 | 25 |
| NCMP-3 | 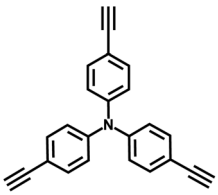 | 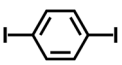 | 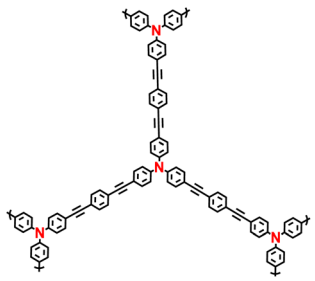 | 25 |
| NCMP-4 | 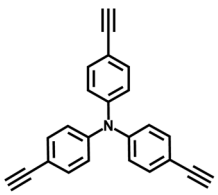 | 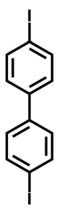 | 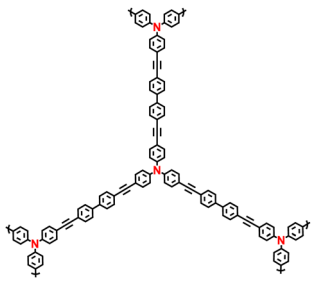 | 25 |

Table 1 (*Contd.*)

| Common name | Building units | | Proposed structures | Ref. |
|---|---|---|---|---|
| PAF-18-OH<br>PAF-18-OLi | 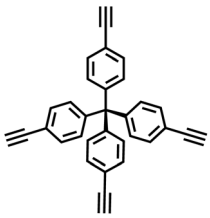 | 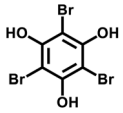 | 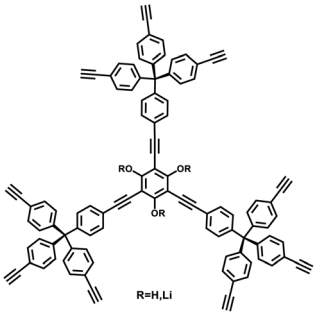 | 26 |
| PAF-19 | 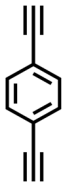 | 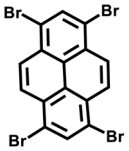 | 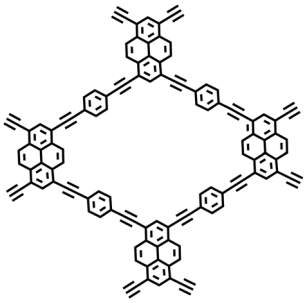 | 27 |
| PAF-20 | 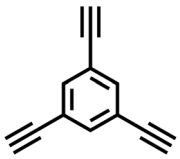 | 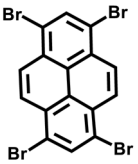 | 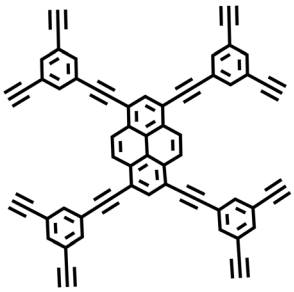 | 27 |
| PAF-23 |  | 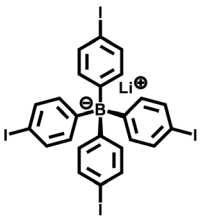 | 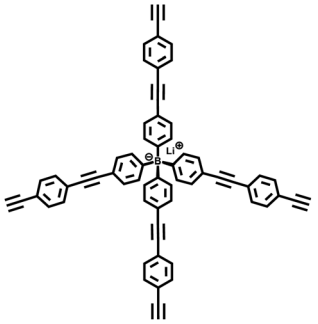 | 28 |
| PAF-24 | 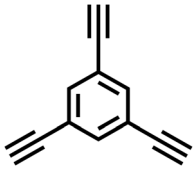 | 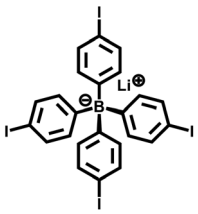 | 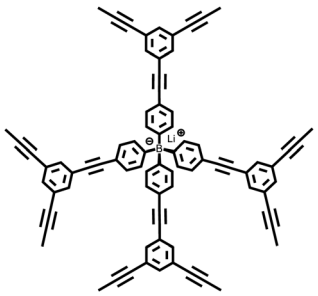 | 28 |

Table 1 (*Contd.*)

| Common name | Building units | | Proposed structures | Ref. |
|---|---|---|---|---|
| PAF-25 | 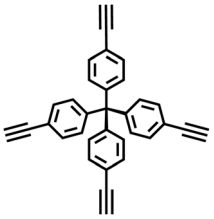 | 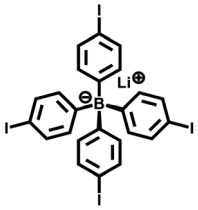 | 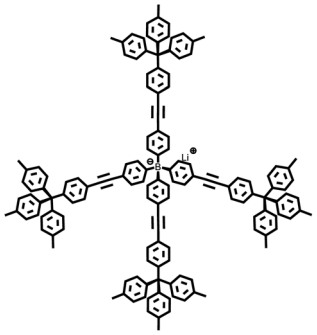 | 28 |
| PAF-26-COOH | 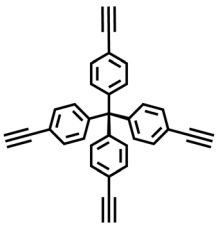 | 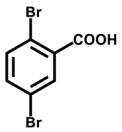 | 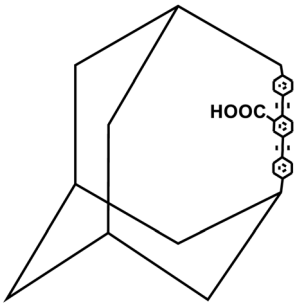 | 29 |
| PAF-28 | 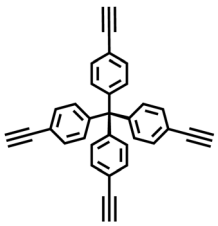 | 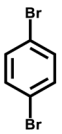 | 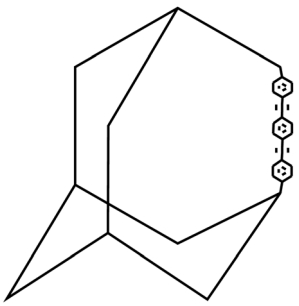 | 15 |
| cPAF-28<br>iPAF-28 | 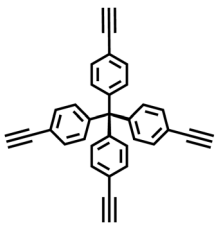 | 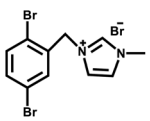 | 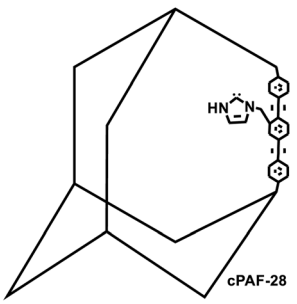 <br> 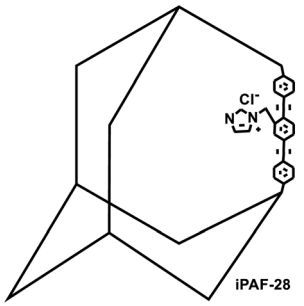 | 15 |

Table 1 (*Contd.*)

| Common name | Building units | | Proposed structures | Ref. |
|---|---|---|---|---|
| PAF-33 | 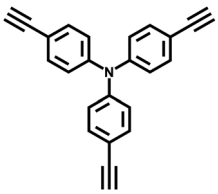 | 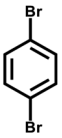 | 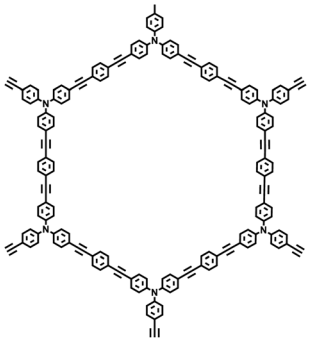 | 30 |
| PAF-34 | 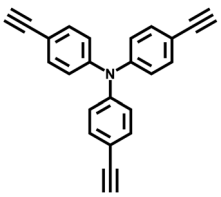 | 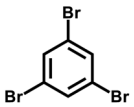 | 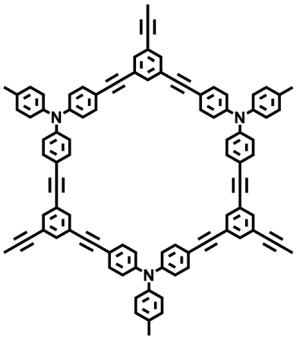 | 30 |
| PAF-35 | 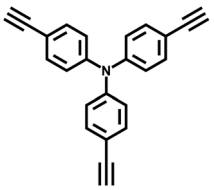 | 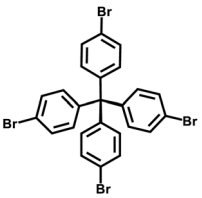 | 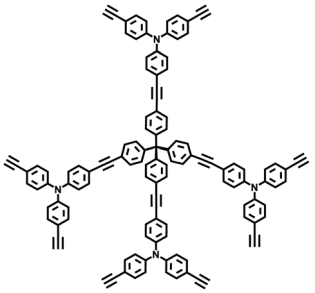 | 30 |
| PAF-79<br>PAF-80 | 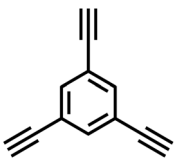 | 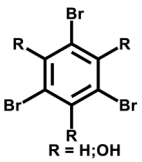 | 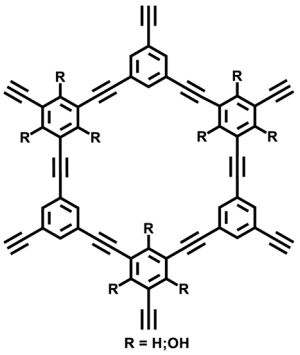 | 31 |

Table 1 (*Contd.*)

| Common name | Building units | Proposed structures | Ref. |
|---|---|---|---|
| NUT-15 | 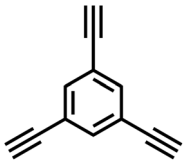 | 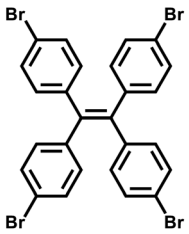 | 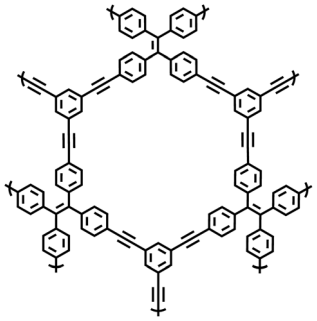 | 14 |

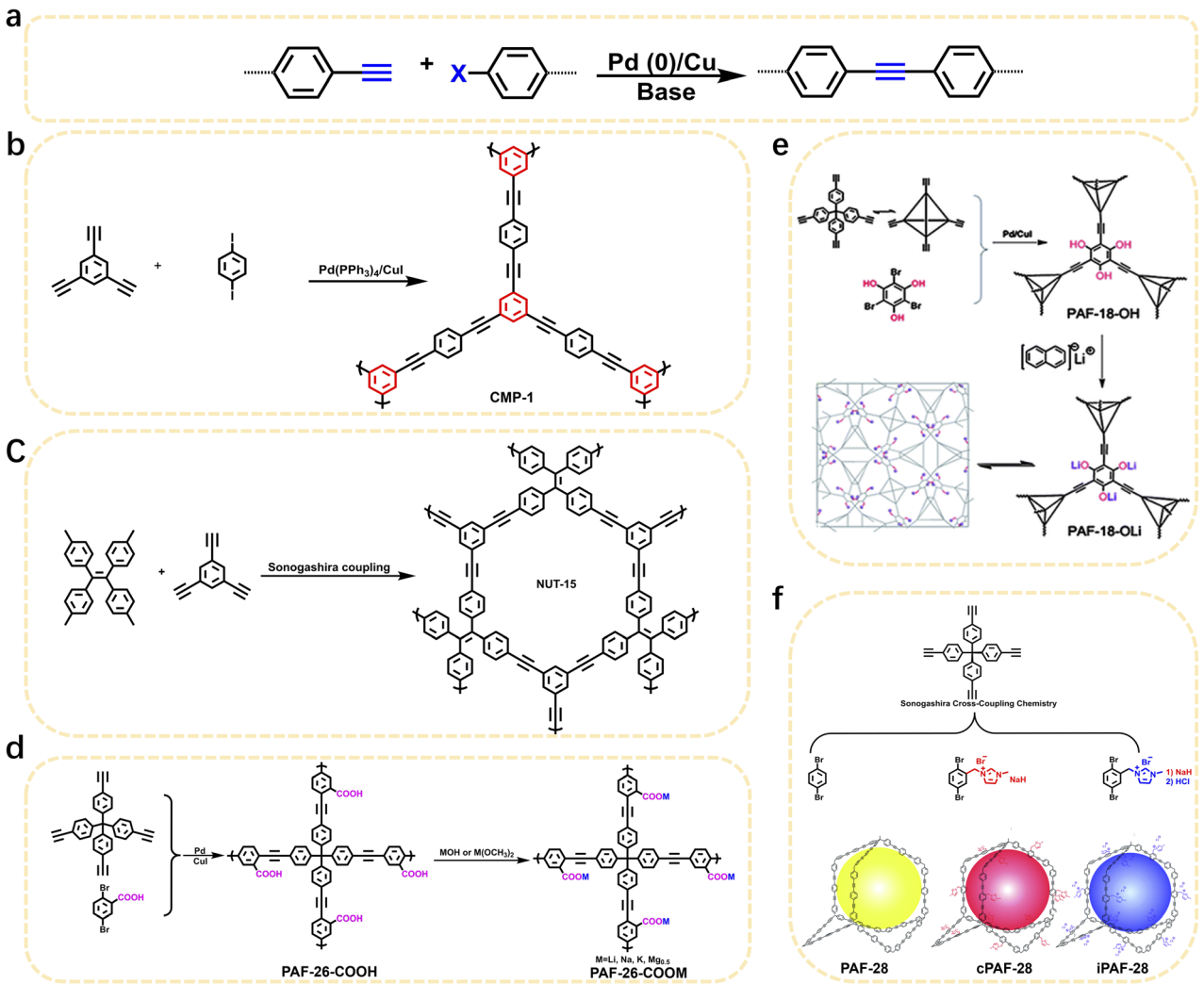


Fig. 2 (a) Sonogashira–Hagihara reaction for the synthesis of porous frameworks. (b) The synthesis of CMPs.[2] Copyright 2007 Wiley-VCH GmbH. (c) Chemical structures of used monomers and the CMPs (NUT-14 and NUT-15).[14] Copyright 2018 American Chemical Society. (d) Schematic representation of the synthesis of PAF-26-COOH and PAF-26-COOM.[29] Copyright 2014 the Royal Society of Chemistry. (e) Schematic depiction of the synthesis of PAF-18-OH and PAF-18-OLi.[26] Copyright 2013 the Royal Society of Chemistry. (f) Schematic representation of the synthesis of PAF-28, cPAF-28 and iPAF-28.[15] Copyright 2022 the Royal Society of Chemistry.

of microporous properties in organic networks. These polymers are constructed with 1,3,5-substituted benzene as nodes and rigid phenyleneethynylene as connecting struts. By adjusting the length of the connecting struts, the micropore size distribution and specific surface area can be systematically tuned ($S_{BET}$ ranges from 522 to 834 $m^2\ g^{-1}$), with the pore diameter shifting toward a larger range as the strut length increases. Compared with MOFs and COFs, CMPs are composed solely of carbon–carbon (C–C) and carbon–hydrogen (C–H) bonds, exhibiting superior thermal stability ($T_d$ > 400 °C) and chemical stability. Integrating conjugated structures with microporous characteristics, CMP-1 also demonstrates photoluminescent properties, thereby providing a novel approach for the design of multifunctional microporous materials. Building on this achievement, Cooper *et al.*[24] further explored the potential of the Sonogashira–Hagihara reaction, synthesizing another series of CMPs. These materials maintain outstanding chemical and thermal stability under various conditions and preserve their microporosity even in harsh environments. Among them, CMP-0 featuring the shortest linking group, possesses the highest specific surface area of 1018 $m^2\ g^{-1}$, while CMP-5, with the longest linking group, has the lowest specific surface area of 512 $m^2\ g^{-1}$. These results show that the physical properties of CMPs, such as pore size, pore volume, specific surface area and hydrogen adsorption capacity, can be effectively regulated by changing the length of the linking monomer struts. Since then, this novel type of POPs has quickly attracted widespread attention from researchers, and the design and synthesis of functionalized CMPs have gradually become a research hotspot. In 2009, the research team advanced the field by introducing N heteroatoms into the CMPs and synthesized a series of functionalized nitrogen-containing NCMPs *via* the Sonogashira–Hagihara coupling reaction.[25] This study revealed that the $S_{BET}$ (ranging from 546 to 1108 $m^2\ g^{-1}$), micropore surface area (ranging from 327 to 825 $m^2\ g^{-1}$), and micropore volume (ranging from 0.20 to 0.51 $m^3\ g^{-1}$) of the NCMPs could be adjusted by varying the lengths of the synthetic monomers. Additionally, triphenylamine, a well-known organic optoelectronic molecule, is incorporated into the CMP skeleton, indicating that the prepared NCMPs hold potential application value in the field of optoelectronics. Sun *et al.*[14] successfully developed NUT-15 by copolymerizing 1,3,5-triynylbenzene and tetrakis(4-bromophenyl)ethylene *via* the Sonogashira–Hagihara cross-coupling reaction (Fig. 2c). NUT-15 exhibits exceptional $CO_2$ adsorption capacity and a high $CO_2/CH_4$ adsorption selectivity of 12.4 at 273 K. Temperature-controlled carbonization of NUT-15 results in the formation of (porous carbons) PCs with high carbonization yield (78–85%), large surface area (800–1700 $m^2\ g^{-1}$), and plentiful micropores. Among the PCs investigated, PC-800 exhibits a maximum $CO_2$ uptake of 5.4 mmol $g^{-1}$ at 273 K and 1 bar, which is obviously much higher than reported benchmarks including activated carbon (2.8 mmol $g^{-1}$).

Moreover, the C($sp^2$)–C(sp) coupling reaction has extensive applications in the synthesis of PAFs. Zhu *et al.*[26] synthesized novel PAFs (PAF-18-OH and PAF-18-OLi) *via* the Sonogashira–Hagihara cross-coupling reaction in 2013 (Fig. 2d). Both PAF-18-OH and PAF-18-OLi exhibit exceptional gas adsorption properties. Specifically, PAF-18-OH exhibits a $H_2$ uptake of 1.35 wt% at 77 K and 1 bar and a $CO_2$ uptake of 110 mg $g^{-1}$ at 273 K and 1 bar, while PAF-18-OLi shows higher capacities and demonstrates a $H_2$ uptake of 1.65 wt% at 77 K and 1 bar, with a $CO_2$ uptake of 144 mg $g^{-1}$ at 273 K and 1 bar. Notably, PAF-18-OLi exhibits a remarkable $CO_2/N_2$ adsorption selectivity of 129. Subsequently, they successfully synthesized pyrene-based fluorescent PAF-19 and PAF-20, employing 1,3,6,8-tetrabromopyrene as the building unit, by coupling it with 1,4-diethynylbenzene and 1,3,5-triethynylbenzene through the Sonogashira–Hagihara cross-coupling reaction.[27] These PAFs exhibit excellent thermal and chemical stability, along with high $H_2$ and $CO_2$ adsorption performance. Specifically, PAF-19 shows a $CO_2$ adsorption capacity of 20.1 $cm^3\ g^{-1}$ at 273 K and 1 bar, while PAF-20 demonstrates a higher capacity of 25.9 $cm^3\ g^{-1}$ at 273 K and 1 bar. Furthermore, both PAF-19 and PAF-20 possess favorable adsorption selectivity, making them promising candidates for water pollutant removal. On this basis, Zhu *et al.*[28] successfully synthesized PAF-23, PAF-24, and PAF-25 *via* the Sonogashira–Hagihara coupling reaction between lithium tetrakis(4-iodophenyl)borate and various alkyne monomers. These polymers exhibit high thermal and chemical stability, along with significant iodine adsorption capacities (2710 mg $g^{-1}$, 2760 mg $g^{-1}$, and 2600 mg $g^{-1}$, respectively). Subsequently, they further synthesized carboxyl-modified PAF-26-COOH ($S_{BET}$ = 717 $m^2\ g^{-1}$) through this reaction (Fig. 2e), which features high porosity and accessible carboxyl groups, enhancing gas–solid interactions.[29] PAF-26-COOH exhibits a high volumetric $CO_2$ adsorption capacity of 286 mg $cm^{-3}$ and favorable $CO_2/CH_4$ adsorption selectivity. Inspired by these findings, Zhu *et al.*[30] synthesized a series of PAFs (PAF-33, PAF-34, and PAF-35) for $CO_2$ capture, incorporating functional groups (such as –COOH, $–NH_2$, and –OH) into the main chain of the PAF material. These PAF materials show high stability and moderate specific surface areas (370–953 $m^2\ g^{-1}$). Notably, PAF-34 exhibits a $CO_2$ uptake of 2.5 mmol $g^{-1}$ at 273 K, and PAF-33 demonstrates an impressive $CO_2/N_2$ adsorption selectivity of 250.5. The incorporation of $CO_2$-philic functional groups (such as –COOH, $–NH_2$, and –OH) into the framework can effectively enhance the interaction between the material and $CO_2$, improve its $CO_2$ capture capacity, selectivity and affinity, and provide an effective strategy for the development of high-performance carbon dioxide capture and sequestration materials.

In addition, PAF-79, PAF-80, and PAF-80-$SO_3H$ were synthesized *via* the Sonogashira–Hagihara cross-coupling reaction, exhibiting specific surface areas of 1964 $m^2\ g^{-1}$, 768 $m^2\ g^{-1}$, and 200 $m^2\ g^{-1}$, respectively.[31] The incorporation of $–SO_3H$ groups endows PAF-80-$SO_3H$ with significantly enhanced pore polarity, enabling it to adsorb ionic compounds in water, with a water absorption capacity of 226 $cm^3\ g^{-1}$, while neutral organic molecules are preferentially adsorbed by the moderately polar porous material PAF-80. Furthermore, it reveals that when PAF materials are applied to water treatment and purification, the specific surface area is less important than pore polarity and surface wettability. This work provides insights into polarity engineering and surface wettability control in the field of water

contaminant capture. Recently, Zhu and Liu *et al.* designed a parent material affording non-functionalized PAF-28 *via* the Sonogashira coupling reaction of tetrakis(4-ethynylphenyl) methane with 1,4-dibromobenzene (Fig. 2f).[15] The specific surface area of PAF-28 is 452 $m^2 g^{-1}$, while those of cPAF-28 and iPAF-28 are slightly lower, at 273 $m^2 g^{-1}$ and 282 $m^2 g^{-1}$, respectively, due to the occupation of pore space by functional groups. By introducing carbene or imidazolium functional groups into PAFs, the pore chemistry (such as basicity and pore size) can be tailored, significantly enhancing the $C_2H_2/C_2H_4$ separation performance. At 273 K and 100 kPa, iPAF-28 exhibits the highest $C_2H_2$ adsorption capacity (57 $cm^3 g^{-1}$), followed by cPAF-28 (48 $cm^3 g^{-1}$). The $C_2H_2/C_2H_4$ selectivities are 15.4 and 12.2, respectively, much higher than that of PAF-28 (1.8). These materials provide efficient options for industrial-scale $C_2H_2/C_2H_4$ separation and offer new insights into achieving specific molecular recognition through pore chemistry design.

### 2.2 $C(sp^2)$–$C(sp^2)$ coupling reaction

POPs, as a class of important materials in the field of materials science, can be constructed *via* $C(sp^2)$–$C(sp^2)$ coupling reactions. Such POPs form stable covalent bonds through the coupling of $sp^2$-hybridized carbon atoms, yielding organic network materials with unique porous structures (Table 2). The core of this synthetic strategy lies in the precise regulation of monomer selection and coupling reaction conditions to achieve accurate customization of the polymer's pore size, specific surface area, and chemical properties. In the field of POPs preparation, various $C(sp^2)$–$C(sp^2)$ coupling reactions have been reported, including Yamamoto-type Ullmann coupling, Suzuki–Miyaura cross-coupling, and Heck cross-coupling (Scheme 1).

The Yamamoto coupling reaction, also known as the Yamamoto polymerization, was first reported in 1978 by Japanese chemist Takakazu Yamamoto.[32] This reaction typically uses transition metals as catalysts (such as $NiCl_2$(bipy), $Ni(COD)_2$, *etc.*) to enable intermolecular coupling of dihaloarenes or polyhaloarenes, forming polyarenes. It is widely used in the synthesis of PAFs and CMPs. The Yamamoto-type Ullmann coupling reaction is an important organic synthesis reaction developed on the basis of the classical Ullmann coupling reaction. In the presence of transition metal catalysts (such as $Pd(PPh_3)_4$) and bases (such as cesium carbonate, potassium phosphate, *etc.*), aryl halides (such as aryl bromides, aryl iodides) react with another aryl compound (such as arylboronic acids, aryltin reagents and other aryl nucleophiles) to form biaryl compounds. This reaction realizes the formation of carbon–carbon bonds through a catalytic cycle, providing an efficient method for organic synthesis. Compared with the classical Ullmann coupling, the Yamamoto-type Ullmann coupling uses transition metal catalysts such as palladium and nickel, and the reaction conditions are milder, which can be carried out at lower temperatures. This optimization of reaction conditions reduces the occurrence of side reactions and improves the compatibility of functional groups. The Suzuki–Miyaura coupling reaction can also be used to prepare CMPs, which possess both excellent conjugation properties and stable microporous structures. Such POPs generally exhibit a high specific surface area, outstanding thermal stability, chemical stability, mechanical stability, and abundant active sites, endowing them with broad application potential in multiple cutting-edge fields.

In 2009, Zhu *et al.* employed the Ni(0)–catalyzed Yamamoto-type Ullmann coupling reaction to achieve the carbon–carbon coupling polymerization of the tetrakis(4-bromophenyl) methane monomer, resulting in the synthesis of PAF-1 (Fig. 3a).[3] PAF-1 not only exhibits an exceptionally high specific surface area of 5600 $m^2 g^{-1}$ but also demonstrates excellent chemical stability and thermal resistance ($T_d$ = 520 °C). Its $H_2$ adsorption capacity reaches 7.0 wt% at 77 K and 48 bar, while the $CO_2$ adsorption capacity can be as high as 1.30 g $g^{-1}$ at 298 K and 40 bar. Subsequently, Qiu *et al.* introduced silicon (Si) and germanium (Ge) heteroatoms into the framework of PAF-1, resulting in PAF-3 and PAF-4 with specific surface areas of 2932 $m^2 g^{-1}$ and 2246 $m^2 g^{-1}$, respectively.[33] Moreover, their $H_2$ adsorption capacity reach 2.1 wt% and 1.5 wt%, respectively, at 77 K and 1 atm. Later on, the Zhu group employed the similar synthetic method to prepare PAF-5, which demonstrated good thermal and chemical stability along with a large specific surface area of 1503 $m^2 g^{-1}$, enabling excellent gas adsorption performance (Fig. 3b).[34] PAF-5 can adsorb large amounts of methanol, benzene, and toluene, with values of 653.09 $cm^3 g^{-1}$ (29.16 mmol $g^{-1}$), 262.96 $cm^3 g^{-1}$ (11.74 mmol $g^{-1}$), 258.22 $cm^3 g^{-1}$ (11.53 mmol $g^{-1}$), respectively, at saturated vapour pressures and room temperature. These excellent sorption performances of PAF-5 promise great potential for dealing with environmental problems. In 2018, the same group synthesized PAF-100 ($S_{BET}$ = 5501 $m^2 g^{-1}$) and PAF-101 ($S_{BET}$ = 5114 $m^2 g^{-1}$), both characterized by ultra-large specific surface areas.[35] These materials achieved high $CH_4$ adsorption capacities of 742 $cm^3 g^{-1}$ and 622 $cm^3 g^{-1}$, respectively, at 298 K and 70 bar, highlighting their potential in natural gas storage and transportation applications.

Ben *et al.* utilized a $Ni(COD)_2$-catalyzed Yamamoto-type Ullmann coupling reaction to facilitate the polymerization of tris(4-bromophenyl)amine, successfully synthesizing JUC-Z2 and JUC-Z4 (Fig. 3c).[36,37] Composed of electron-rich secondary structural units and robust covalent bonds, JUC-Z2 exhibits excellent thermal stability (up to 430 °C) and a large surface area. Electron-rich aromatic blocks and the nitrogen atom with a lone pair of electrons render JUC-Z2 a Lewis base, enabling strong interactions with electron-deficient $CO_2$. The $CO_2$ uptake of JUC-Z2 was 71 $cm^3 g^{-1}$ at 273 K and 760 mmHg. Moreover, the high electron density of the structure promotes significant H–π interactions between $CH_4$ and JUC-Z2, endowing JUC-Z2 with high $CH_4$ absorption of 25 $cm^3 g^{-1}$ at 273 K and 760 mmHg and favorable adsorption selectivity. The $H_2$, $CO_2$, $CH_4$ storage capabilities of electron-rich aromatic framework JUC-Z2 make it highly promising for applications in addressing greenhouse gas pollution-related environmental issues. In contrast, JUC-Z4 demonstrates remarkable physical and chemical stability, a reversible redox state, and a controllable high specific surface area ($S_{BET}$ = 2034 $m^2 g^{-1}$). The $H_2$ uptake of JUC-Z4 was 142 $cm^3 g^{-1}$ at 77 K and 760 mmHg, and the $CH_4$

Table 2 A summary of building units, frameworks, and the corresponding synthetic using $C(sp^2)–C(sp^2)$ coupling

| Common name | Building units | Reactions | Proposed structures | Ref. |
|---|---|---|---|---|
| PAF-1 | 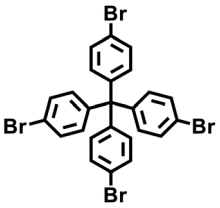 | Yamamoto-type Ullmann coupling | 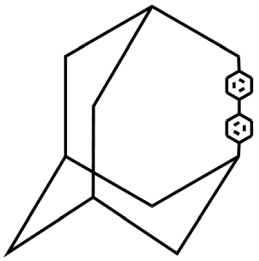 | 3 |
| PAF-3 | 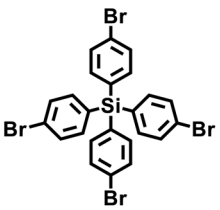 | Yamamoto-type Ullmann coupling | 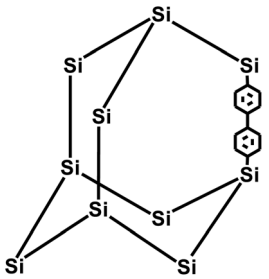 | 33 |
| PAF-4 | 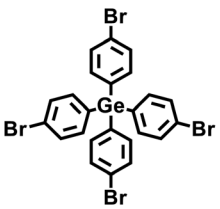 | Yamamoto-type Ullmann coupling | 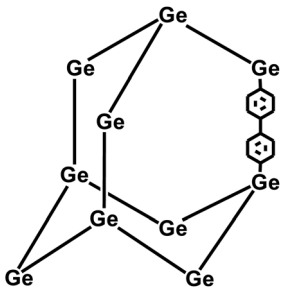 | 33 |
| PAF-5 | 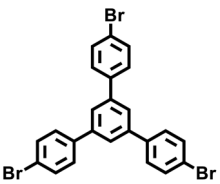 | Yamamoto-type Ullmann coupling | 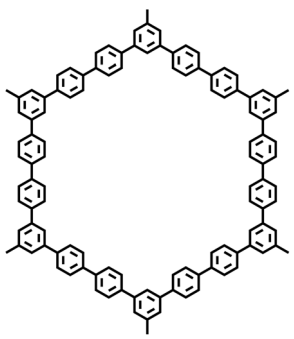 | 34 |
| JUC-Z2 | 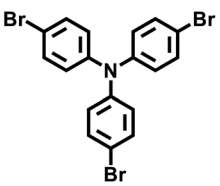 | Yamamoto-type Ullmann coupling | 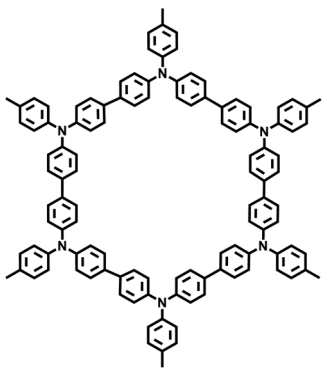 | 36 |

Table 2 (*Contd.*)

| Common name | Building units | Reactions | Proposed structures | Ref. |
|---|---|---|---|---|
| JUC-Z4 | 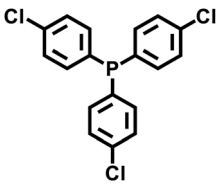 | Yamamoto-type Ullmann coupling | 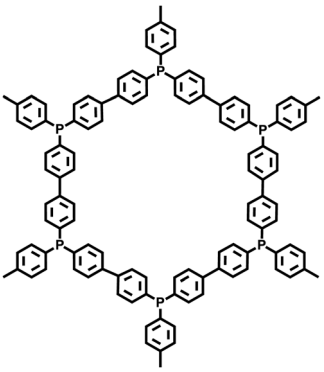 | 37 |
| PPN-3 | 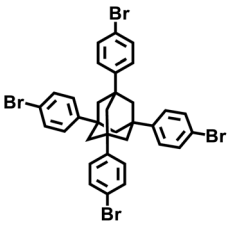 | Yamamoto-type Ullmann coupling | 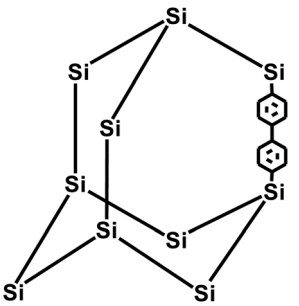 | 13 |
| PPN-4 | 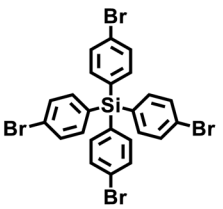 | Yamamoto-type Ullmann coupling | 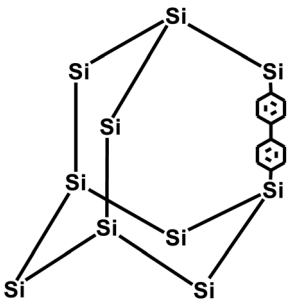 | 13 |
| PPN-5 | 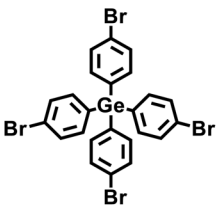 | Yamamoto-type Ullmann coupling | 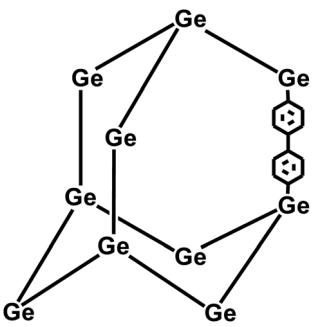 | 13 |
| PPN-6 | 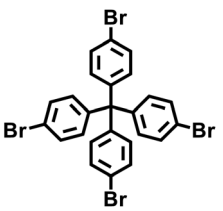 | Yamamoto-type Ullmann coupling | 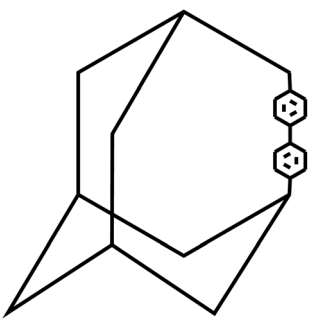 | 13 |

Table 2 (*Contd.*)

| Common name | Building units | Reactions | Proposed structures | Ref. |
|---|---|---|---|---|
| PAF-100 | 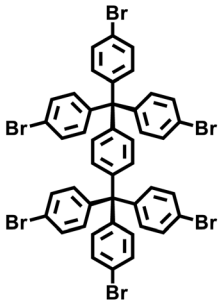 | Yamamoto-type Ullmann coupling | 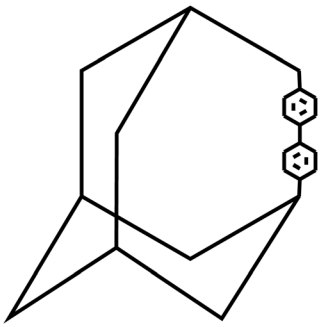 | 35 |
| PAF-101 | 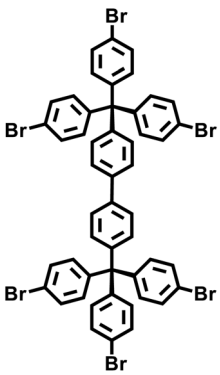 | Yamamoto-type Ullmann coupling | 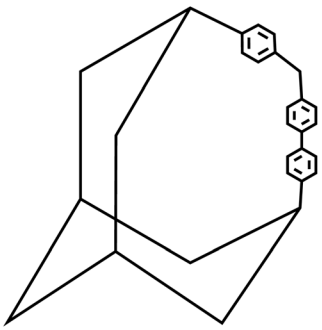 | 35 |
| TCB-CMP | 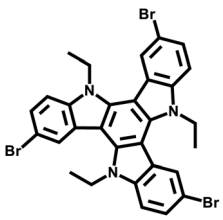 | Yamamoto-type Ullmann coupling | 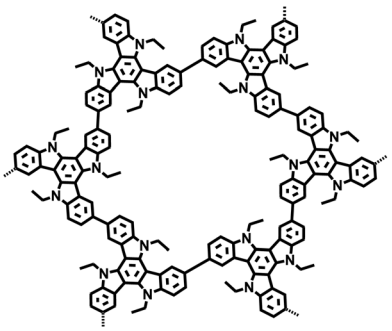 | 38 |
| PAF-11 | 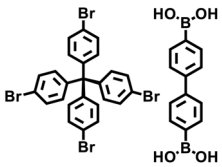 | Suzuki–Miyaura coupling | 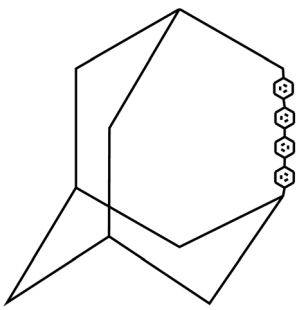 | 40 |

Table 2 (*Contd.*)

| Common name | Building units | Reactions | Proposed structures | Ref. |
|---|---|---|---|---|
| PAF70-$NH_2$ | 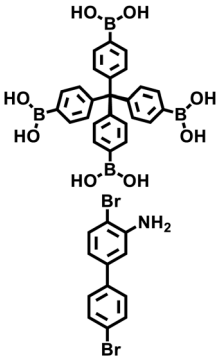 | Suzuki–Miyaura coupling | 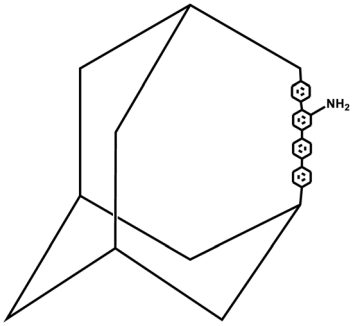 | 28 |
| PAF-76 | 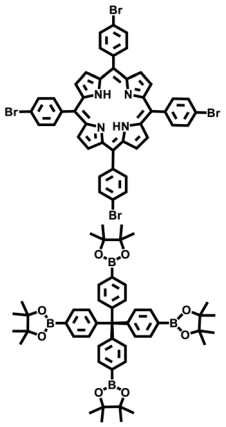 | Suzuki–Miyaura coupling | 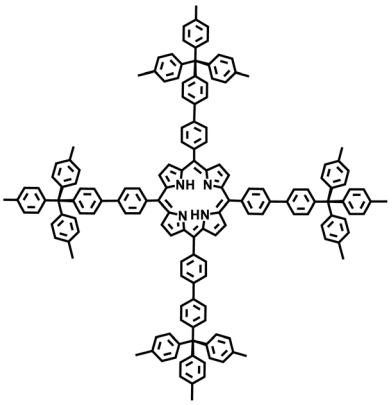 | 41 |
| PAF-111 | 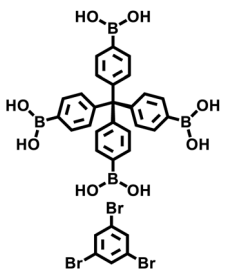 | Suzuki–Miyaura coupling | 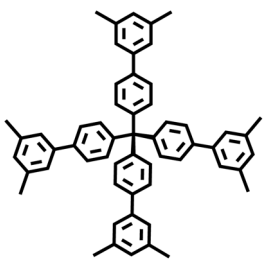 | 42 |
| PAF-112A | 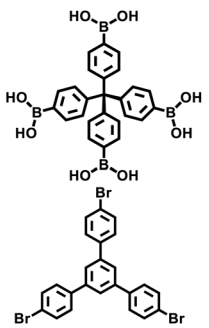 | Suzuki–Miyaura coupling | 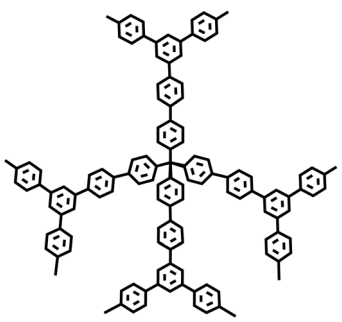 | 42 |

Table 2 (*Contd.*)

| Common name | Building units | Reactions | Proposed structures | Ref. |
|---|---|---|---|---|
| PAF-112B | 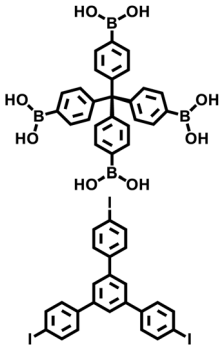 | Suzuki–Miyaura coupling | 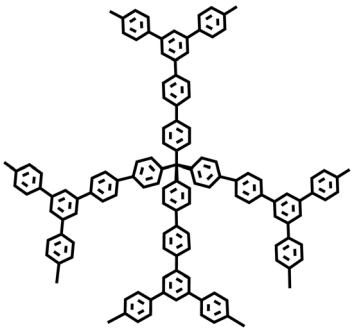 | 42 |
| PAF-113 | 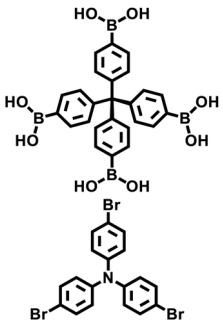 | Suzuki–Miyaura coupling | 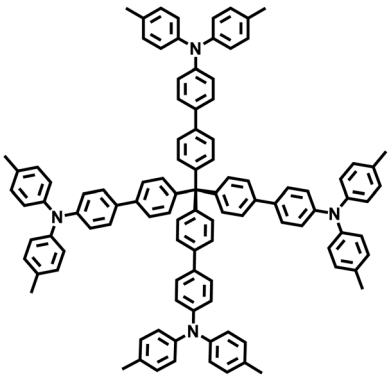 | 42 |
| P1 | 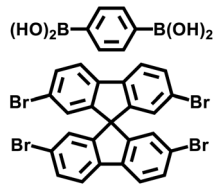 | Suzuki–Miyaura coupling | 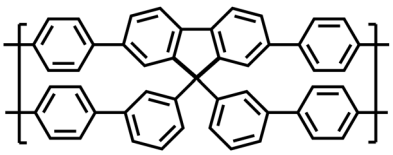 | 43 |
| P2 | 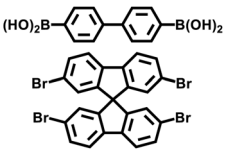 | Suzuki–Miyaura coupling | 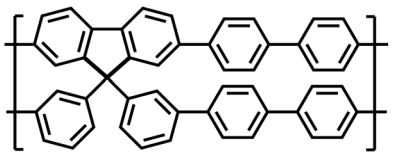 | 43 |
| PP-CMP | 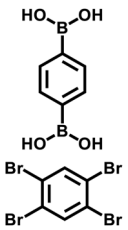 | Suzuki–Miyaura coupling | 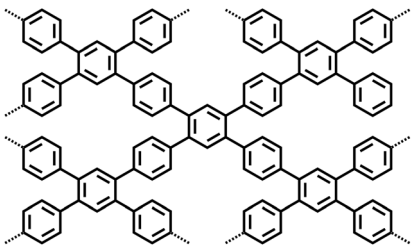 | 44 |
| CP-CMP | 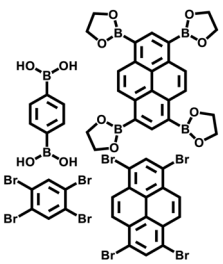 | Suzuki–Miyaura coupling | CP-CMP 1-15 | 16 |

Table 2 (*Contd.*)

| Common name | Building units | Reactions | Proposed structures | Ref. |
|---|---|---|---|---|
| PrPy | 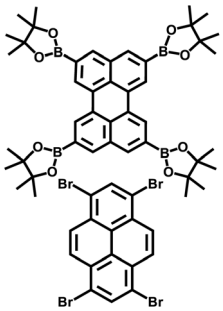 | Suzuki–Miyaura coupling | 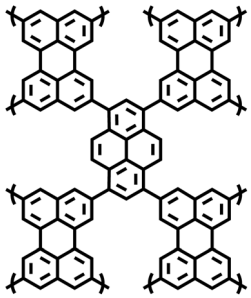 | 45 |
| PrTPE | 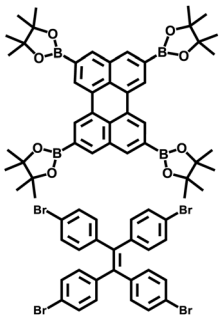 | Suzuki–Miyaura coupling | 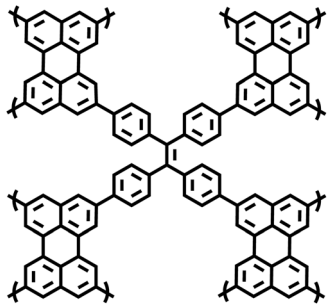 | 45 |
| CTP-1 | 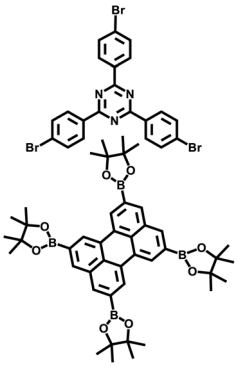 | Suzuki–Miyaura coupling | 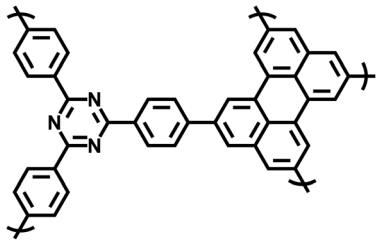 | 46 |
| CTP-2 | 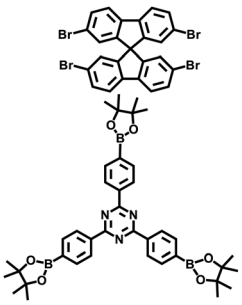 | Suzuki–Miyaura coupling | 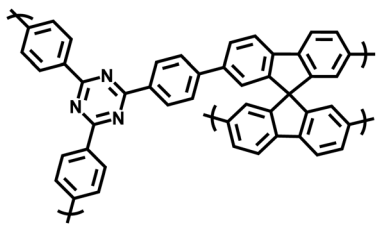 | 46 |
| CPOP-1 | 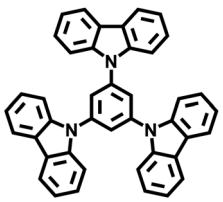 | Oxidative coupling | 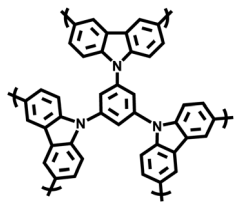 | 48 |

Table 2 (*Contd.*)

| Common name | Building units | Reactions | Proposed structures | Ref. |
|---|---|---|---|---|
| TPOP-4 | 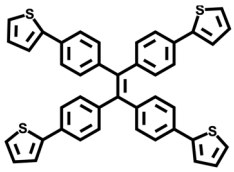 | Oxidative coupling | 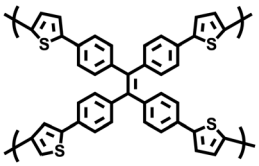 | 47 |
| ThPOP-1 | 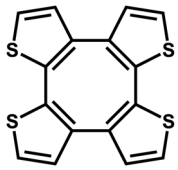 | Oxidative coupling | 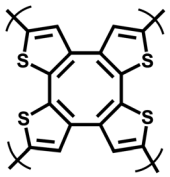 | 49 |
| ThPOP-2 | 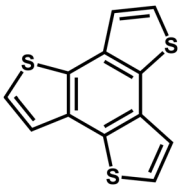 | Oxidative coupling | 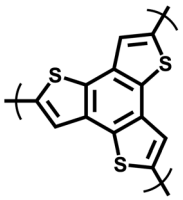 | 49 |

adsorption capacity and $CO_2$ adsorption capacity were 20 $cm^3$ $g^{-1}$ and 59 $cm^3$ $g^{-1}$, respectively, at 273 K and 760 mmHg. JUC-Z4 and its derivatives can modulate pore structure and polarity *via* redox reactions, thus exhibiting high capacity and selectivity in hydrogen storage, methane storage, and $CO_2$ capture. They are particularly advantageous in gas adsorption under low pressure and cyclic stability, providing an efficient material option for clean energy storage and environmental pollutant treatment.

In 2011, Zhou *et al.* employed a Ni(0)–catalyzed Yamamoto-type Ullmann coupling reaction, using tetrakis(4-bromophenyl)silicon and tetrakis(4-bromophenyl)adamantane as monomers, to synthesize PPNs with enhanced specific surface areas (Fig. 3d).[13] Among them, PPN-4 features an especially large specific surface area ($S_{BET}$ = 6461 $m^2$ $g^{-1}$). This polymer also demonstrates outstanding gas adsorption capabilities, achieving an adsorption capacity of 0.158 g $g^{-1}$ for $H_2$ at 77 K and 90 bar, 0.39 g $g^{-1}$ for $CH_4$ at 295 K and 55 bar, and 2.12 g $g^{-1}$ for $CO_2$ at 295 K and 50 bar. Subsequently, Jiang *et al.* synthesized the carbazole based conjugated microporous polymer (TCB-CMP) *via* Yamamoto coupling reaction that could be used to sense chemicals.[38] TCB-CMP is unique in that it discriminates between electron-rich and electron-deficient arenes and exhibits opposite fluorescence outputs with fluorescence-on and fluorescence-off characteristics. The micropores absorb arene molecules into the confined space of the polymer, the skeleton possesses a large surface area and provides a broad interface for arenes, and the network architecture facilitates exciton migration across the framework. These structural features function cooperatively, thereby enhancing the signaling activity of TCB-CMP in fluorescence-on and fluorescence-off detection.

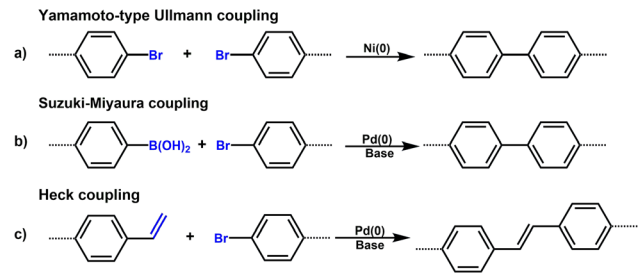


Scheme 1 C($sp^2$)–C($sp^2$) coupling reaction for the synthesis of porous frameworks.

The Suzuki–Miyaura reaction was first reported by Akira Suzuki in 1979.[39] It refers to a cross-coupling reaction between aryl or alkenyl boronic acids and aryl or alkenyl halides in the presence of a palladium catalyst (such as $Pd(PPh_3)_4$) and a base (such as potassium carbonate, potassium phosphate, *etc.*). This forms a new carbon–carbon bond and generates biaryl, bisalkenyl or aryl-alkenyl compounds. Renowned for its mild reaction conditions, high efficiency, broad substrate compatibility, and excellent functional group tolerance, the Suzuki–Miyaura coupling reaction has become a powerful tool for the synthesis of POP materials, enabling the construction of diverse molecular architectures with tailored properties. In 2011, PAF-11 was synthesized by Zhu *et al. via* the Suzuki–Miyaura coupling reaction, in which tetrakis(4-(dihydroxyboryl)phenyl) methane (a tetrahedral unit) was polymerized with 4,4′-biphenyl diboronic acid.[40] It exhibits good thermal stability (up to 400 °C) and chemical stability. At 77 K and 1 bar, its $H_2$ adsorption

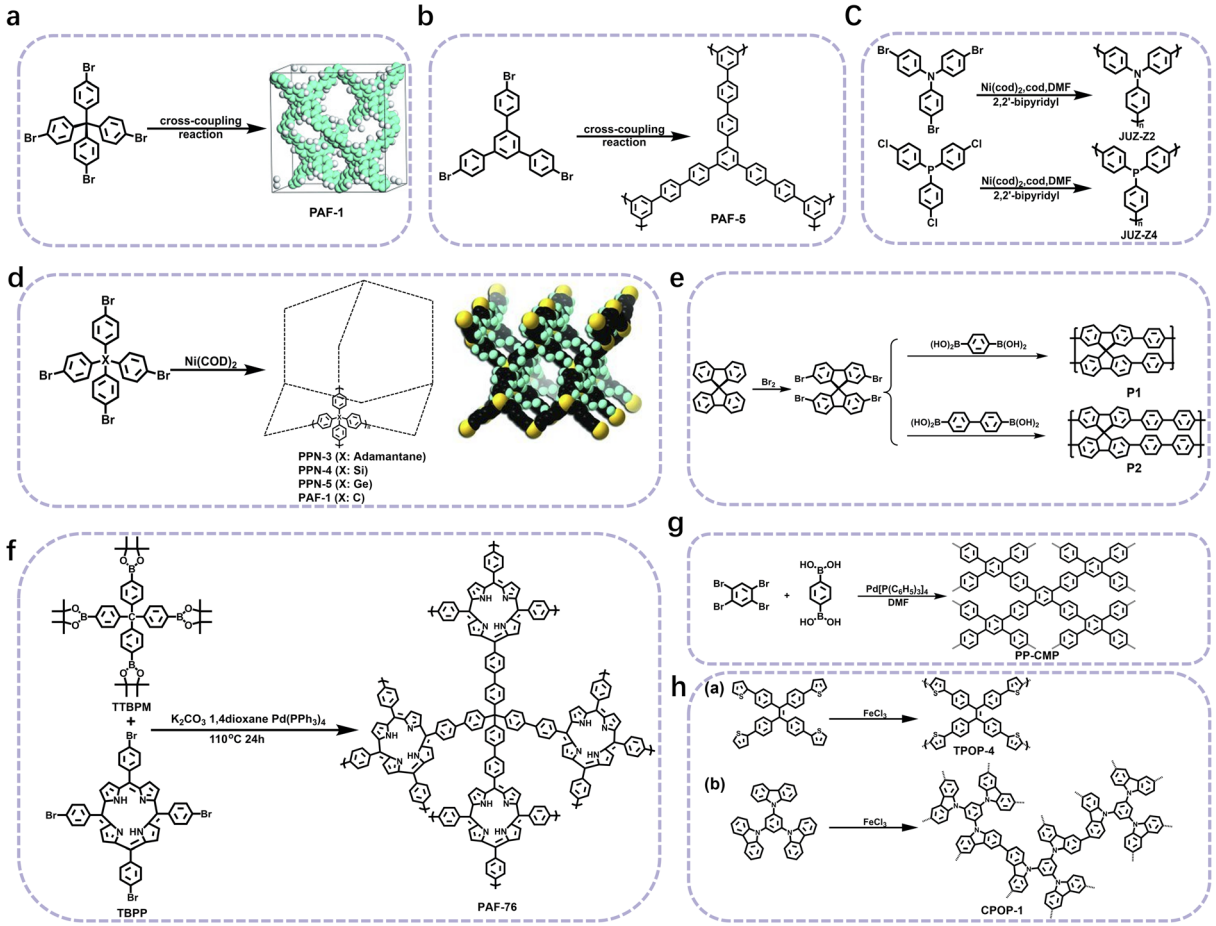


Fig. 3 (a) The synthesis of PAF-1.[3] Copyright 2009 Wiley-VCH GmbH. (b) The synthesis of PAF-5.[34] Copyright 2011 the Royal Society of Chemistry. (c) The synthesis of JUC-Z2.[36] Copyright 2012 Springer Nature. and JUC-Z4.[37] Copyright 2013 the Royal Society of Chemistry. (d) Synthetic route for PPN-3, PPN-4, PPN-5, and PAF-1.[13] Copyright 2011 Wiley-VCH GmbH. (e) Synthetic pathway towards the CMPs P1–P2.[43] Copyright 2008 American Chemical Society. (f) A representation of the synthesis of PAF-76 employing TTBPM and TBPP reactants.[41] Copyright 2016 Wiley-VCH GmbH. (g) The synthesis of PP-CMP.[44] Copyright 2017 Science China Press. (h) The synthesis of TPOP-4 and CPOP-1.[47] Copyright 2011 the Royal Society of Chemistry.

capacity is 1.03 wt%. It also exhibits high adsorption capacities for small aromatic molecules such as benzene and toluene, with adsorption amounts of 874 mg $g^{-1}$ (11.2 mmol $g^{-1}$) and 780 mg $g^{-1}$ (8.5 mmol $g^{-1}$), respectively, at room temperature. These initial findings not only demonstrate the feasibility of the Suzuki–Miyaura coupling in POPs synthesis but also laid the groundwork for subsequent explorations in this area. Building on this, this group further employed the Suzuki–Miyaura coupling reaction to synthesize PAF-76 in 2016 (Fig. 3f).[41] By using tetrakis(4-(dihydroxyboryl)phenyl)methane as tetrahedral nodes and tetrakis(4-bromophenyl) porphyrin as planar nodes, they created a new material with enhanced structural complexity. PAF-76 exhibits high thermal stability, excellent recyclability, and robust solvent resistance, highlighting its promising potential in heterogeneous catalyst development. This work represents a significant advancement, as it expands the scope of building blocks and functionalities accessible through the Suzuki–Miyaura coupling in POPs synthesis. To further expand the scope of this synthetic strategy, Zhu *et al.* achieved the carbon–carbon coupling polymerization of tetrakis(4-borophenyl)methane and 4,4′-dibromo-2-aminobiphenyl *via* the Suzuki–Miyaura coupling reaction in 2018, leading to the preparation of PAF70-$NH_2$.[8] The outstanding stability and uniformly distributed mesopore characteristics of PAF70-$NH_2$ enabled efficient immobilization of relatively large-sized catalysts within its pores. This unique property not only enhances the catalyst utilization rate but also extends its service life, facilitating complete accessibility of catalysts in recyclable heterogeneous organocatalysis. Moreover, the research group employed the Suzuki–Miyaura coupling reaction to polymerize four-node monomers with a series of three-node monomers, successfully synthesizing PAF-111, PAF-112A, PAF-112B, and PAF-113.[42] Using rhodamine B (RB) as a model organic dye, the adsorption performance of these PAFs was evaluated. Among them, PAF-111, with the highest specific surface area of 857 $m^2$ $g^{-1}$, demonstrates a maximum adsorption capacity for RB of 1666 mg $g^{-1}$, ranking it among porous organic materials with excellent adsorption capacities for organic dyes. The excellent stability of PAF-111 ensures high recyclability in organic dye adsorption,

underscoring the great potential of PAFs in water treatment applications. Collectively, these studies by Zhu and colleagues vividly illustrate the evolution and refinement of the Suzuki–Miyaura coupling-based synthesis strategies for PAFs, gradually expanding their applications from gas adsorption to catalysis and environmental remediation.

Meanwhile, in the realm of CMPs, Thomas and colleagues made a significant breakthrough in 2008 by expanding the monomer synthesis to three-dimensional (3D) structures (Fig. 3e).[43] Utilizing 2,2′,7,7′-tetrabromo-9,9′-spirobifluorene as a monomer, they successfully synthesized fluorescently active products for the first time *via* the Suzuki–Miyaura coupling reaction. Conjugated polymers based on the spirobifluorene unit combine microporosity and conjugation properties, integrating two important concepts in materials science "microporous structure" and "optoelectronic activity", and providing new ideas for the construction of stable interfaces in organic electronic devices. Current research in this field is being extended to film-forming materials, aiming to develop high-performance advanced devices.

Building on the advancements in Suzuki–Miyaura coupling-based POPs synthesis, research on CMPs has also witnessed remarkable progress, expanding the materials' functionality and application scope. In 2010, Jiang *et al.* initiated a new exploration by employing 1,2,4,5-tetrabromobenzene and 1,4-benzenediboronic acid as monomers to synthesize CMPs featuring a complete benzene ring structure (PP-CMP) through the Suzuki–Miyaura coupling reaction (Fig. 3g).[44] The PP-CMP exhibit intrinsic fluorescence quenching and exceptional light collection properties, paving the way for their subsequent application in the field of optoelectronics. This pioneering work inspired further investigations into the design and synthesis of CMPs with tailored optical properties. In 2015, Cooper and colleagues made significant strides by using the Suzuki–Miyaura coupling reaction to synthesize a series of CMPs based on pyrene and benzene.[16] By precisely tuning the feed ratios of different monomers, they achieved fine control over crucial material properties, including the specific surface area, fluorescence emission, visible light absorption characteristics, and energy band structure of the target CMPs. Among them, CP-CMP10 exhibited excellent hydrogen evolution activity and stability under visible light. Its hydrogen evolution rate under visible light was 30 times that under ultraviolet light (with U-340 filter). It is the first organic hydrogen evolution photocatalyst that mainly relies on visible light, which is in line with the demand for solar energy utilization and provides a new strategy for the design of organic photocatalysts for efficient solar energy utilization. Building on the trend of monomer design innovation, Jiang *et al.* further explored the potential of perylene derivatives.[45] They utilized pyrene and tetraphenylethylene comonomers to prepare two distinct geometric configurations of four-arm CMPs (PrCMPs) through Suzuki–Miyaura cross-coupling reactions. Among them, pyrene-based polymer network (PrPy) with a specific surface area of 1219 $m^2\ g^{-1}$, not only exhibits strong gas adsorption performance (with a $CO_2$ adsorption capacity of 3.89 mmol $g^{-1}$), but also possesses unique structural and optical advantages. Its higher degree of conjugation, planar structure, broader UV-visible absorption, reduced photoluminescence lifetime, and notable photocatalytic activity demonstrated the great potential of PrCMPs in both gas adsorption and photocatalysis applications.

In a parallel development, Niu *et al.* ventured into the application-driven synthesis of CMPs.[46] They synthesized CTP-1 and CTP-2 from perylene derivatives and triazine monomers through the Suzuki–Miyaura coupling reaction and successfully applied these CMPs as polysulfide fixatives and catalysts in lithium–sulfur (Li–S) batteries. The electrochemical properties of CTP-1 and CTP-2 were particularly favorable, and notably, CTP-1 exhibited a narrower band gap and enhanced electron transfer efficiency compared to CTP-2, leading to a stronger binding affinity for polysulfides. This work expanded the application boundaries of CMPs from traditional adsorption and optical fields to the emerging area of energy storage.

The oxidative coupling reaction, a typical carbon–carbon coupling approach, has also made significant contributions to CMP synthesis. Lewis acids such as $FeCl_3$ and $AlCl_3$ often serve as catalysts in reactions involving carbazole and thiophene, and electron-rich aromatics like triphenylamine participate in these oxidative coupling processes. In 2011, Han *et al.* innovatively fabricated TPE-based porous organic polymers (TPOPs) *via* oxidative coupling reaction, endowing the materials with outstanding comprehensive properties (Fig. 3h).[47] Their BET specific surface areas reach 681 $m^2\ g^{-1}$ and 810 $m^2\ g^{-1}$, respectively, with pore sizes centrally distributed at 0.67 nm, featuring well-defined microporous structures. They exhibit excellent hydrogen adsorption performance, and notably, TPOP-5 achieves a high hydrogen uptake capacity of 1.07 wt% at 1.13 bar and 77 K, demonstrating remarkable potential for hydrogen storage applications. Furthermore, both polymers possess good acid and alkali resistance, and are thermally stable up to 300 °C under a nitrogen atmosphere, combining structural robustness with functional practicality and laying a solid foundation for their practical applications in related fields. Building on this concept, the same group focused on the oxidative self-coupling polymerization of 1,3,5-tris(9-carbazolyl) benzene in 2012 to synthesize porous polycarbazole (CPOP-1) with a large specific surface area of 2220 $m^2\ g^{-1}$ (Fig. 3h).[48] This polymer not only exhibits excellent gas adsorption performance, with $H_2$ adsorption capacity of 2.80 wt% at 77 K and 1.0 bar, and $CO_2$ adsorption capacity of 21.2 wt% at 273 K and 1.0 bar, but also demonstrates remarkable adsorption selectivity of 33 for $CO_2/CH_4$ and 25 for $CO_2/N_2$ at 273 K. These results highlight the unique advantages of oxidative coupling in creating CMPs with high-performance adsorption properties, further enriching the synthetic strategies and application scenarios of porous organic polymers. Polymers such as CPOPs, TPOPs, and ThPOPs prepared *via* oxidative coupling polymerization possess high specific surface areas, excellent gas adsorption capacities (for $H_2$ and $CO_2$), and good chemical and thermal stability.[49–53] Some of them also exhibit photoluminescent or catalytic activity. These polymers require no complex functional groups and feature facile preparation, holding great significance in fields including gas storage and

separation, heterogeneous catalysis, and electronic devices. They provide an efficient pathway for the development of related functional materials.[54,55]

### 2.3 C(sp)–C(sp) coupling reaction

POPs constructed *via* C(sp)–C(sp) coupling reactions are a new class of functional materials, featuring three-dimensional porous network structures formed by linking building blocks through alkynyl bonds. Synthesized *via* direct coupling of sp-hybridized carbon atoms, such POPs are typically prepared through alkyne polymerization reactions, among which alkyne oxidative coupling stands out as a paradigmatic strategy in C(sp)–C(sp) coupling (Table 3). This reaction plays a pivotal role in the synthesis of CMPs. Under the catalysis of Pd(II)/Cu(I) systems, terminal alkynes undergo C(sp)–C(sp) oxidative coupling to form diyne compounds (Fig. 4a).[9,10] This synthetic route enables the efficient introduction of rigid alkynyl units, endowing the materials with excellent thermal, chemical, and mechanical stability. In terms of structural features, these POPs can form highly cross-linked rigid frameworks with uniform pore size distribution, thus possessing a large specific surface area and precisely tunable pore structures. These unique structural and physicochemical properties endow them with broad application prospects in multiple key technological fields, as elaborated below. In gas adsorption and separation, they can efficiently capture gas (*e.g.*, $CO_2$) and achieve high-selectivity separation of mixed gases (*e.g.*, $CO_2/N_2$ and light hydrocarbons).[56] In catalysis, as heterogeneous catalysts, they exhibit remarkable performance in photocatalysis, heterogeneous catalysis, and electrochemical conversion reactions, particularly showing enormous potential in $CO_2$ resource conversion and fine organic synthesis.[16,17] Furthermore, such POPs hold significant research value and application prospects in interdisciplinary fields, including environmental remediation (*e.g.*, efficient removal of pollutants), energy storage (as electrode materials), and biomedicine (*e.g.*, targeted drug delivery and biosensing).[18,57]

In 2008, Cooper *et al.* successfully synthesized a series of CMPs, namely HCMP-1 and HCMP-2, through the oxidative self-coupling polymerization of terminal alkyne monomers derived from 1,3,5-triethynylbenzene (Fig. 4b).[9] HCMP-1 exhibits a specific surface area of 842 $m^2\ g^{-1}$, while HCMP-2 exhibits a specific surface area of 827 $m^2\ g^{-1}$. These polymers exhibit excellent thermal and chemical stability, thus highlighting their significant potential for gas adsorption applications. Specifically, HCMP-1 and HCMP-2 exhibit $H_2$ adsorption capacities of 107 $cm^3\ g^{-1}$ and 131 $cm^3\ g^{-1}$, respectively, at 77.3 K and 1.13 bar.

Building upon these pioneering achievements, Zhou *et al.* leveraged the Oxidative Eglinton coupling reaction in 2010 to polymerize tetrakis (4-alkynylphenyl)methane (Fig. 4c).[56] This endeavor led to the synthesis of diynyl-linked PPN-1 with a specific surface area of 1249 $m^2\ g^{-1}$ and PPN-2 with a specific surface area of 1764 $m^2\ g^{-1}$. These POPs not only exhibit remarkable thermal and chemical stability but also feature tunable porosity and chemical composition. These structural and chemical features collectively contribute to their excellent $H_2$ adsorption capacities, with PPN-1 achieving an adsorption capacity of 3.30 wt% at 77 K and 45 bar, and PPN-2 showing an adsorption capacity of 3.76 wt% under the same conditions (77 K and 45 bar). Notably, PPN-1 demonstrated a higher $CO_2/CH_4$ adsorption selectivity for $CO_2/CH_4$ adsorption, rendering it a promising candidate for industrial-scale $CO_2/CH_4$ separation technologies.

While the oxidative coupling reactions have laid a solid foundation, the Glaser coupling reaction represents one of the earliest established terminal alkyne coupling processes and offers an alternative synthetic pathway. In this reaction, ethynyl-substituted benzene compounds act as the fundamental building blocks, with ammonia or pyridine serving as the bases and methanol or ethanol functioning as the solvents.[10,58] A series of butadiynyl-linked CMPs have been successfully fabricated *via* the Glaser coupling reaction (Fig. 4d). At 273 K and 1 bar, TPM-BD-CMP exhibited a maximum $CO_2$ adsorption capacity of 3.78 mmol $g^{-1}$ and a maximum $CH_4$ adsorption capacity of 0.95 mmol $g^{-1}$. Its *in situ* gel-forming property facilitates processability, along with high specific surface areas, hierarchical pore structures, and excellent $CO_2/CH_4$ adsorption performance. This method provides a new strategy for preparing functionalized CMPs under low-cost and mild conditions, thereby expanding their potential applications in energy storage and environmental remediation. Inspired by the robustness of the Glaser coupling approach, Chen *et al.* pioneered the utilization of polyethynyl-substituted aromatic monomers with diverse geometric configurations in 2017.[10] They synthesized a series of alkyne-linked CMPs based on 1,3-butanediamide *via* the Glaser coupling reaction, with CuCl as the catalyst. The resultant CMPs possess remarkable properties, including a specific surface area of 1008 $m^2\ g^{-1}$ and a total pore volume of 1.11 $cm^3\ g^{-1}$.

These materials demonstrate exceptional adsorption capacities for both $CO_2$ and $CH_4$. The unique properties of these CMPs stem from the enhanced π–π electron delocalization within the diacetylene moieties, coupled with coordination effects and the feasibility of effective post-modification of active sites. Consequently, this class of CMPs displays outstanding UV-visible light absorption capabilities and electrochemical properties, rendering them highly suitable for photocatalytic applications and opening new avenues for research in renewable energy conversion. These studies collectively highlight the versatility and significance of C(sp)–C(sp) coupling reactions in the rational design and synthesis of porous organic polymers. By meticulously adjusting monomer structures, optimizing catalyst systems, and fine-tuning reaction conditions, researchers have achieved precise control over critical material properties, such as porosity, specific surface area, and chemical reactivity. This precise control has significantly expanded the application scope of such POPs, ranging from gas adsorption and separation to photocatalysis. Looking forward, future research is expected to focus on developing more sustainable and efficient catalytic systems, exploring novel strategies for incorporating multifunctional moieties, and innovating synthetic methodologies that integrate multiple coupling

Table 3 A summary of building units, frameworks, and the corresponding synthetic using C(sp)–C(sp) coupling

| Common name | Building units | Reactions | Proposed structures | Ref. |
|---|---|---|---|---|
| HCMP-1 | 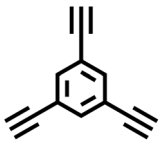 | Oxidative Eglinton coupling reaction | 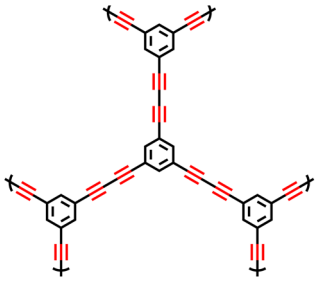 | 9 |
| HCMP-2 |  | Oxidative Eglinton coupling reaction | 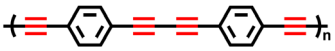 | 9 |
| PPN-1 | 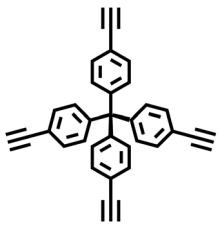 | Oxidative Eglinton coupling reaction | 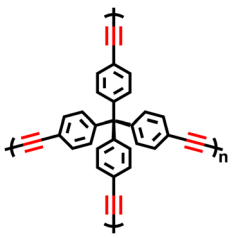 | 56 |
| PPN-2 | 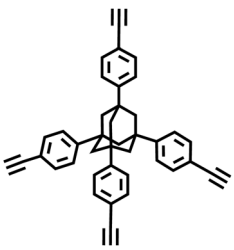 | Oxidative Eglinton coupling reaction | 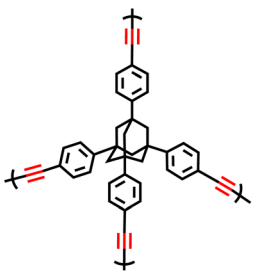 | 56 |
| TPB-BD-CMP | 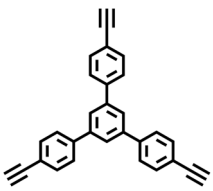 | Glaser coupling reaction | 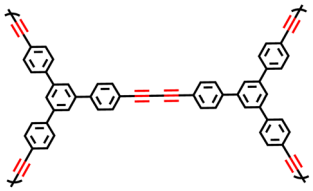 | 10 |
| TPA-BD-CMP | 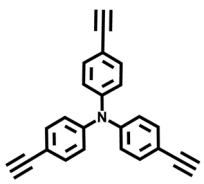 | Glaser coupling reaction | 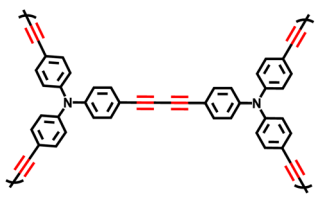 | 10 |
| TPM-BD-CMP | 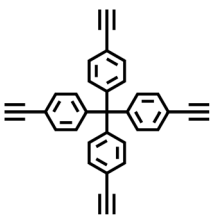 | Glaser coupling reaction | 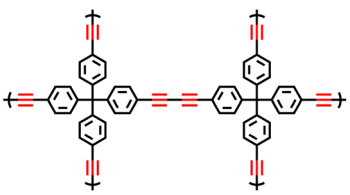 | 10 |
| SPF-BD-CMP |  | Glaser coupling reaction | 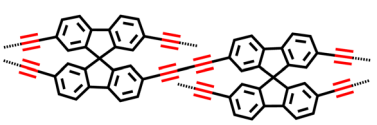 | 10 |

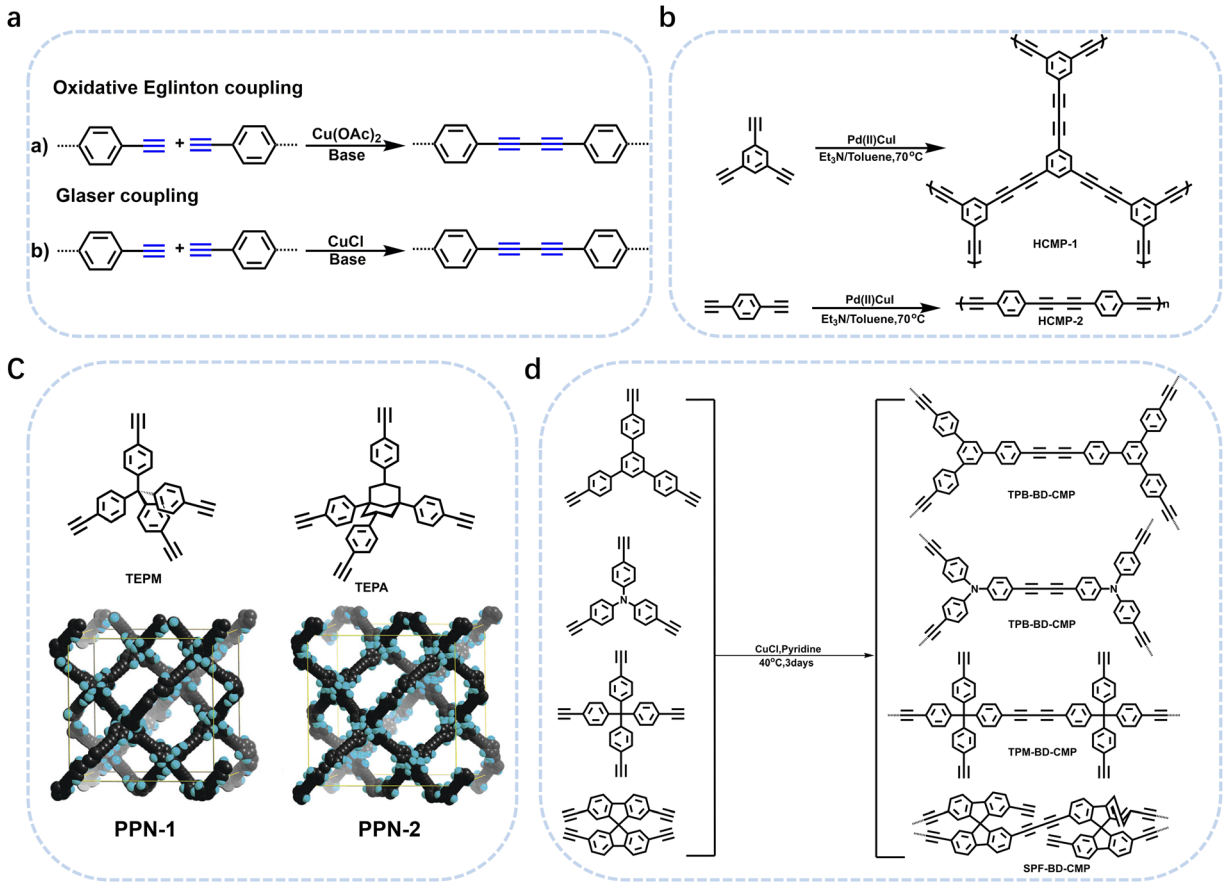


Fig. 4 (a) C(sp)–C(sp) coupling reaction for the synthesis of porous frameworks. (b) The synthesis of HCMP-1 and HCMP-2.[9] Copyright 2008 the Royal Society of Chemistry (c) Tetrahedral monomers and the default noninterpenetrated diamondoid networks of the PPNs generated by coupling reactions (TEPM, PPN-1; TEPA, PPN-2; TBPA, PPN-3).[56] Copyright 2010 American Chemical Society. (d) Synthetic routes for the four BD-CMPs.[10] Copyright 2017 the Royal Society of Chemistry and the Chinese Chemical Society.

reactions, thereby driving continuous advancements in the field of POP materials.

### 2.4 $C(sp^2)$–$C(sp^3)$ coupling reaction

The Friedel–Crafts alkylation reaction stands as a cornerstone for achieving $C(sp^2)$–$C(sp^3)$ coupling between aromatic hydrocarbons and haloalkanes, providing an effective approach for the synthesis of POPs with regulated structures and properties. This reaction mechanism has been extensively investigated as a powerful synthetic tool for fabricating advanced materials with unique properties. Cooper *et al.* pioneered the use of small-molecule monomers with leaving groups to promote the Friedel–Crafts reaction (Fig. 5a).[59] This innovative strategy enables direct self-polycondensation or co-polymerization, ultimately leading to the fabrication of HCPs with remarkably high specific surface areas. By employing small molecules bearing chloromethyl groups as monomers and leveraging Lewis acid catalysts, the Friedel–Crafts alkylation reaction occurs between the chloromethyl moieties and adjacent benzene rings. As a result, hydrogen chloride (HCl) was eliminated, and dense molecular linkages were formed between the small molecule building units, giving rise to the formation of HCPs (Fig. 5b). Although this method offered the flexibility to tune the specific surface areas of the polymers by adjusting the monomer proportions, it is limited by the relatively narrow diversity of monomers with leaving groups. Nevertheless, the synthesized polymers exhibited impressive performance metrics, boasting a specific surface area of 1904 $m^2\ g^{-1}$, an $H_2$ adsorption capacity of 3.68 wt% at 77 K and 15 bar, and an excellent $CH_4$ adsorption capacity of 116 $cm^3\ g^{-1}$ at 298 K and 20 bar.[60] These findings not only demonstrated the feasibility of the approach but also laid a solid foundation for subsequent advances in Friedel–Crafts-based POP synthesis.

Building on this seminal work, Tan *et al.* further propelled the field forward in 2011 by developing a modified synthesis strategy for HCPs with ultrahigh specific surface areas.[61] They achieved this by reacting a variety of aromatic hydrocarbons (*e.g.*, benzene, biphenyl, and 1,3,5-triphenylbenzene) with dimethoxymethane or dichloroalkanes (Fig. 5c). The resulting polymers exhibited remarkable adsorption capabilities for both $H_2$ and $CO_2$, which underscores their great potential in gas storage applications. This synthetic method offers several notable advantages to the table, including abundant and low-cost raw materials, facile tunability of pore structures, and mild reaction conditions, the ability to create diverse chemical

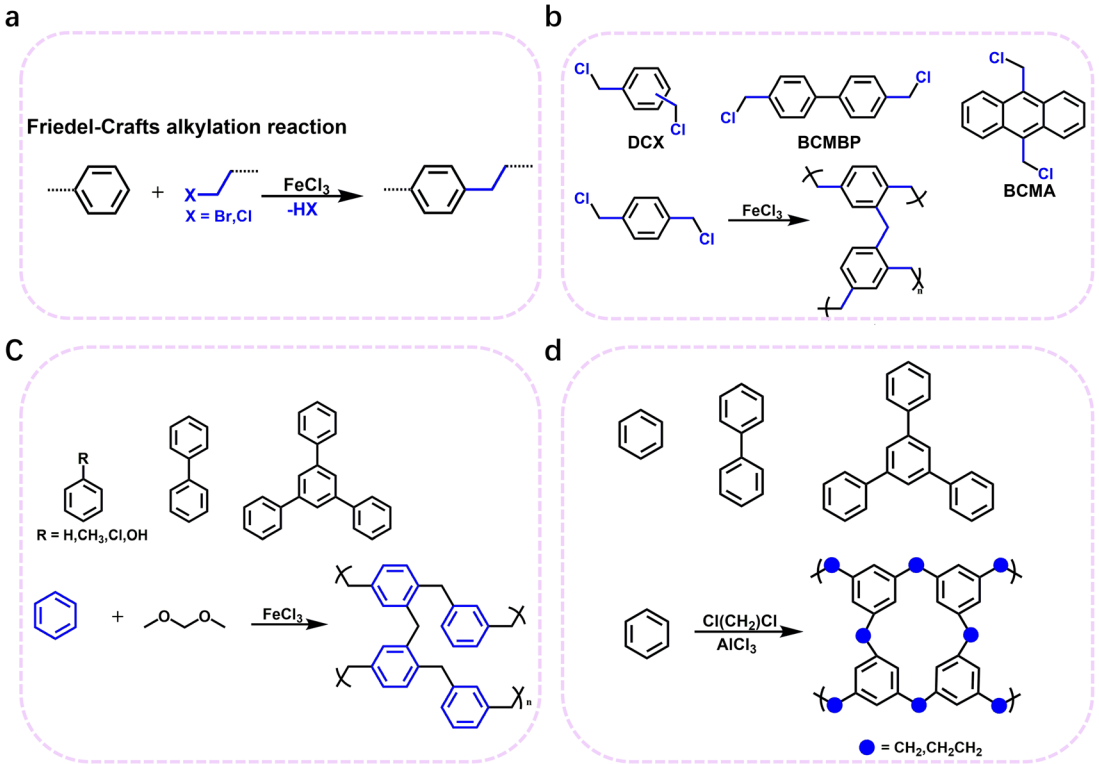


Fig. 5 (a) The Friedel–Crafts alkylation reaction. (b) Monomers used for the synthesis of the hypercrosslinked polymer networks.[59] Copyright 2007 American Chemical Society. (c) Scheme showing the synthetic pathway to the network structure.[61] Copyright 2011 American Chemical Society. (d) Molecular structures of the building blocks for the network and the synthetic pathway to produce the network structure.[11] Copyright 2017 American Association for the Advancement of Science.

architectures, and straightforward functionalization procedures. Overall, this simple yet highly effective approach represents a significant leap forward, as it substantially expanded the monomer pool for HCP synthesis. Consequently, it broadens the scope of HCPs and opens up new avenues for their potential applications in interdisciplinary fields, ranging from energy storage to environmental remediation.

Continuing the trend of innovation, in 2017, the Tan group developed a solvent-knitting strategy for the fabrication of layered HCPs with high specific surface areas and excellent gas storage capabilities (Fig. 5d).[11] SHCP-3, with significantly higher microporosity, exhibits the highest $CO_2$ uptake of 4.84 mmol $g^{-1}$ at 273 K and 1.00 bar. The $CO_2$ uptake of SHCP-3 is substantially higher than that of other HCP materials under identical conditions, representing the highest $CO_2$ uptake capacity among HCP materials reported to date. This superior $CO_2$ uptake performance of SHCP-3 is attributed to its enhanced microporosity, which provides abundant adsorption sites for $CO_2$ molecules. This strategy has several outstanding characteristics: (i) the strategy enables the fabrication of porous materials with high specific surface areas, abundant microporous structures, and excellent gas storage capacities. (ii) Simple synthesis conditions, low-cost reagents, and high yields enable the economical and large-scale production of such materials. (iii) Tunable porous structures and specific surface areas can be achieved by modulating the solvent chain length, the molar ratio of $AlCl_3$, and the monomer size. In a parallel line of research, Yavuz *et al.* reported the fabrication of flexible POPs *via* the Friedel–Crafts alkylation reaction of benzene with 1,2-dichloroethane.[62] The resulting polymer exhibits outstanding $CH_4$ adsorption performance, achieving a $CH_4$ adsorption capacity of up to 0.625 g $g^{-1}$, which surpasses the methane adsorption target (0.5 g $g^{-1}$) established by the U.S. Department of Energy (DOE) for practical on-board applications. This remarkable achievement not only highlights the enormous potential of $C(sp^2)$–$C(sp^3)$ coupling reactions in developing high-performance gas storage materials but also underscores the critical role of innovative monomer design and reaction engineering in advancing the field of porous organic polymers. It serves as a compelling testament to the ongoing efforts to advance material synthesis paradigms and tailor material properties for practical deployment.

### 2.5 $C(sp^3)$–$C(sp^3)$ coupling reaction

Over the past few decades, traditional POP synthesis mostly relies on $C(sp^2)$–$C(sp^2)$ or $C(sp^2)$–C(sp) or C(sp)–C(sp) coupling. However, due to the core bottlenecks such as the inherent low reactivity of $sp^3$-hybridized carbon and the tendency to undergo side reactions, the application of $C(sp^3)$–$C(sp^3)$ coupling reactions in the preparation of POPs still requires further exploration and improvement. Currently, $C(sp^3)$–$C(sp^3)$ coupling reactions are still mainly limited to the preparation of small organic molecules or oligomers. This limitation greatly restricts

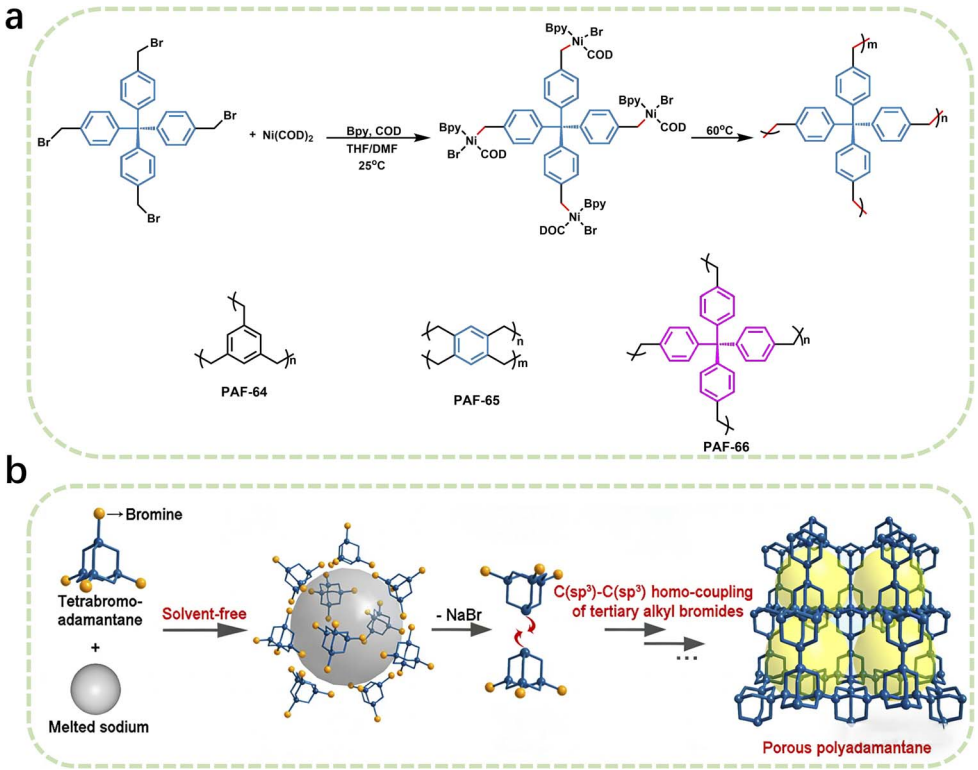


Fig. 6 (a) The synthetic pathway to produce the porous polymers and molecular structures of PAF-64, PAF-65 and PAF-66.[12] Copyright 2024 the Royal Society of Chemistry. (b) The synthetic pathway to produce the porous polyadamantane.[23] Copyright 2026 Science China Press.

the progress in developing new porous materials through this approach and also constitutes a key bottleneck that urgently needs to be broken through in the current research field.[63–66]

A recent breakthrough reported by Liu and Zhu *et al.* has reshaped the landscape of $C(sp^3)$–$C(sp^3)$ coupling in polymer synthesis, paving the way for the rational design of $sp^3$-rich POPs.[12] They have demonstrated that $Ni(COD)_2$ serves as a highly efficient catalyst for promoting $C(sp^3)$–$C(sp^3)$ coupling reactions of bromomethyl arenes. This reaction typically involves two key steps: the reduction of metal halides and the organometallic nucleophilic reaction for carbon–carbon coupling. In traditional methods, although reductants such as Sm and Zn can initiate the slow formation of organometallic nucleophiles, the resulting nucleophiles are relatively low, which is difficult to meet the requirements of coupling polymerization. In contrast, $Ni(COD)_2$, as a catalyst, can directly react with bromomethyl arenes to generate organometallic nucleophiles without additional metallic reductants, thereby efficiently catalyzing the $C(sp^3)$–$C(sp^3)$ coupling reaction of benzyl bromides. Under mild reaction conditions, this catalyst enables the construction of unique structural features. Specifically, when dibromomethyl arenes were used as monomers, the resulting linear polymers exhibit exceptional crystallinity, evidenced by their high melting points ($T_m$ = 286 °C). This exceptional crystallinity stems from the precise control of reaction sites during the $Ni(COD)_2$-catalyzed coupling process, which minimizes random branching and facilitates the formation of well-ordered molecular architectures. On the other hand, the utilization of tribromomethyl or tetrabromomethyl arenes as monomers led to the synthesis of flexible three-dimensional PAFs, such as PAF-64, PAF-65, and PAF-66 (Fig. 6a). These PAFs possess a highly flexible framework, which endows them with a specific surface area of 390 $m^2\ g^{-1}$ and remarkable methane storage capabilities. This performance highlights the potential of $C(sp^3)$–$C(sp^3)$ coupling in the development of advanced materials for gas storage applications. By demonstrating the feasibility of using $Ni(COD)_2$ to overcome the reactivity limitations of $sp^3$-hybridized carbon, it not only provides a new synthetic paradigm for fabricating novel porous polymers but also opens new avenues for developing high-performance methane storage materials for on-board applications.

Building on their previous work on constructing porous polymers *via* carbon–carbon coupling, they further developed a solvent-free sodium-catalyzed $C(sp^3)$–$C(sp^3)$ coupling reaction for the construction of porous polyadamantane (PPA) using 1,3,5,7-tetrabromoadamantane as the monomer (Fig. 6b).[23] As an alkali metal, sodium can induce the homolysis of C–Br bonds through single electron transfer. Without relying on activating groups in the substrates, it can directly activate the $C(sp^3)$–Br bonds of tertiary alkyl bromides successfully overcoming the bottlenecks of low reactivity and high steric hindrance of tertiary alkyl carbons. Traditional POPs mostly rely on phenyl-containing building blocks, but this study breaks through this paradigm, enabling the synthesis of pure alkane-based POPs and expanding the scope of building blocks and synthetic pathways for POPs. PPA exhibits excellent comprehensive properties. Its specific surface area reaches 681 $m^2\ g^{-1}$, with micropores of 0.5 nm and 1.2 nm, as well as abundant

Table 4 A summary of building units and frameworks using $C(sp^3)$–$C(sp^3)$ coupling

| Common name | Building units | Proposed structures | Ref. |
|---|---|---|---|
| PAF-64 | 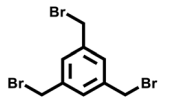 | 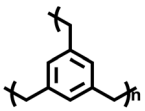 | 12 |
| PAF-65 | 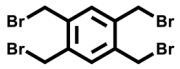 | 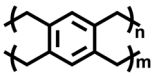 | 12 |
| PAF-66 | 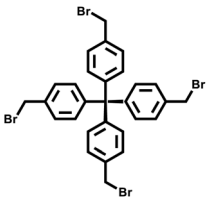 | 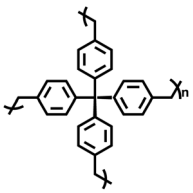 | 12 |
| PPA | 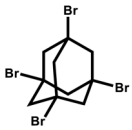 |  | 23 |

mesopores. It shows high separation efficiency for $C_1$–$C_3$ alkanes, with the selectivity for $C_3H_8/CH_4$ up to 317 and for $C_2H_6/CH_4$ up to 13, which is superior to most reported porous materials. This work provides a new pathway for the construction of porous polyalkane materials and is of great significance for promoting the development of related fields. Looking forward, future research may focus on optimizing the reaction conditions to further improve the efficiency and scalability of $C(sp^3)$–$C(sp^3)$ coupling reactions, exploring the use of alternative catalysts or monomers to access polymers with diverse structures and properties, and investigating the potential applications of these materials in energy storage, separation technologies, and beyond (Table 4).

# 3 Application of POPs materials prepared by caron–caron coupling reaction

POPs fabricated *via* carbon–carbon coupling reactions demonstrate tremendous potential for application in gas adsorption and separation, catalysis, and electrochemistry, owing to their unique structural features. Such materials typically exhibit key merits, including tunable pore architectures, low density, high specific surface area, diverse compositions, facile post-functionalization, high carbon content, and superior chemical and thermal stability. These characteristics collectively support their applications in gas adsorption and separation. Firstly, high specific surface area and tailorable pore size distribution serve as the key prerequisites for POPs to achieve efficient gas adsorption.[24,26,27] These materials possess abundant internal microporous and mesoporous structures, which provide ample adsorption active sites for gas molecules, remarkably enhancing gas capture efficiency and providing structural support for efficient adsorption–separation processes. Secondly, superior chemical stability endows POPs with excellent environmental adaptability. The framework of POPs is generally linked *via* rigid covalent bonds, a bonding mode that confers exceptional chemical stability. Even under harsh service conditions (*e.g.*, strong acids, strong alkalis, high temperatures), they can retain structural integrity and stable adsorption performance, thereby expanding their application scope. Thirdly, the facile functionalization capability offers a versatile avenue for regulating the adsorption selectivity of POPs. The surface of the POP framework is rich in functional groups, which facilitates the introduction of specific adsorption sites and the precise modulation of pore microenvironments. Through targeted chemical modification strategies, the selective adsorption capacity of the material toward target gas molecules can be significantly enhanced, enabling efficient separation of mixed gases. Additionally, low density and favorable mechanical stability are important auxiliary advantages of POPs as gas adsorption materials. Low density contributes to reducing the overall load of the adsorption system, while excellent mechanical stability ensures the structural durability of the material during adsorption–desorption cycles, further enhancing its practical application value.

Beyond gas adsorption and separation, POPs also perform excellently as heterogeneous catalysts or catalyst supports in the field of catalysis.[83,84,95] POPs constructed *via* carbon–carbon coupling have enormous catalytic potential, especially in photocatalysis and heterogeneous catalysis, due to their unique structural features (high specific surface area, abundant active sites, tunable pores, and excellent stability). Strategies like C(sp)–C(sp) and $C(sp^2)$–$C(sp^2)$ couplings enable precise regulation of their framework and electronic structure, optimizing photocatalytic performance for organic transformations, pollutant degradation and water splitting. In heterogeneous catalysis, their rigid frameworks and immobilizable active sites act as stable supports/catalysts. Introducing metal ions or functional groups allows customization for $CO_2$ utilization, redox and coupling reactions, offering promising solutions to energy and environmental issues.

In the field of electrochemistry, the inherent characteristics of POPs, including low density, high porosity, high carbon content, and tunable electronic structure, render them promising candidates for energy storage devices such as supercapacitors and batteries.[18,19] However, the poor electrical conductivity of most POPs has become a major bottleneck limiting their widespread application in electrochemical devices. Therefore, future research efforts should focus on improving the electrical conductivity of POPs through strategies such as skeleton engineering and post-modification, which will further broaden their application prospects in the electrochemical field.

POPs possess many advantages that collectively make them ideal materials for multiple fields. With the continuous optimization of synthesis methods and functionalization strategies, the application value of POPs will be steadily improved, and

they are expected to provide innovative solutions for global challenges related to energy shortage, environmental pollution, and sustainable development.

### 3.1 Gas adsorption

Gas adsorption represents one of the most extensive research areas for POPs applications to date.[1,67] The synthetic tunability of porosity, structure, and functionality enables POPs and their composites as promising candidates for adsorption. In addition, owing to their excellent thermal and chemical stability, POPs are insoluble in common organic solvents, thus demonstrating remarkable recyclability as adsorbents.[1] The synthetic tunability of POPs is a key feature that makes them exceptionally promising for adsorption. Through meticulous control of synthesis parameters, researchers can precisely tailor various aspects of POPs, including their porosity, structural architecture, and functionality. In particular, porosity is a critical property, as it directly influences the available surface area for gas adsorption. By adjusting the synthesis conditions, POPs can be designed to possess a broad range of pore sizes, from micropores (with diameters less than 2 nm) that are ideal for capturing small gas molecules, to mesopores (2–50 nm) and macropores (greater than 50 nm) that can facilitate the diffusion and accommodation of larger molecules or even serve as reservoirs for adsorbates.

The structural diversity of POPs also plays a significant role. Their frameworks can be constructed in different topologies, such as linear, two-dimensional, or three-dimensional networks. Each structural configuration offers distinct advantages for gas adsorption. For example, two-dimensional POPs may have a large planar surface area that enhance the interaction with gas molecules, while three-dimensional POPs can provide a more extensive internal void space for adsorption. Furthermore, the ability to incorporate various functional groups into the structures enables customization of surface chemistry. Functional groups can be selected to interact specifically with certain gas molecules through mechanisms such as hydrogen bonding, π–π stacking, or electrostatic interactions, thereby increasing the selectivity and affinity of the adsorption process. In addition to their synthetic flexibility, POPs exhibit remarkable thermal and chemical stability. The stability ensures that they remain intact under a wide range of operating conditions. As a result, POPs are insoluble in common organic solvents, which not only protects their structural integrity but also makes them highly suitable for repeated use as adsorbents. Their excellent recyclability reduces the cost associated with adsorption processes and minimizes environmental impact, by decreasing the need for continuous synthesis of new materials. These combined characteristics of synthetic tunability, stability, and recyclability position POPs as highly attractive candidates for a broad spectrum of gas adsorption applications.

**3.1.1 Hydrogen storage.** Hydrogen is a clean energy gas with high energy density, and its storage is meaningful for industry and manufacturing applications. Hydrogen, known for lightness, cleanliness, abundance, high energy content, and pollution-free combustion products, stands out as a leading candidate to replace traditional energy sources and holds significant promise for future applications.[68,69] The DOE has established expectations for $H_2$ storage materials, which include achieving a $H_2$ storage capacity of 6.0 wt% and 45 g $L^{-1}$. Additionally, these materials should enable reversible charging and discharging at room temperature and medium pressure.[70] Based on distinct adsorption mechanisms, hydrogen storage materials can be primarily categorized into two types: physical adsorption hydrogen storage and chemical adsorption hydrogen storage.[71,72] The latter primarily consists of a metal hydride, in which hydrogen combines with metal in the form of hydrogen ions for the purpose of hydrogen storage. In contrast, the former adsorbs hydrogen molecules within the micropores of porous materials that possess a high specific surface area.

Table 5 $H_2$ storage performances of POPs

| Materials | BET surface area ($m^2$ $g^{-1}$) | $T$ (K) | Pressure (bar) | Uptake (wt%) | Ref. |
|---|---|---|---|---|---|
| PAF-1 | 5600 | 77 K | 48 | 7.0 | 3 |
| PPN-1 | 1249 | 77 K | 45 | 3.3 | 56 |
| PPN-2 | 1764 | 77 K | 40 | 3.76 | 56 |
| PPN-3 | 2840 | 77 K | 42 | 3.28 | 56 |
| PPN-4 | 6461 | 77 K | 55 | 8.34 | 13 |
| PAF-3 | 2932 | 77 K | 1 | 2.07 | 33 |
| PAF-4 | 2246 | 77 K | 1 | 1.50 | 33 |
| PAF-11 | 704 | 77 K | 1 | 1.03 | 34 |
| PAF-18-OH | 1121 | 77 K | 1 | 1.35 | 26 |
| PAF-18-Li | 981 | 77 K | 1 | 1.65 | 26 |
| PAF-19 | 250 | 77 K | 1 | 0.55 | 27 |
| PAF-20 | 702 | 77 K | 1 | 0.89 | 27 |
| JUC-Z2 | 2034 | 77 K | 1 | 1.62 | 36 |
| JUC-Z4 | 793 | 77 K | 1 | 1.25 | 37 |

Commonly utilized porous materials include inorganic carbon materials, porous polymers, zeolites, and MOFs. Both physical and chemical hydrogen storage are generally considered safer and more convenient than traditional hydrogen storage methods. However, metal hydrides, which chemically store hydrogen, require high-pressure conditions for effective storage. In contrast, the physical adsorption method, which operates under milder conditions, typically does not achieve substantial hydrogen storage capacity. From a practical application perspective, physical adsorption of hydrogen storage is more advantageous. Consequently, the development of organic porous materials with a high hydrogen storage capacity has emerged as a prominent focus in current research. POPs possess a high specific surface area and adjustable pore sizes, making them well-suited to meet the performance requirements for hydrogen storage. As such, they are considered promising materials for hydrogen storage.

To meet the stringent hydrogen storage capacity targets set by the DOE, researchers have devoted significant efforts to the synthesis of POP materials with ultrahigh specific surface areas. A comprehensive study has been conducted to explore the relationships between the gravimetric hydrogen storage capacity and the BET surface area of POPs, under both elevated

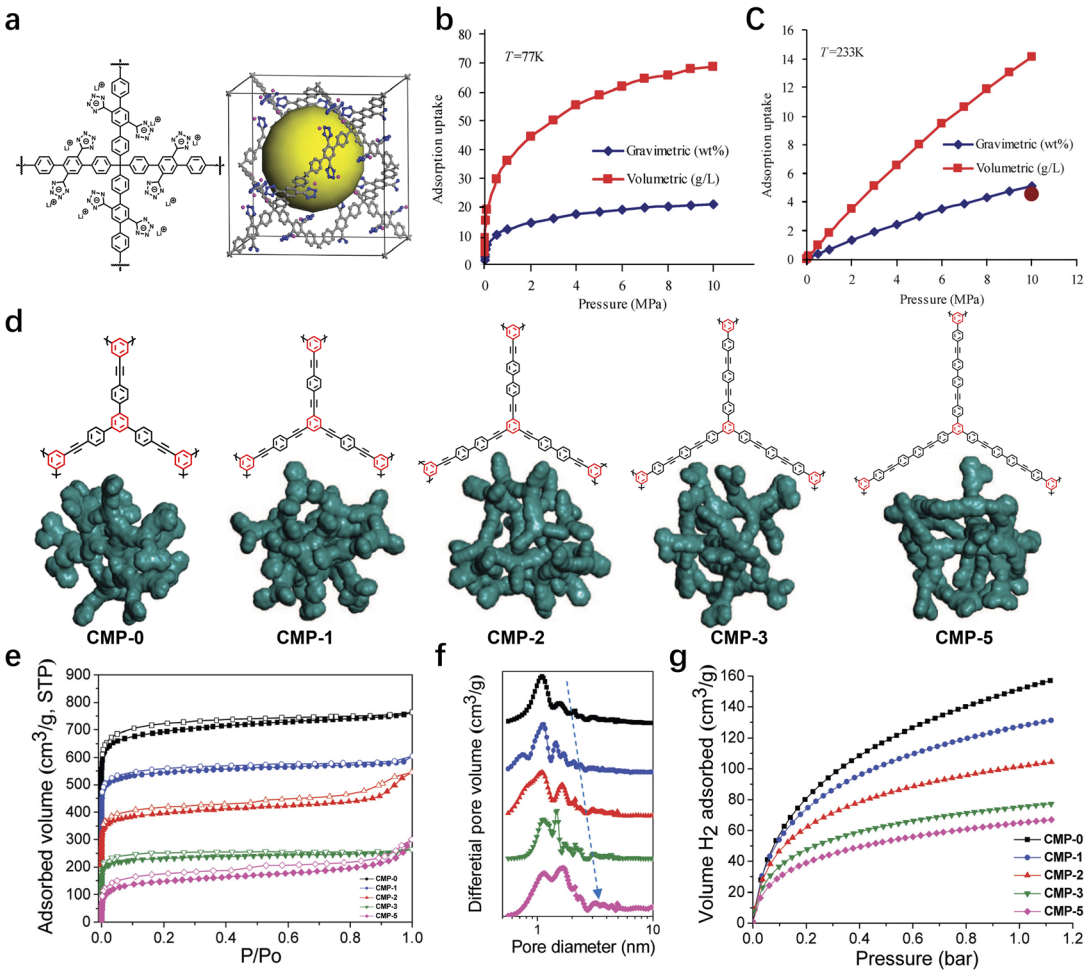


Fig. 7 (a) The building block (left) and unit cell (right) of the PAF-4. Gravimetric and volumetric adsorption isotherms of $H_2$ predicted at (b) 77 and (c) 233 and up to 10 MPa.[73] Copyright 2010 American Chemical Society. (d) Atomistic simulations of network fragments for CMP-0, CMP-1, CMP-2, CMP-3, and CMP-5. (e) $N_2$ adsorption–desorption isotherms measured at 77.3 K. (f) NL-DFT pore size distribution curves. (g) Volumetric $H_2$ adsorption isotherms for CMP-0-5 at 77.3 K.[24] Copyright 2008 American Chemical Society.

and ambient pressure conditions, as detailed in Table 5. The data reveals a clear trend: as the BET surface area of POPs increases, so does their hydrogen storage capacity. For instance, under high-pressure conditions (48–60 bar) and at 77 K, PAF-4, with a BET surface area of 2246 $m^2\ g^{-1}$, exhibits a hydrogen storage capacity of 4.2 wt%.[33] In contrast, PAF-1 with an impressive specific surface area of 5600 $m^2\ g^{-1}$ achieves a hydrogen storage capacity of 7.0 wt% at the same temperature and pressure conditions.[3] PPN-3,[13] with a specific surface area of 2840 $m^2\ g^{-1}$, shows a hydrogen uptake of 4.28 wt%, further validating the positive correlation between surface area and hydrogen storage performance.[56] To further enhance the hydrogen storage capabilities of PAFs, both computational simulations and experimental investigations focusing on lithium (Li)-doping have been carried out. Owing to the presence of multiple binding sites, the hydrogen uptake of PAF-4 is forecast to be exceptional. At 77 K and 100 bar, PAF-4 is predicted to achieve a gravimetric capacity of 20.7 wt% and a volumetric capacity of 68.6 g $L^{-1}$, along with a high binding energy of up to 14.5 kJ $mol^{-1}$ (Fig. 7a–c).[73] Experimentally, PAF-18-OLi, which contains a lithium phenoxide functional group, has been found to have a heat of absorption of 7.6 kJ $mol^{-1}$.[26] This value not only reflects the strength of the interactions between hydrogen molecules and the material but also provides insights into the thermodynamic feasibility of the hydrogen adsorption process.

In parallel with the research on PAFs, significant progress has been made in the synthesis of CMPs for hydrogen storage applications. In 2008, Cooper *et al.* synthesized a series of CMPs by selecting linking units of varying lengths and employing the Sonogashira–Hagihara coupling reaction. The specific surface area and pore size of the target CMP materials were effectively tailored. Notably, CMP-0, which features the shortest linking group, exhibits the highest specific surface area of 1018 $m^2\ g^{-1}$ and a hydrogen storage capacity of 1.4 wt% (Fig. 7d–f).[24] The research group also successfully developed HCMPs *via* the self-coupling reaction of phenylacetylene monomers, catalyzed by a Pd/Cu bimetallic system.[2] Compared to CMPs, HCMPs possess a more intricate pore structure and demonstrate a hydrogen storage capacity of 131 $cm^3\ g^{-1}$. These findings

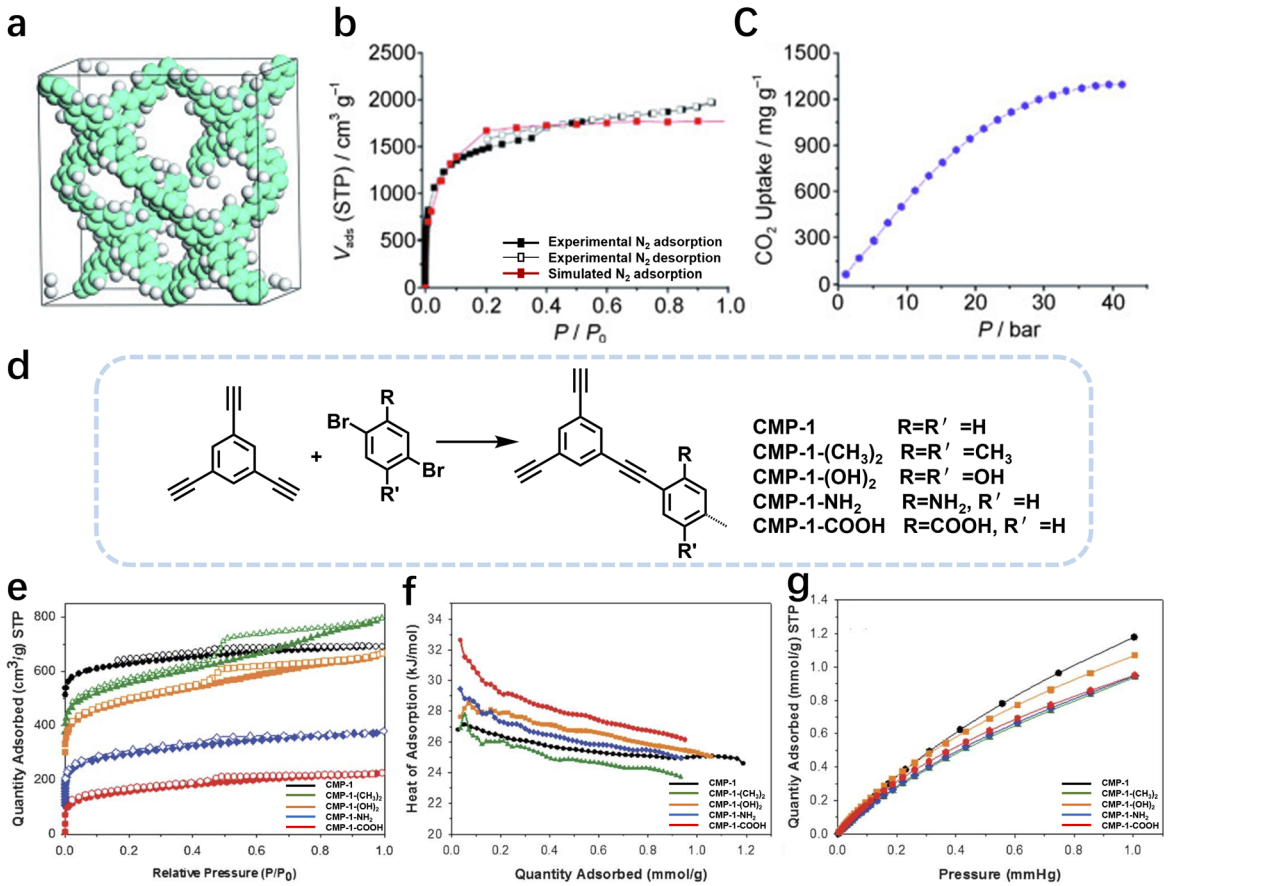


Fig. 8 (a) Structure of PAF-1. (b) $N_2$ adsorption isotherms of PAF-1 at 77 K. (c) Excess high-pressure carbon dioxide adsorption isotherm at 298 K.[3] Copyright 2009 Wiley-VCH GmbH. (d) Synthesis of functionalised CMPs. (e) $N_2$ adsorption/desorption isotherms (77 K) for CMPs, and (f) measured $CO_2$ isotherms at 298 K for CMP networks. (g) Measured isosteric heats of adsorption for $CO_2$ for CMP networks.[80] Copyright 2011 the Royal Society of Chemistry.

highlight the potential of CMPs and HCMPs as promising hydrogen storage materials, demonstrating that through rational design and synthesis, it is possible to tailor the properties of porous organic polymers to meet the demanding requirements of hydrogen storage applications.

**3.1.2 $CO_2$ capture.** In modern society, the extensive combustion of fossil fuels has resulted in increased carbon dioxide emissions, thereby contributing to severe global climate and environmental challenges. Against the backdrop of dual carbon goals, $CO_2$ capture and storage (CCS) has garnered worldwide attention. Currently, the prevalent technology involves the use of liquid organic amine solutions for the chemical absorption of $CO_2$ as the initial step in the capture and storage process. However, the organic amine absorption method is characterized by high corrosivity, environmental unfriendliness, and challenges related to desorption. Consequently, the development of low-energy-consumption and efficient methods for capturing and separating $CO_2$ from mixed gases is of paramount importance.[74–76] POPs exhibit not only a high specific surface area and tunable porosity, which fulfill the physical adsorption requirements for $CO_2$, but they also allow for the introduction of heteroatoms to enhance the adsorption heat of $CO_2$. Functional groups, including imine bonds, triazine rings, carbazole, and porphyrin, are incorporated into POPs to improve their $CO_2$ adsorption performance.[77]

For instance, PAF-1 exhibits excellent carbon dioxide adsorption performance (Fig. 8a).[3] With an ultrahigh BET specific surface area of 5600 $m^2\ g^{-1}$, it provides abundant sites for $CO_2$ adsorption. Additionally, PAF-1 possesses outstanding thermal stability (stable below 520 °C in air) and hydrothermal stability, laying a solid foundation for adsorption applications. At room temperature (298 K) and 40 bar, the $CO_2$ adsorption capacity of PAF-1 reaches 1300 mg $g^{-1}$ (Fig. 8b and c). Combined with its stable characteristics, this performance endows PAF-1 with significant potential in the field of carbon dioxide capture. Furthermore, it possesses outstanding adsorption properties for volatile organic compounds.[3] The introduction of functional groups (*e.g.*, S and –OH), into the CMP-1 skeleton enabled the post-synthetic modification of CMPs. Although the specific surface area of the post-modified CMP-1 is slightly reduced, this post-modification strategy enhances the applicability of CMPs in gas-selective adsorption and increases the number of catalytic active sites.[78]

Inspired by this, Cooper *et al.* synthesized a series of CMPs containing functional groups (*e.g.* $–NH_2$, –OH, and –COOH) through the Sonogashira–Hagihara coupling reaction

(Fig. 8d).[80] The results indicate that under low pressure (1 atm) and near-ambient temperature conditions, the chemical composition of the materials has a much greater impact on $CO_2$ adsorption capacity than the specific surface area (Fig. 8e). Among them, the carboxyl-functionalized CMP-1-COOH exhibits the highest isosteric heat of $CO_2$ adsorption, 32.6 kJ mol$^{-1}$. The order of adsorption heat for each material is –COOH > –$(OH)_2$ > –$NH_2$ > H > –$(CH_3)_2$ (Fig. 8f). The non-functionalized CMP-1 achieves the highest volumetric $CO_2$ adsorption capacity (1.18 mmol g$^{-1}$) at 298 K and 1 bar (Fig. 8g). However, $CO_2$ adsorption capacity depends not only on the specific surface area or pore volume but also on the type of functional groups and pore size, which play crucial roles. This study confirms that carboxyl functional groups are excellent design targets for $CO_2$ capture materials, providing a valuable reference for the optimization of related adsorbents.

**3.1.3 Methane adsorption.** Among the diverse energy sources available, methane has emerged as a highly promising and sought-after clean and efficient energy option. As the principal component of natural gas, methane is also abundantly present in unconventional natural gas resources, such as coal bed methane and shale gas. Its advantages include vast reserves, a high combustion calorific value, and relatively low pollutant emissions upon combustion, making it a linchpin in the pursuit of sustainable energy development and in combatting climate change. Traditional methane storage methods predominantly rely on high-pressure compression or low-temperature liquefaction. High-pressure compression requires methane to be stored under extremely high pressures, imposing rigorous demands on storage equipment. This not only poses significant safety risks, as the high-pressure vessels are prone to leakage or explosion under improper conditions, but also consumes substantial amounts of energy during the compression process. On the other hand, low-temperature liquefaction involves cooling methane to cryogenic temperatures, which presents its own set of challenges. The process demands sophisticated and costly cooling systems, and maintaining low temperatures require continuous energy input. Moreover, the handling of liquefied methane requires specialized infrastructure and safety protocols. Collectively, these limitations have underscored the urgent need for the development of novel and efficient methane storage technologies.[79]

POPs have demonstrated unique and significant advantages in the field of methane adsorption. The high customizability of POPs enables researchers to precisely tailor their pore structures, specific surface areas, and surface chemical properties. By strategically selecting organic monomers and adopting diverse synthesis strategies, the pore structures of POPs can be tailored

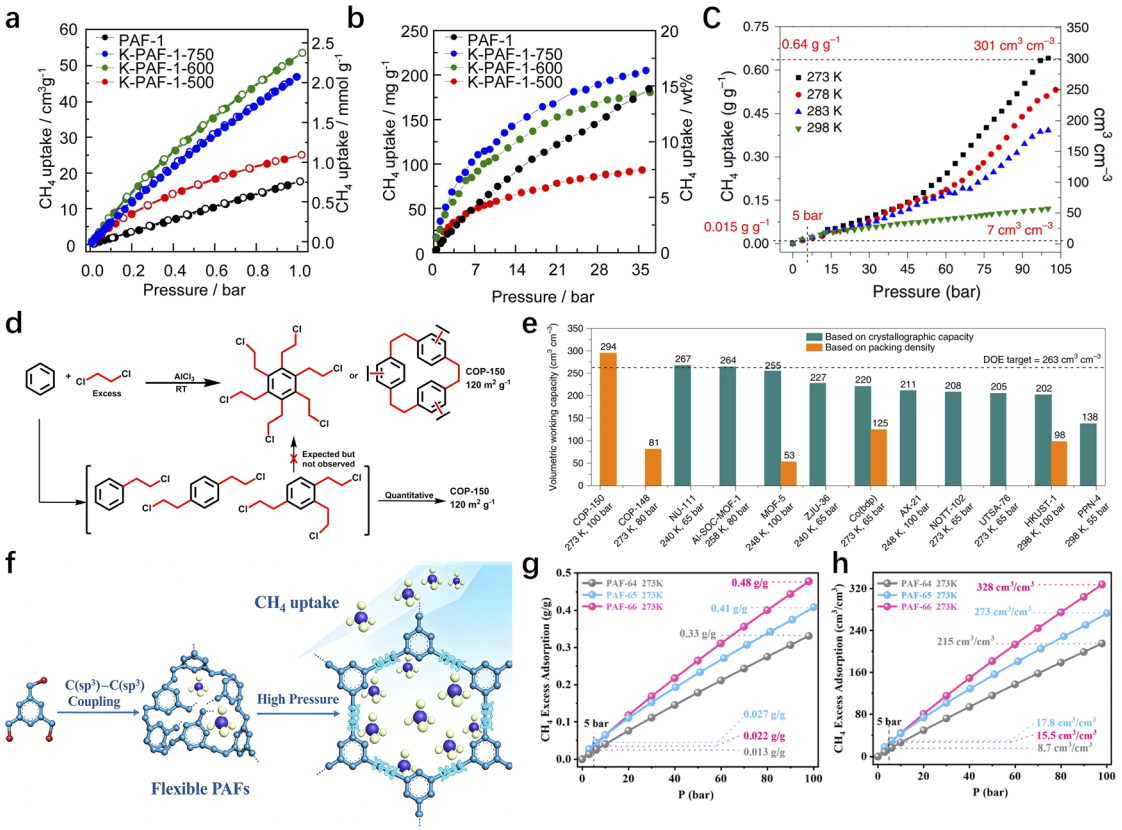


Fig. 9 (a) $CH_4$ uptake of PAF-1 and KOH-activated samples at 273 K and 1 bar. (b) High pressure $CH_4$ uptake of KOH-activated samples at 298 K.[85] Copyright 2013 Springer Nature. (c) Methane adsorption isotherms of COP-150 at four different temperatures. (d) The synthesis of COP-150. (e) Comparison of highest reported volumetric working capacities.[62] Copyright 2019 Springer Nature. (f) Schematic diagram of PAF-64 high-pressure $CH_4$ adsorption. (g) Gravimetric $CH_4$ adsorption isotherms of PAFs at 273 K. (h) Volumetric $CH_4$ adsorption of PAFs at 273 K.[12] Copyright 2024 the Royal Society of Chemistry.

to optimize methane adsorption. For instance, the size and shape of the pores can be designed to match the kinetic diameter of methane molecules, facilitating efficient capture and retention. Additionally, the surface chemistry of POPs can be modified to enhance the interaction with methane, such as *via* the incorporation of functional groups with affinity for methane. Furthermore, POPs generally exhibit excellent chemical and thermal stability, enabling them to maintain their structural integrity in a wide range of complex environments. This stability ensures that they are effectively utilized in diverse application scenarios, from stationary storage facilities to mobile energy systems. Among POPs, PAF materials have proven to be particularly effective methane adsorbents, owing to their ultrahigh specific surface areas and robust structural stability.

KOH-activated carbonized PAF-1 derived materials (K-PAF-1 series) exhibit exceptional gas adsorption performance, with their core advantage stemming from the synergistic effect of the unique bimodal microporous structure (0.6 nm and 1.2 nm) and high specific surface area (up to 2926 $m^2\ g^{-1}$), enabling efficient gas storage under both low and high pressure conditions.[85] KOH-activated PAF-1 derivatives exhibit excellent methane adsorption performance. Under low-pressure conditions (273 K, 1 bar), K-PAF-1-600 achieves an adsorption capacity of 53.5 $cm^3\ g^{-1}$ (3.7 wt%) with the isosteric heat of adsorption ($Q_{st}$) enhanced to 15.9–20.6 kJ $mol^{-1}$, outperforming the pristine PAF-1 (Fig. 9a). Under high pressure, K-PAF-1-750 delivers the best performance, 207 mg $g^{-1}$ of $CH_4$ at 35 bar, which is superior to that of the original PAF-1 (Fig. 9b).

Recently, Liu *et al.* developed a series of PAFs (PAF-64, PAF-65, and PAF-66) *via* $C(sp^3)$–$C(sp^3)$ coupling reactions, and these PAFs exhibit excellent methane adsorption performance (Fig. 9c).[12] Their core advantage stems from the synergistic effect of flexible frameworks and porous structures. These materials possess favorable specific surface areas (up to 390 $m^2\ g^{-1}$), and PAF-66 is dominated by a microporous structure (1.23 nm). Moreover, their frameworks exhibit pressure-triggered swelling properties, providing ample active sites for methane adsorption. The flexible PAF-64, PAF-65 and PAF-66 exhibit outstanding gravimetric working capacity (5–100 bar) of 0.32 g $g^{-1}$, 0.38 g $g^{-1}$ and 0.46 g $g^{-1}$, respectively, at 273 K (Fig. 9d). At the same condition, PAF-64, PAF-65, and PAF-66 demonstrate outstanding volumetric working capacity of 206, 255, and 313 $cm^3\ cm^{-3}$, respectively (Fig. 9e). The volumetric working capacity of PAF-66 exceeds the U.S. DOE target by 19%, ranking among the top performers of reported porous materials. The adsorption performance of these materials is positively correlated with flexibility and specific surface area, and PAF-66 achieves the optimal adsorption capacity owing to its superior structural flexibility and higher specific surface area. Additionally, these PAF materials exhibit excellent acid-base stability and thermal stability (10% weight loss temperature >442 °C), enabling them to resist interference from impurities in natural gas. They possess extremely high application value in adsorbed natural gas (ANG) storage, offering a new pathway for the design of high-efficiency methane storage materials.

Yavuz and co-workers synthesized alkane-linked flexible porous aromatic network polymers on a large scale *via* the Friedel–Crafts alkylation reaction, using benzene and 1,2-dichloroethane as the starting materials (Fig. 9d).[62] The representative COP-150 exhibits excellent performance and great practical application potential in the field of methane adsorption and storage, benefiting from the synergistic structural features of its aromatic ring skeleton and ethylene flexible linkers. This material possesses high ultramicroporosity in the ground state and achieves dynamic pore opening and closing *via* a pressure-triggered framework swelling effect. The pores are closed at low pressure, while at high pressure, the framework swells to open the pores and generate new adsorption sites, thus enabling efficient and reversible methane adsorption. Under the cyclic conditions of 273 K and 100 bar, COP-150 delivers a gravimetric methane working capacity of 0.625 g $g^{-1}$ and a volumetric working capacity of 294 $cm^3\ cm^{-3}$ (Fig. 9c), surpassing the targets set by the U.S. DOE by 25% and 12%, respectively (Fig. 9e). Moreover, its working capacity accounts for 98% of the total adsorption capacity, representing an extremely high adsorption utilization efficiency. Such flexible COP materials synthesized *via* $C(sp^2)$–$C(sp^3)$ coupling have broken through the pressure bottleneck of methane adsorption in traditional rigid porous materials, providing a novel strategy for the structural design of methane storage materials.

### 3.2 Gas separation

The purification of gas holds substantial importance in industrial applications. The separation of gas (*e.g.*, $N_2$, $CO_2$, $H_2$, and $CH_4$) is closely correlated with the pore size distribution of porous materials. Despite its small kinetic diameter (0.33 nm), the selective capture of $CO_2$ presents significant challenges.[81] Consequently, the selective separation of $CO_2$ from $N_2$, $CH_4$, and other gas has emerged as a pivotal research direction.

POPs exhibit tremendous potential for gas separation, thanks to their unique pore structure, high specific surface area, excellent chemical and thermal stability, and tunable composition. By introducing rigid conjugated units, POPs constructed through different C–C coupling reactions feature stable three-dimensional network structures with tunable pore sizes, making them ideal candidates for gas separation. Their high specific surface area and adjustable pore sizes facilitate efficient gas capture and separation. For example, Han *et al.* utilized the oxidative self-coupling polymerization of 1,3,5-tris(9-carbazolyl) benzene to synthesize porous polycarbazole, which exhibits a high specific surface area ($S_{BET} = 2220\ m^2\ g^{-1}$).[48] At 273 K and 1 bar, the polymer demonstrates an adsorption selectivity of 33 for $CO_2/CH_4$ and 25 for $CO_2/N_2$. Similarly, CMPs constructed *via* $C(sp^2)$–$C(sp)$ coupling reactions can also achieve efficient gas adsorption and separation due to their regular microporous structures. NUT-15 exhibits a specific surface area of 415 $m^2\ g^{-1}$ and an exceptional $CO_2$ adsorption capacity, along with a $CO_2/CH_4$ adsorption selectivity of up to 12.4 at 273 K.[14] The structural designability of POPs enables precise regulation of pore size and pore microenvironment for the selective adsorption of target gas.

Continuous microporous membranes are widely studied for gas separation, due to their low energy premium and strong molecular specificity. Tian *et al.* fabricated a defect-free continuous iPAF-5 membrane through surface-initiated C($sp^2$)–C(sp) coupling polymerization.[82] Both pore size and chemistry of the PAF membrane were modified by ion-exchange, resulting in good selectivity and permeance for the gas mixtures $H_2/N_2$ and $CO_2/N_2$. The membrane with Br-as a counter ion in the framework exhibited a $H_2/N_2$ selectivity of 72.7 with a $H_2$ permeance of 51 844 gas permeation units (GPU). When the counter ions were replaced by $BF_4^-$, the membrane showed a $CO_2$ permeance of 23 058 GPU, and an optimized $CO_2/N_2$ selectivity of 60.0. Such cationic PAF continuous membranes synthesized *via* the C($sp^2$)–C(sp) coupling reaction hold important application prospects in the industrial gas separation fields such as hydrogen purification, $CO_2$ capture from flue gas. Thus, they provide a universal strategy for the functional design and precise regulation of porous organic framework membranes.

Liu *et al.* prepared a series of novel three-dimensional PAFs by reacting tetrakis (4-alkynylphenyl)methane with 1,4-dibromobenzene with various functional groups.[15] The functionalized porous aromatic framework materials (cPAF-28 and iPAF-28) prepared in this work exhibit excellent separation performance for acetylene/ethylene (Fig. 10a). Compared with the non-functionalized PAF-28, both materials exhibit significantly enhanced separation performance *via* modification with carbene or imidazolium groups. As shown in Fig. 10c–e, the acetylene adsorption capacities of cPAF-28 and iPAF-28 reach 48 $cm^3\ g^{-1}$ and 57 $cm^3\ g^{-1}$, respectively, at 273 K and 100 kPa, which are much higher than those of PAF-28 (37 $cm^3\ g^{-1}$). Furthermore, the acetylene/ethylene selectivity increases from 1.8 to 12.2 and 15.4 at 298 K and 100 kPa (Fig. 10b). In dynamic breakthrough experiments (Fig. 10f–h), iPAF-28 retains acetylene for over 10 minutes, exhibiting an ultrahigh selectivity of

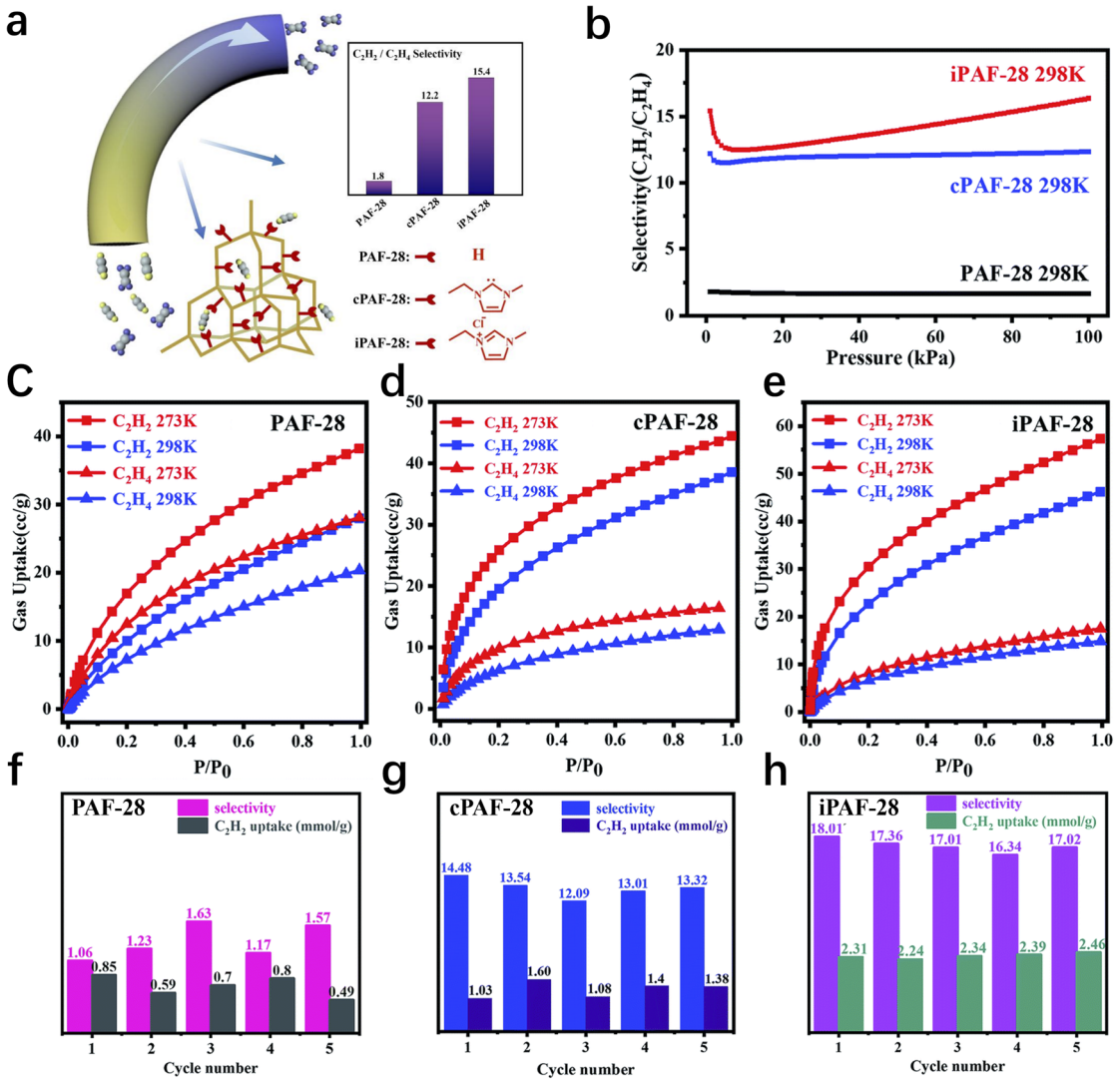


Fig. 10 (a) Schematic diagram of $C_2H_2/C_2H_4$ separation for PAFs. (b) The selectivity of $C_2H_2/C_2H_4$ predicted by IAST for PAFs at 298 K. (c–e) $C_2H_2/C_2H_4$ adsorption isotherms at 273 K and 298 K for PAFs ($P_0 = 100$ kPa). (f–h) Recyclability of PAFs in terms of $C_2H_2/C_2H_4$ selectivity and $C_2H_2$ capacity.[15] Copyright 2022 the Royal Society of Chemistry.

18.01 and a dynamic adsorption capacity of 2.3 mmol $g^{-1}$, which is consistent with the static adsorption test results. These materials exhibit good thermal stability up to 300 °C, and their performance remains unchanged after five cycles, integrating high selectivity, high adsorption capacity, and excellent recyclability. Moreover, the separation process is low-energy-consuming and environmentally friendly, offering an ideal material candidate for the efficient acetylene/ethylene separation in the petrochemical industry.

Additionally, PAFs constructed *via* $C(sp^3)$–$C(sp^3)$ coupling reactions exhibit excellent performance in gas alkane separation, benefiting from their unique structural features and excellent chemical stability. Liu *et al.* synthesized the porous polyadamantane (PPA) (Fig. 11a), which exhibits remarkable performance in the separation of $C_1$–$C_3$ alkanes.[23] As the first alkane-based porous organic polymer prepared *via* $C(sp^3)$–$C(sp^3)$ homocoupling, it possesses a BET specific surface area of 681 $m^2$ $g^{-1}$, featuring a bimodal microporous structure (0.5 nm and 1.2 nm) along with abundant mesopores. At 273 K and 100 kPa, the adsorption capacities for propane, ethane, and methane are 1.61, 0.58, and 0.17 mmol $g^{-1}$, respectively (Fig. 11b). The isotherms are fitted using the virial equation, and the isosteric heat of gas adsorption ($Q_{st}$) is calculated as 24.5, 35.0 and 37.7 kJ $mol^{-1}$ for $CH_4$, $C_2H_6$ and $C_3H_8$, respectively (Fig. 11c), confirming that PPA exhibits higher affinity for $C_3H_8$ and $C_2H_6$ than for $CH_4$. The ideal adsorbed solution theory (IAST) selectivity for $C_3H_8/CH_4$ $C_2H_6/CH_4$ binary mixtures (1 : 1, v/v) at 298 K and 100 kPa (1 bar) are calculated to be as high as 317 and 13, respectively (Fig. 11d). In dynamic breakthrough experiments, PPA enables the effective separation of these three alkanes under different flow rates, with propane exhibiting the longest retention time (Fig. 11e–g). Notably, the performance remains unchanged after five cycles. Combining high selectivity, large adsorption capacity, excellent stability, acid-base resistance, and strong hydrophobicity, PPA offers an efficient material for industrial applications, such as natural gas purification.

### 3.3 Catalysis

POPs constructed *via* carbon–carbon coupling exhibit tremendous application potential for the field of catalysis, particularly in photocatalysis and heterogeneous catalysis, owing to their unique structural characteristics such as high specific surface area, abundant active sites, precisely tunable pore structures, and excellent chemical and thermal stability. Through carbon–carbon coupling strategies including C(sp)–C(sp) and $C(sp^2)$–$C(sp^2)$ couplings, the precise regulation of the framework composition and electronic structure of POPs can be achieved, thereby optimizing their light-harvesting capacity and charge separation efficiency and enabling them to serve as high-performance photocatalytic materials. POPs have been widely applied in scenarios such as organic transformation reactions, photocatalytic degradation of pollutants, and photocatalytic water splitting for hydrogen production. In the field of

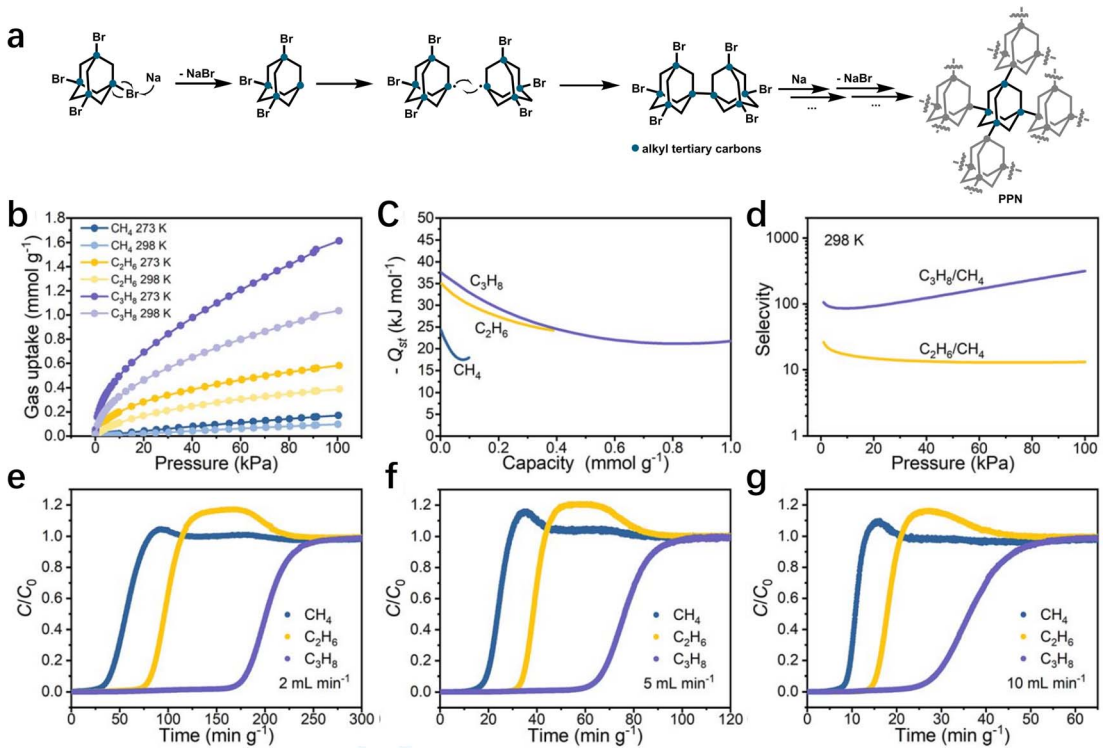


Fig. 11 (a) Proposed mechanism for the construction of PPA from 1,3,5,7-tetrabromoadamantane. (b) $CH_4$, $C_2H_6$ and $C_3H_8$ adsorption isotherms for PPA. (c) $Q_{st}$ of PPA towards $CH_4$, $C_2H_6$ and $C_3H_8$. (d) IAST adsorption selectivity of PPA towards equimolar mixtures of $C_3H_8/CH_4$ and $C_2H_6/CH_4$. (e–g) Breakthrough experiments of PPA for $CH_4/C_2H_6/C_3H_8$ (V/V/V = 85/10/5) mixture at different flow rate.[23] Copyright 2026 Science China Press.

heterogeneous catalysis, the rigid frameworks and immobilizable active sites of POPs allow them to act directly as both stable catalytic supports and heterogeneous catalysts. By introducing metal ions or functional organic groups into the POP frameworks, materials with specific catalytic properties can be constructed, which are widely suitable for catalytic processes such as $CO_2$ resource utilization and conversion, redox reactions, and carbon–carbon coupling reactions. Thus, POPs constructed based on carbon–carbon coupling reactions, through sophisticated structural design and functional modification, can achieve efficient and sustainable chemical transformations in the fields of photocatalysis and heterogeneous catalysis, providing a highly promising innovative solution for addressing global issues such as energy shortage and environmental pollution.

**3.3.1 Photocatalysis.** POPs have emerged as promising candidates in photocatalysis, owing to their unique structural and functional attributes. Their exceptional structural stability ensures long-term durability under reaction conditions, while their strong visible-light absorption capability and microporous features arising from cross-linked frameworks significantly boost their catalytic performance. These features not only increase the specific surface area of the POPs, exposing abundant photocatalytic active sites, but also facilitate water splitting driven by photogenerated electrons, thereby improving their photocatalytic hydrogen evolution efficiency.[83,84]

The exploration of POPs in photocatalysis began with seminal work by Cooper and colleagues. They harnessed pyrene and benzene rings as fundamental building units to design and synthesize a series of CMPs *via* Suzuki coupling copolymerization.[16] Among these, CP-CMP10 stands out with the most promising photocatalytic hydrogen production performance, achieving a hydrogen evolution rate of 17.4 ± 0.9 μmol $h^{-1}$ without noble metal co-catalysts and demonstrating excellent cycle stability. This success spur further investigations into the structure–activity relationships of CMPs. In 2016, this research group delved deeper into the influence of different building units and monomer linkage lengths on photocatalytic performance. By using benzene and spirobifluorene as core building units in the Suzuki–Miyaura coupling reaction, they synthesized a new series of CMPs.[86] The results show that SP-CMP, constructed from spirobifluorene and benzene monomers, exhibited optimal photocatalytic hydrogen production activity under visible light ($\lambda > 420$ nm) without noble metal co-catalysts. With a hydrogen evolution rate of 3.0 μmol $h^{-1}$, it significantly

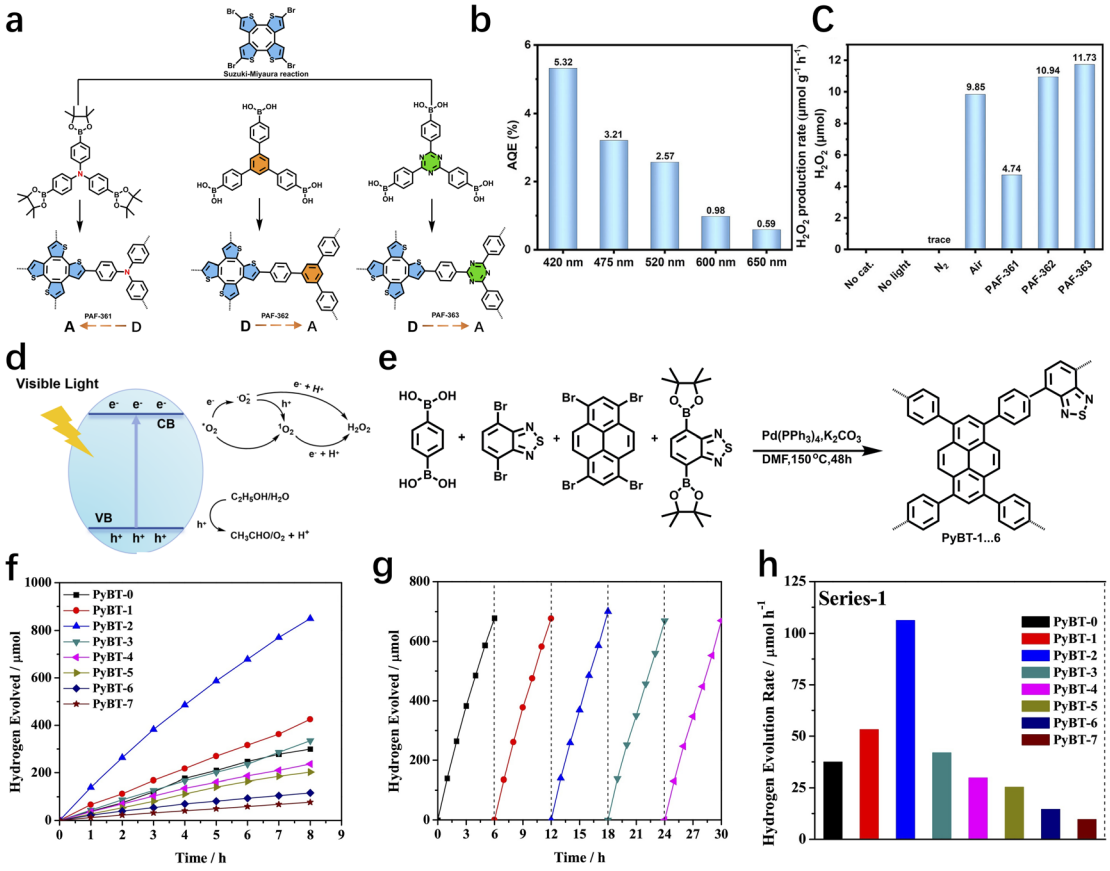


Fig. 12 (a) Synthetic routes of COTh-PAFs. (b) The AQE of PAF-363 under different wavelengths. (c) The photocatalytic activities of COTh-PAFs. (d) The AQE of PAF-363 under different wavelengths.[91] Copyright 2024 Wiley-VCH GmbH. (e) Synthetic routes to the polymers. (f) Time course of hydrogen evolution of the CMP photocatalysts with 3 wt% Pt from water containing 20 vol% triethanolamine under UV-vis light irradiation. (g) Stability test of PyBT-2 with 3 wt% Pt from water containing 20 vol% triethanolamine over a time period of 30. (h) HER of the CMP photocatalysts with 3 wt% Pt under UV-vis light irradiation.[88] Copyright 2018 Elsevier B.V.

outperforms other polymers, such as extended analogue of spirobifluorene conjugated microporous polymers (ESP-CMP) synthesized from spirobifluorene and biphenyl. The superior performance of spirobifluorene conjugated microporous polymers (SP-CMP) can be attributed to its enhanced rigidity and planarity, which facilitate the transport of photogenerated excitons and suppress electron–hole pair recombination, optimizing the photocatalytic process. Yu *et al.* synthesized a series of carbazole-based CMPs with tunable redox potentials by anchoring carboxylic acid groups and amide derivatives.[87] Its redox potential can be regulated by adjusting the core structure, among which CMP-CSU6 exhibits the strongest oxidative capacity and optimal photocatalytic activity. Driven by visible light, this material can efficiently catalyze the C-3 formylation and thiocyanation of indoles. Under room temperature conditions, the maximum product yields reach 90% and 98% respectively, without the need for strong acids, strong bases, or strong oxidants. The material shows good tolerance to indole substrates with different substituents (electron-donating, electron-withdrawing, or halogen groups), is not affected by steric hindrance at the C-2 position, and the reaction has high regioselectivity. In addition, the catalyst is easy to recover and can be reused at least five times without significant decline in catalytic activity, featuring both environmental friendliness and practicality.

Building on these foundational studies, Jiang *et al.* achieved notable breakthroughs in the field. In 2018, they rationally designed CMPs with different electronic structures by using electron-rich planar pyrene as the electron donor, benzene or biphenyl as the π-linker, and benzothiadiazole as the electron acceptor.[88] Through Suzuki–Miyaura coupling copolymerization, a series of CMPs with D–π–D, D–π–A, D–A, and π–A structures were synthesized (Fig. 12e). Under UV-vis light irradiation ($\lambda > 300$ nm) with triethanolamine (TEOA) as the sacrificial agent, the photocatalytic hydrogen evolution activity of D–π–A type polymers is significantly superior to that of D–π–D type and D–A type polymers. PyBT-2 (with a pyrene-to-benzothiadiazole molar ratio of 9 : 2) exhibits optimal performance (Fig. 12f). The hydrogen evolution rate (HER) of the bare catalyst reaches 52.5 μmol $h^{-1}$, and it further increases to 106.2 μmol $h^{-1}$ upon loading 3 wt% Pt as a cocatalyst, which is superior to most reported organic photocatalysts (Fig. 12h). This class of materials possesses high specific surface area, excellent thermal stability, and broad-spectrum absorption characteristics. After a 30-hour cyclic test, the catalytic activity shows no significant attenuation, demonstrating outstanding structural stability (Fig. 12g). Additionally, the batch synthesis demonstrates good reproducibility, providing a practical solution for efficient organic photocatalytic hydrogen production. The D–π–A structure is crucial for enhancing catalytic performance: the electron push–pull effect between pyrene (donor) and benzothiadiazole (acceptor) promotes the separation of photogenerated electron–hole pairs. The extended π-conjugated structure accelerates the migration of charges from the bulk to the surface, while the porous structure enhances light harvesting through multiple scattering and simultaneously provides abundant active sites.

Other research groups also explored the diverse applications of POPs in photocatalysis. Kailasam *et al.* first synthesized Tx-CMP with high specific surface area, large pore volume, narrow bandgap, and good stability *via* Suzuki cross-coupling reaction.[89] A novel truxene (Tx) based conjugated microporous polymer (Tx-CMP) exhibits excellent photocatalytic performance driven by natural sunlight. It shows outstanding activity in the oxidative homocoupling of benzylamine, achieving a conversion rate of over 99%, a yield of 90%, and a TOF of 12.4 mmol $g^{-1}$ $h^{-1}$ within 4 hours, with catalytic activity superior to that of $TiO_2$ and (mesoporous carbon nitride) SG-CN. The catalyst exhibits broad applicability. It can efficiently catalyze benzylamines substituted with electron-withdrawing or electron-donating groups, as well as heterocyclic amines (*e.g.*, furfurylamine), with conversions ranging from 77% to 98% and selectivities from 80% to 95%. However, it has no catalytic effect on aliphatic amines. It also demonstrates excellent cyclic stability, maintaining high conversion and yield after five cycles, with its structure and specific surface area remaining basically stable. During the reaction, Tx-CMP absorbs natural sunlight to generate charge carriers, and molecular oxygen is converted into reactive oxygen species, which synergistically oxidize amines to form imines. No metals or cocatalysts are required, making the process environmentally friendly. Its good recyclability further highlights the potential of POPs in sustainable catalytic processes. Similarly, Chen *et al.* synthesized polybenzothiadiazole *via* the Sonogashira–Hagihara cross-coupling polymerization reaction, which exhibits bifunctional activity toward both photocatalytic hydrogen evolution and pollutant degradation.[90] When this polymer is combined with $TiO_2$ to construct poly(benzothiadiazole) (BBT)/$TiO_2$ heterojunctions, the catalytic performance is significantly enhanced, primarily owing to the accelerated transfer of photogenerated electrons at the heterojunction interface. Collectively, these studies have broadened the application scope of POPs in photocatalysis, extending from hydrogen evolution to environmental remediation.

Zhu *et al.* selected three monomers with different electron-donating groups, including triphenylamine (TPA), 1,3,5-triphenylbenzene (TPB), and 2,4,6-triphenyltriazine (TPTA), and combined them with cyclooctatetrathiophene (COTh) groups to construct three donor–acceptor (D–A) type porous aromatic frameworks linked *via* carbon–carbon bonds, named PAF-361, PAF-362, and PAF-363, respectively (Fig. 12a).[91] These frameworks possess unique extended saddle-shaped structures. Among them, PAF-363 exhibits the optimal performance. Notably, the generation of $H_2O_2$ is completely inhibited in the absence of either light or COTh-PAFs photocatalysts, which emphasizes the crucial role of COTh-PAFs as photocatalysts (Fig. 12c). Under visible light irradiation ($\lambda > 420$ nm), with water and oxygen as raw materials, PAF-363 achieves an $H_2O_2$ production rate of 11 733 μmol $g^{-1}$ $h^{-1}$ in the presence of a sacrificial agent, and maintains a production rate of 3930 μmol $g^{-1}$ $h^{-1}$ even in the absence of a sacrificial agent. The apparent quantum efficiency at 420 nm wavelength is 5.32% (Fig. 12b), which is significantly higher than those of PAF-361 and most reported porous organic semiconductors. Its high

efficiency stems from the rational design of the D–A structure, which aligns the charge transfer sites with the $O_2$ adsorption sites (both concentrated at the C=CH sites of the COTh fragments), thereby promoting $H_2O_2$ generation *via* a one-step two-electron oxygen reduction reaction (ORR) pathway. In the absence of sacrificial agents, the four-electron water oxidation (WOR) pathway is also involved, generating $H^+$ and $O_2$ to further assist $H_2O_2$ synthesis (Fig. 12d). Moreover, the material exhibits excellent stability, with its structure and catalytic activity remaining essentially unchanged after cyclic use. The generated $H_2O_2$ can also degrade methyl blue through the Fenton reaction, demonstrating potential applications in green chemical synthesis and environmental purification.

This group synthesized PAF-380 and PAF-381 *via* the palladium-catalyzed Suzuki–Miyaura cross-coupling reaction of 2,6-bis(pinacolatoboryl)anthraquinone and 2,6-bis(pinacolatoboryl)naphthalene with tris(4-bromophenyl) amine.[92] By tuning the acceptor units, researchers regulate the specific surface area, light absorption range, and optical band gap of the materials, thereby enhancing their photocatalytic activity. Compared with PAF-381, PAF-380 exists a stronger push–pull effect between the electron-donating triphenylamine groups and the more electron-accepting anthraquinone groups, which is beneficial to the separation of charge carriers. Under 460 nm blue light irradiation, PAF-380 exhibits excellent catalytic activity for the synthesis of benzimidazoles with broad substrate compatibility, and the maximum yield reaches 99%. In addition, PAF-380 exhibits excellent recyclability. After 10 cycles of use, its structure and morphology remain stable, and its catalytic activity shows no significantly attenuation, with the target product yield reaching as high as 94%. Overall, this work proposes a viable strategy for fabricating PAF-based catalytic materials, further expanding the application scope of PAF materials in the field of photocatalysis.

Zhu *et al.* synthesized three AQ-PAFs (PAF-377, PAF-378, and PAF-379) by linking anthraquinone (AQ)-derived boronic esters with bromo-substituted thiophene derivatives (thienothiophene, benzotrithiophene, and cyclooctatetrathiophene (COTh)) *via* the Suzuki–Miyaura cross-coupling reaction.[93] Among them, the 3D conjugated PAF-379 is constructed *via* the alternating donor–acceptor (D–A) coupling of electron-donating cyclooctatetrathiophene (COTh) and electron-accepting anthraquinone (AQ) fragments. This structure ensures efficient charge separation and transfer upon visible light excitation while conferring superhydrophilicity to the material. Under visible light irradiation ($\lambda > 420$ nm), with water and air as the sole raw materials and without any organic sacrificial agents, PAF-379 reaches an $H_2O_2$ production rate of 7124 μmol $g^{-1}$ $h^{-1}$, which is significantly higher than that of PAF-377 (1409 μmol $g^{-1}$ $h^{-1}$) and PAF-378 (1748 μmol $g^{-1}$ $h^{-1}$). This performance surpasses that of most reported organic semiconductor photocatalysts. This study provides a viable strategy for constructing water-dispersible anthraquinone-based organic semiconducting materials, which have tunable charge mobility and tailored pore chemistry properties and can be used for efficient photocatalytic synthesis of $H_2O_2$.

Tao *et al.* synthesized a series of tetraphenylsilane-based porous aromatic frameworks (TEPS-PAFs) *via* the Sonogashira–Hagihara cross-coupling reaction.[94] Notably, tetraphenylsilane (TEPS, as the electron donor) and triphenyltriazine

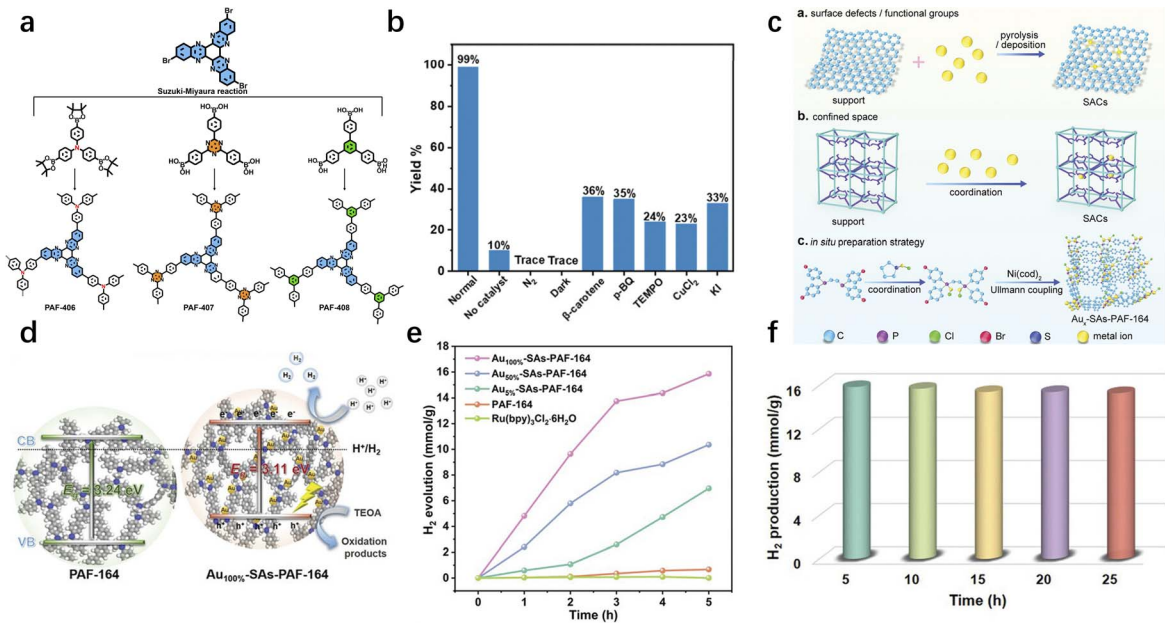


Fig. 13 (a) Synthetic routes of COTh-PAFs. (b) Schematic illustration of different synthetic strategies for the preparation of SACs.[95] Copyright 2025 the Royal Society of Chemistry. (c) Control experiments using the PAF-406 catalyst under various conditions. (d) Schematic illustration of photocatalytic $H_2$ production of PAF-164 and Aux-SAs-PAF-164 under visible light irradiation. (e) Photocatalytic activities for $H_2$ evolution per unit mass. (f) Five cycles of $H_2$ production by Au100%-SAs-PAF-164. Each run took 5 h of continuous light exposure.[96] Copyright 2024 Wiley-VCH GmbH.

fragments (as the electron acceptor) are bridged by an acetylene group to form a well-defined donor-π-acceptor (D–π–A) conjugated framework PAF-405, which exhibits strong electron affinity. This unique characteristic helps promote photoinduced charge separation and electron transfer reactions, thereby facilitating the overall photocatalytic reaction. Under optimized conditions (5.0 mg PAF-405, THF as solvent, air atmosphere, 25 W blue light irradiation at 420 nm), it can efficiently catalyze the C-3 thiocyanation of indoles, achieving a yield as high as 99% with broad substrate compatibility. In addition, PAF-405 exhibits good recyclability, retaining a yield of over 80% after 5 consecutive catalytic cycles. The morphology and chemical composition of the recovered catalyst remain essentially unchanged, demonstrating excellent stability and chemical stability. This study expands the application scope of PAF materials in photocatalytic organic transformations.

Furthermore, this group reported the rational design and synthesis of donor–acceptor (D–A) type PAFs incorporating hexaazatrinaphthylene units for the photocatalytic synthesis of 2-benzothiazoles (Fig. 13a).[95] The porosity, photoelectrochemical properties, energy levels, and band gaps of HATN-PAFs can be readily tuned by modifying the linking fragments. PAF-406 exhibits the optimal photocatalytic performance. As shown in Fig. 13b, light, air, and the PAF-406 catalyst are key reaction conditions and prerequisites for core active species generation. Without PAF-406, the yield is merely 10% (attributed to the photoinduced self-coupling of 2-aminothiophenol). Upon the addition of scavengers for reactive oxygen species (ROS) and photogenerated charge carriers to the reaction system, the reaction yield significantly decreases to 24–36%. This confirms that superoxide radical anions ($O_2^{\bullet -}$), singlet oxygen, as well as photogenerated electrons ($e^-$) and holes ($h^+$), are the core species driving the reaction, providing direct experimental evidence for the synergistic catalytic mechanism involving the dual pathways of energy transfer (ET) and single electron transfer (SET). The rational design of PAF catalytic materials based on HATN fragments could afford efficient photocatalysts for benzothiazole synthesis.

Zhu *et al.* synthesized PAF-164 *via* Yamamoto cross-coupling and immobilized ultrahigh-content gold (Au) single atoms on its surface, with a loading of up to 45.3 wt%, which is leading among currently reported related materials.[96] Strong coordination interactions are established between the phosphorus sites in PAF-164 and Au single atoms, and this unique coordination structure significantly enhances light absorption capability and photogenerated charge separation efficiency (Fig. 13c). Under simulated sunlight (AM 1.5 G), $Au_{100\%}$-SAs-PAF-164 exhibits the optimal performance, with a hydrogen evolution rate of 4.82 mmol $g^{-1}$ $h^{-1}$ and a cumulative hydrogen production of 15.27 mmol $g^{-1}$ after 5 hours of irradiation (Fig. 13e). This performance is significantly superior to that of low-loading samples and most porous material-based catalysts. Notably, the catalyst maintains stable activity without obvious structural changes even after 5 consecutive cycles (Fig. 13f). As electron transporters, Au single atoms rapidly capture photogenerated electrons from the conduction band and accumulate them on the surface, which reduces charge transfer resistance and suppresses electron–hole recombination. The electrons concentrated on the surface of Au single atoms further reduce $H^+$ to $H_2$, while triethanolamine scavenges the holes in the valence band to complete the oxidation reaction. Density Functional Theory (DFT) calculations further reveal that the high-loading Au single atoms provide abundant active sites, optimize the H adsorption and desorption capabilities ($\Delta G_{H^*} =$ 1.8 eV), and thereby further enhance the hydrogen evolution kinetics (Fig. 13d). The catalytic performance of single-atom catalysts (SACs) can be effectively enhanced by appropriately increasing the metal loading, highlighting the critical importance of fabricating SACs with high metal loading densities.

POPs fabricated *via* carbon–carbon coupling reactions exhibit remarkable advantages in photocatalysis, attributed to their exceptional stability, high specific surface area, tunable light absorption properties, and abundant active sites. These materials allow for the flexible construction of D–π–A architectures, which facilitate charge separation and transfer, thereby enabling efficient applications in photocatalytic hydrogen evolution, $H_2O_2$ synthesis, organic functional group transformation, and pollutant degradation. Being free from noble metals or cocatalysts, these materials exhibit excellent cyclic stability and environmental benignity. They not only broaden the scope of photocatalytic materials but also offer a viable pathway for the development of green catalytic processes, which hold great significance for advancing photocatalytic technology from laboratory research to practical applications.

The development of efficient and low-cost catalysts is essential for photocatalysis. However, the intrinsically low photocatalytic efficiency as well as the difficulty in using and recycling photocatalysts in powder morphology greatly limit their practical performance. Gu *et al.* achieved an efficient quasi-homogeneous photocatalytic process by constructing ultrastiff CMP aerogels with exceptional charge-transport properties.[97] These CMP aerogels exhibit an ultra-low density of 0.019–0.085 g $cm^{-3}$, along with a hierarchically porous structure and outstanding charge-transport performance. Applied to the quasi-homogeneous photocatalysis of direct deaminative borylation, the aerogels realize gram-scale productivity and record-high catalytic efficiency under ambient temperature and pressure conditions. Recently, this group designed and synthesized donor–acceptor conjugated microporous polymer aerogels with ultralong-lived excitons.[98] Utilized for the quasi-homogeneous photocatalysis of C–H functionalization, it enables the efficient conversion of 18 types of reactions, exhibiting remarkable conversion efficiency, gram-scale productivity and recyclability. This design principle can be extensively adapted to various photocatalytic systems, offering support for the sustainable synthesis of chemicals and the development of clean energy sources.[99,100]

**3.3.2 Heterogeneous catalysis.** CMPs have carved out a niche in heterogeneous catalysis, thanks to their exceptional stability, highly cross-linked porous architectures, and the ability to incorporate functional groups into their pore structures. These features enable CMPs to immobilize active species, facilitate mass transfer, and serve as stable supports for

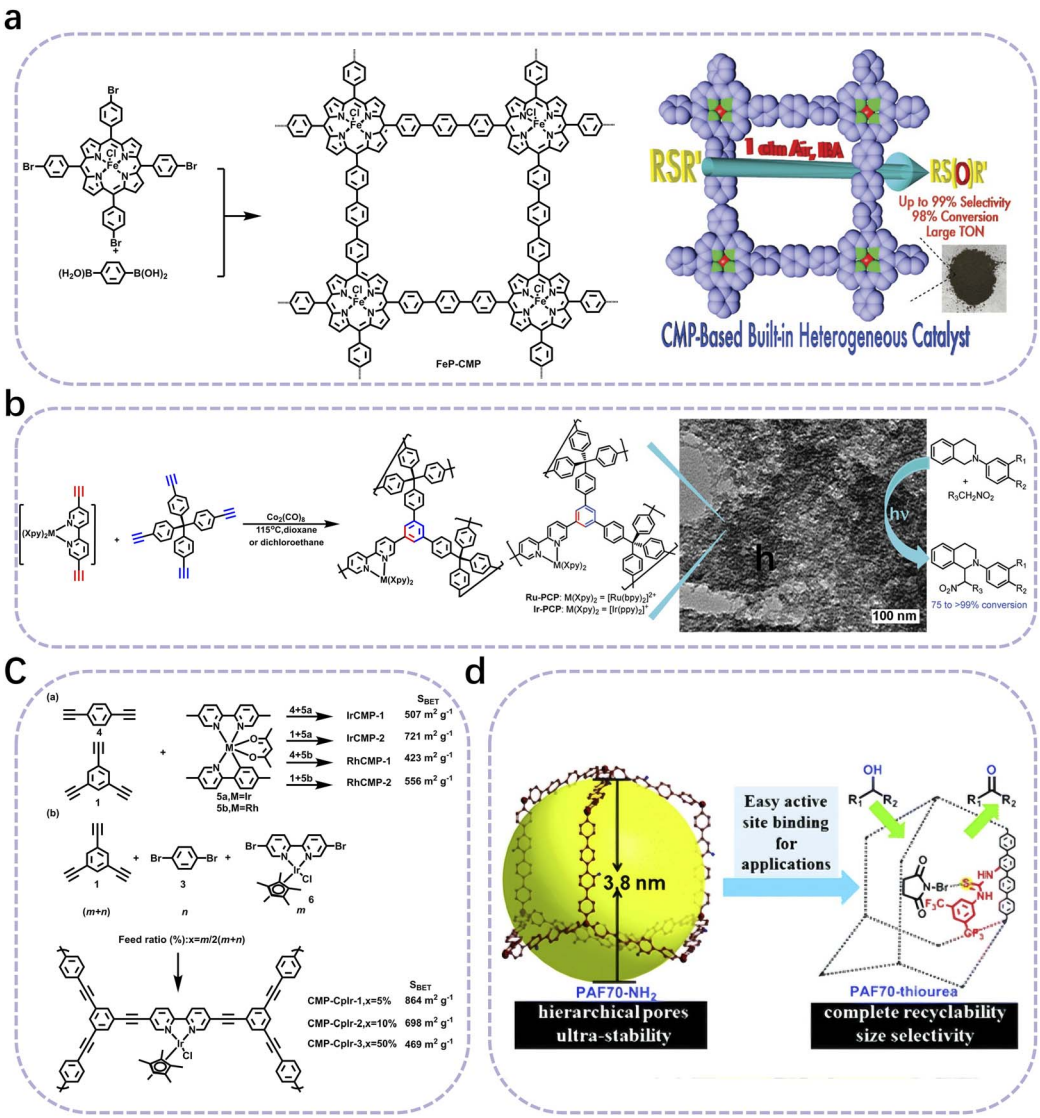


Fig. 14 (a) Schematic representation of the synthesis of nanoporous polymer with metalloporphyrin built-in skeleton and schematic representation of the transformation of sulfides to sulfoxides catalyzed by FeP-CMP.[17] Copyright 2010 American Chemical Society. (b) Synthesis of Ir-PCP and Ru-PCP.[102] Copyright 2011 American Chemical Society. (c) Direct synthetic routes for Ir- and Rh-containing MO-CMPs produced from cyclometalated Ir and Rh complexes, respectively.[104] Copyright 2010 Wiley-VCH GmbH. (d) Synthetic route for PAF70-NH2 and PAF70-thiourea.[8] Copyright 2018 the Royal Society of Chemistry.

catalytic reactions, making them promising alternatives to traditional heterogeneous catalysts.

The utilization of CMPs in heterogeneous catalysis was first demonstrated by Jiang *et al.* in 2010. They successfully synthesized an Fe-porphyrin-based CMP catalyst (FeP-CMP) *via* the Suzuki–Miyaura coupling reaction.[17] This catalyst exhibits outstanding catalytic performance (Fig. 14a). It possesses a specific surface area of 1270 $m^2\ g^{-1}$, featuring both microporous and mesoporous structures with a pore volume of 1.18 $cm^3\ g^{-1}$. The iron porphyrin catalytic sites are covalently embedded in the framework, endowing it with high structural stability and insolubility in common organic solvents. Under ambient temperature and pressure, with molecular oxygen or air as the oxidant, it can efficiently catalyze the oxidation of various sulfides to sulfoxides, achieving a maximum conversion rate of 99% and a selectivity of up to 99%, with a turnover number (TON) as high as 97 320, comparable to those of natural enzymes. This catalyst demonstrates broad substrate compatibility, being applicable to aromatic, aliphatic, and heteroaromatic sulfides. It also exhibits excellent chemoselectivity and cyclic stability, retaining nearly unchanged catalytic activity after 3 consecutive reuse cycles. Additionally, it enables large-scale transformation, making it an environmentally friendly and practical catalytic system. Building on this success, the same team further demonstrated the versatility of FeP-CMP in 2011, showing that it could efficiently catalyze the epoxidation of olefins with excellent recyclability.[101]

Around the same time, other research groups also reported significant progress in CMP-based heterogeneous catalysts. Lin *et al.* synthesized heterogeneous catalysts containing

$[Ru(bpy)_3]^{2+}$ and $[Ir(ppy)_2(bpy)]^+$ through $Co_2(CO)_8$-catalyzed alkyne trimerization (Fig. 14b).[102] Ir-PCP and Ru-PCP are efficient heterogeneous photocatalysts based on porous cross-linked polymers (PCPs), and synthesized by covalently incorporating Ru/Ir phosphorescent units into the framework. Both exhibit excellent stability, with thermal stability up to 350 °C in air, and are insoluble in water, concentrated hydrochloric acid, and various organic solvents. Ir-PCP possesses a BET specific surface area of 1547 $m^2\ g^{-1}$, while Ru-PCP is 1348 $m^2\ g^{-1}$, both featuring micro- and mesoporous structures that enhance substrate contact. They can efficiently catalyze visible light–driven reactions such as Aza–Henry reactions and α-arylation of bromomalonate, achieving conversions exceeding 90%, with catalytic activity comparable to that of homogeneous catalysts. The catalysts can be recovered by filtration, retaining negligible loss of catalytic activity after 4 consecutive reuse cycles, and no metal leaching is detected. They combine molecular tunability with practical applicability. Subsequently, the group synthesized another two metal-pyridine photocatalysts, $Ru(bipy)_3$-CP using alkynes as linking units *via* the Glaser coupling reaction.[103] The catalysts are directly prepared by self-coupling of functionalized monomers, ensuring abundant catalytic sites. Despite its relatively low specific surface area of 198 $m^2\ g^{-1}$, this catalyst maintained high catalytic activity, highlighting the critical role of active site accessibility in PCP/CMP-based catalysts.

Cooper *et al.* also contributed to the development of CMP-based catalysts in 2011. Using triethynylbenzene, 1,4-dibromobenzene, and 5,5′-dibromobipyridine compounds as monomers, they synthesized M-pyridine catalysts *via* the Sonogashira–Hagihara coupling reaction, followed by complexation with Rh salts or Ir salts on a series of MOP supports under Pd(II)/Cu(I) catalysis (Fig. 14c).[104] Metal–organic conjugated microporous polymers (MO-CMPs) are a class of materials prepared *via* two strategies: post-synthetic metalation and direct metal incorporation by copolymerization, enabling the introduction of metal units such as rhenium, iridium, and rhodium. Amorphous in nature and endowed with excellent thermal stability, these MO-CMPs feature tunable metal loading (up to 15 wt%) and a BET specific surface area ranging from 423 to 864 $m^2\ g^{-1}$, while retaining micro and mesoporous structures. The metal sites can exist as pendant groups or as integral linkers without disrupting the conjugation of the polymer backbone. Among these materials, CMP-CpIr-3 exhibits outstanding performance in catalyzing reductive amination reactions, achieving isolated product yields of 86–95% for various ketone and amine substrates, with catalytic activity comparable to that of analogous homogeneous catalysts under mild conditions. Combining conjugated backbones with metal activity, MO-CMPs hold significant potential in heterogeneous catalysis, light harvesting, and other fields, offering a modular synthetic platform for multifunctional porous materials.

Other studies further expanded the application range of CMPs in heterogeneous catalysis. Wang and colleagues synthesized the target catalyst *via* the Sonogashira–Hagihara cross-coupling reaction.[105] This material is an organic nanoporous polymer containing biscovalently bonded Troöger's base as functional moieties. It has a BET specific surface area of 750 $m^2\ g^{-1}$, featuring both microporous (0.6 nm) and mesoporous (1.3 nm) structures with a total pore volume of 0.74 $cm^3\ g^{-1}$. As a heterogeneous catalyst, it can efficiently catalyze the addition reaction of diethylzinc to 4-chlorobenzaldehyde, achieving a maximum yield of 60%, with catalytic activity comparable to that of analogous homogeneous catalysts. The catalyst can be recycled for at least 3 consecutive catalytic cycles with negligible loss of catalytic activity and maintains excellent structural stability, offering a new strategy for the heterogeneous application of Troöger's base-based catalysts. In 2012, the team prepared the catalyst DMAP-CMP *via* coupling copolymerization of catalytically active *N*,*N*-dimethylaminopyridine (DMAP) with triethynylbenzene using the same method.[106] Characterization results indicate that the DMAP loading reaches 2.02 mmol $g^{-1}$. This catalyst can efficiently catalyze the acylation of alcohols and phenols, with no apparent decrease in catalytic activity after 14 consecutive reuse cycles. Notably, the catalyst maintained its activity even after continuous use for 536 hours, demonstrating great potential for industrial-scale applications.

Furthermore, Han *et al.* synthesized two porous conjugated polycarbazoles (CPOP-11 and CPOP-12) *via* carbazole-based oxidative coupling polymerization, with porphyrin and Fe(II)-porphyrin as their respective core structures, and yields reaching 97–98%.[107] CPOP-11 has a BET specific surface area of 1320 $m^2\ g^{-1}$, while CPOP-12 is 1180 $m^2\ g^{-1}$. Both contain micropores of approximately 0.6 nm and mesopores of around 1.3 nm, exhibiting excellent thermal stability. CPOP-12 has a high saturated adsorption capacity for toluene of up to 1192 mg $g^{-1}$, making it suitable for removing harmful aromatic molecules in the environment. CPOP-11 is hydrophobic, with a maximum methanol-to-water adsorption mass ratio of 1 : 39, indicating its ability to efficiently extract methanol from aqueous solutions. CPOP-12 is a high-performance heterogeneous catalyst that can catalyze the oxidation of glycosyl sulfides to glycosyl sulfoxides, achieving a yield of 89% in 5 hours. It exhibits broad substrate compatibility and retains over 80% of its catalytic activity after 3 consecutive reuse cycles. These diverse studies have collectively established CMPs as a versatile class of materials in heterogeneous catalysis, with broad application prospects in organic synthesis and beyond.

Zhu *et al.* synthesized PAF-70-$NH_2$ *via* the Suzuki–Miyaura coupling reaction using boronic acid-containing tetrahedral building units and amine-functionalized 4,4′-dibromobiphenyl (Fig. 14d).[8] PAF70-thiourea is a heterogeneous organocatalyst derived from the ultrastable porous aromatic framework PAF70-$NH_2$, exhibiting excellent intrinsic catalytic performance. It can efficiently catalyze the NBS-mediated oxidation of alcohols to corresponding carbonyl compounds. When 1-phenylethanol is used as the substrate, the conversion rate reaches 79% at 35 °C, and the product yield for small-molecule alcohols is as high as 90%, exhibiting superior catalytic activity to analogous homogeneous thiourea catalysts. The catalyst exhibits significant size selectivity, with drastically reduced catalytic efficiency for large-sized alcohol substrates, confirming that the reaction occurs within the pores. Its cyclic stability is exceptional, retaining no loss of catalytic activity after 36 consecutive reuse cycles, with its

framework structure and porous properties remaining intact, and no leakage of catalytically active components detected, achieving complete recycling and reuse. It provides an efficient and stable solution for heterogeneous organocatalysis. This work exemplifies how the rational design of hierarchical structures in POPs can synergistically optimize catalytic activity and stability, opening up new avenues for catalyst design.

A cascade reaction is a one-pot multi-step reaction conducted in a single reactor, where intermediate products do not require separation. The product of the previous step directly serves as the reactant for the next step, and the target product is obtained after completing multiple transformations in sequence. Sánchez *et al.* synthesized the porous aromatic framework (PPAF) framework *via* Suzuki coupling reaction using 2,2′,7,7′-tetraiodo-9,9′-spirobisfluorene and 1,4-phenylenediboronic acid as monomers.[115] The composite system of PPAF-$SO_3H$ and PPAF-$NH_2$ is a highly efficient heterogeneous acid-base catalyst capable of synergistically catalyzing one-pot two-step cascade reactions. The acidic PPAF-$SO_3H$ first catalyzes the hydrolysis of benzaldehyde dimethyl acetal to form benzaldehyde, and the basic PPAF-$NH_2$ then catalyzes the Knoevenagel condensation between benzaldehyde and malononitrile. The final product, benzylidenemalononitrile, achieves a conversion rate of 100%, and its activity is far superior to that of traditional ion exchange resin composite systems. In this system, the acidic and basic sites do not neutralize each other and can function independently, with a tunable acid-base ratio. The catalysts can be recovered by simple filtration, retaining high catalytic activity and selectivity after 7 consecutive reuse cycles, with no leaching of active components detected, offering a green and efficient strategy for multi-step organic reactions requiring acid-base synergy.

In conclusion, POPs constructed *via* carbon–carbon coupling reactions have shown remarkable potential in diverse catalytic applications, including photocatalysis, heterogeneous catalysis, and cascade catalysis. These materials provide innovative solutions for energy conversion and environmental remediation. Future research should focus on further elucidating the structure–activity relationships of POPs, optimizing their catalytic performance, and extending their applications to a wider range of catalytic processes. By doing so, POPs are expected to play an increasingly pivotal role in addressing global energy and environmental challenges, thereby advancing the development of sustainable catalytic technologies.

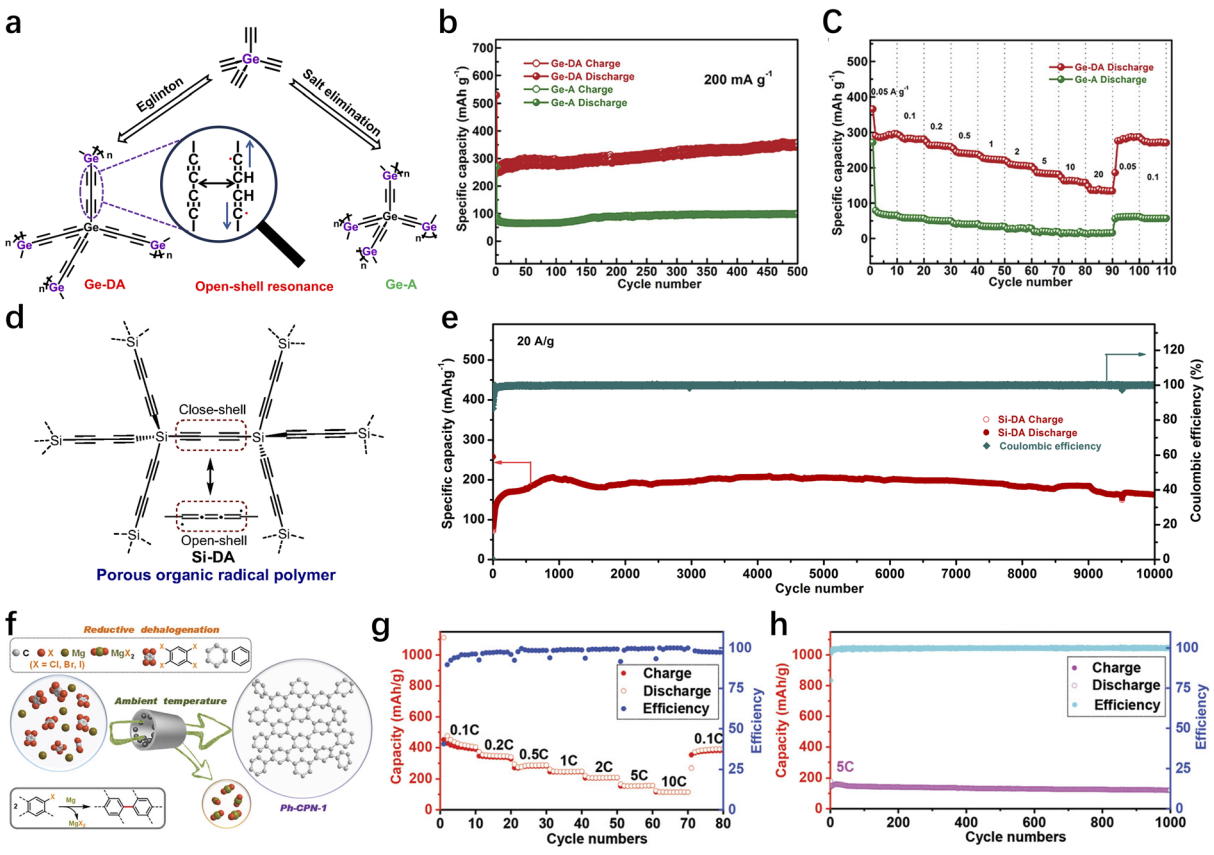


Fig. 15 (a) Synthesis and structural diagram of porous organic polymers Ge-DA and Ge-A. (b) Comparison of cycling performance of Ge-DA and Ge-A at 200 mA $g^{-1}$. (c) Rate behavior of Ge-DA and Ge-A at various current densities.[18] Copyright 2024 Wiley-VCH GmbH. (d) Synthesis of porous organic polymers Si-DA. (e) Cycling performance of Si-DA at 20 A $g^{-1}$.[116] Copyright 2023 Chinese Chemical Society. (f) The reductive dehalogenation approach for the construction of CPNs *via* direct C–C bond formation between aromatic rings. (g) Charge–discharge capacities of the LIB half-cells at different current densities (0.1–10C). (h) Cycle performance of Ph-CPN-1-based LIB half-cell with the current density of 5C.[117] Copyright 2021 Wiley-VCH GmbH.

### 3.4 Electrochemistry

POPs, as a class of covalently linked porous materials, exhibit tremendous potential in the electrochemical field due to their structural designability, high specific surface area, and excellent chemical stability. Among them, POPs fabricated *via* C–C coupling reactions can precisely tune the skeletal conjugation degree, pore size, and functional sites, offering innovative solutions to key challenges in electrochemical energy storage, including low ion transportation efficiency, insufficient active sites for catalytic reactions, and poor electrolyte stability. These materials boast diverse synthetic routes.[108–114] For instance, Eglinton coupling can construct alkynyl-conjugated networks; Ullmann-type reductive coupling enables the direct linkage of aromatic rings at room temperature; Yamamoto coupling excels at preparing rigid aromatic frameworks; and Sonogashira coupling facilitates the introduction of alkynyl-aryl composite structures. These synthetic strategies can tailor the electronic properties and porous structures of materials to suit different application scenarios. The pore size can be precisely adjusted from micropores to mesopores by modifying the monomer structure, or active sites (*e.g.*, free radicals and cations) can be introduced to enhance electrochemical responses. Thus, they have emerged as a research hotspot in the electrochemical field.

**3.4.1 Battery anode materials.** The Eglinton coupling reaction constructs conjugated networks *via* the homopolymerization of alkynyl groups, rendering it particularly suitable for fabricating POPs with three-dimensional structures and open-shell radical features, which provide abundant active sites and efficient transport channels for ion storage. Zhu *et al.* synthesized a three-dimensional germanium-based porous organic polymer (Ge-DA) with an open-shell resonance structure using tetraethynylgermanium as the monomer *via* the Eglinton coupling reaction (Fig. 15a).[18] This material has a high specific surface area of 368.8 $m^2\ g^{-1}$ and a hierarchical pore structure with major pore sizes of 1.98 nm and 4.22 nm. It not only offers sufficient active sites for sodium ion storage but also significantly shortens the ion diffusion pathway, thereby effectively improving ion transport efficiency. DFT calculations show that it has a relatively low LUMO energy level (−5.46 eV) and a narrow band gap (approximately 1.64 eV), which can effectively enhance electron conduction efficiency. In sodium-ion batteries (SIBs), Ge-DA exhibits excellent performance. It delivers a specific discharge capacity of 349 mAh $g^{-1}$ at a current density of 200 mA $g^{-1}$ and retains 135 mAh $g^{-1}$ (Fig. 15b) even at a high current density of 20 A $g^{-1}$, demonstrating excellent rate performance (Fig. 15c). It exhibits exceptional cycling stability with 5000 consecutive cycles at 5 A $g^{-1}$, retaining a capacity of 112 mAh $g^{-1}$ and a nearly 100% coulombic efficiency. The material exhibits good electrical conductivity with a charge transfer resistance of only 55 Ω, and $Na^+$ storage is dominated by capacitive mechanism. The electrochemical process exhibits excellent reversibility: the EPR signal of radicals diminishes during discharge and is fully recovered after charging. Its overall electrochemical performance is far superior to that of the monoalkynyl analog (Ge-A), fully highlighting the significant advantages of Ge-DA in sodium-ion storage.

Similarly, Zhu *et al.* synthesized a three-dimensional silicon-diacetylene porous organic radical polymer (Si-DA) using tetraethynylsilane as the monomer *via* the Eglinton coupling reaction (Fig. 15d).[116] Its carbon-centered radical features, LUMO energy level of −5.47 eV, and narrow band gap of 1.46 eV can enhance conductivity. The binding energy between radical sites and lithium ions (−6.13 eV) is lower than that of non-radical counterparts (−2.97 eV), enabling rapid provision of lithium-ion binding sites. Meanwhile, its specific surface area of 779 $m^2\ g^{-1}$ and microporous structure provide channels for ion transport. As an anode material for lithium-ion batteries (LIBs), the three-dimensional silicon-based diacetylene porous organic radical polymer (Si-DA) exhibits excellent cycling stability and rate performance, demonstrating great application potential in the energy field. At a current density of 50 mA $g^{-1}$, the initial discharge capacity of Si-DA reaches 1308 mAh $g^{-1}$, and after 60 cycles of activation, the capacity increases to 946 mAh $g^{-1}$ with a coulombic efficiency of 99.2%; at a current density of 200 mA $g^{-1}$, it achieves a saturated capacity of 1161 mAh $g^{-1}$, which is significantly higher than those of control samples silicon-based phenylene diacetylene porous organic polymer (Si-PDA) and silicon-based biphenyl porous organic polymer (Si-BP). At an ultra-high current density of 20 A $g^{-1}$, it still maintains a capacity of 200 mAh $g^{-1}$ after 10 000 cycles with a coulombic efficiency as high as 99.6% (Fig. 15e). Under different current densities ranging from 50 mA $g^{-1}$ to 20 A $g^{-1}$, the reversible capacity is significantly higher than those of Si-PDA and Si-BP. The open-shell radical structure derived from conjugated diacetylene endows it with a lower lithium-ion binding energy, which serves as the key mechanism underlying its outstanding electrochemical performance.

Dai *et al.* reported a method for preparing CPNs *via* mechanochemical Ullmann-type homocoupling reactions, which directly links aromatic rings.[117] In the presence of magnesium, aromatic halides undergo dehalogenation at room temperature to form Grignard reagent intermediates, which then participate in the subsequent C–C coupling. Using 1,2,4,5-tetrabromobenzene (TBB) as the monomer, they achieved C–C coupling of aromatic rings, successfully synthesizing a series of CPNs (Fig. 15f). Ph-CPN-1 possesses ordered mesoporous structures with pore sizes ranging from 8.5 to 10 nm, which can shorten the lithium-ion diffusion distance and enhance ion transport kinetics. Meanwhile, its conjugated skeleton effectively facilitates electron conduction, achieving the synergistic optimization of ion and electron transport.

As anode materials for lithium-ion batteries, conjugated porous networks (CPNs) represented by Ph-CPN-1 exhibit excellent electrochemical performance. At 0.1C, it delivers an initial discharge capacity of 1112 mAh $g^{-1}$ and a charge capacity of 455 mAh $g^{-1}$, with the stabilized capacity far exceeding the theoretical capacity of graphite. It also demonstrates outstanding rate performance, providing capacities of 338, 283, 245, 206, 154, and 115 mAh $g^{-1}$ at current densities ranging from 0.2C to 10C, which is attributed to its porous structure that shortens the lithium-ion diffusion distance (Fig. 15g). The cycling stability is excellent: after 500 cycles at 2C and 1000 cycles at 5C, the coulombic efficiency remains above 99.7%

(Fig. 15h). Featuring a low-potential lithium intercalation plateau, the material exhibits good reversibility of redox reactions, with the coulombic efficiency quickly rising above 96% after the first cycle. Integrating high capacity, rapid transport rate, and long cycle life, it serves as an excellent energy storage electrode material. Compared with natural graphite and traditional polymer materials, Ph-CPN-1 shows obvious advantages in capacity, rate performance, and cycling stability, making it a promising candidate for next-generation high-performance lithium-ion battery anode materials.

**3.4.2 Solid polymer electrolytes.** Solid polymer electrolytes (SPEs) can not only mitigate the battery safety hazards, inhibit the growth of dendrites, and boost battery energy density, but also exhibit advantages including good flexibility, excellent viscoelasticity, and favorable swelling properties. Therefore, they hold broad application prospects in the next generation of high-safety solid-state batteries.

In the field of electrolytes, Su *et al.* successfully synthesized PAF-142 *via* Yamamoto-type Ullmann cross-coupling, using imidazolium cation-containing building blocks (*e.g.*, $TBIBr_3$) and 1,4-diethynylbenzene as monomers.[19] After introducing $TFSI^-$ *via* ion exchange, the composite electrolyte formed by blending PAF-142-$TFSI^-$ with PVDF-HFP exhibits enhanced lithium-ion conductivity; this improvement stems from the strong electrostatic interactions between imidazolium cations in PAF-142 and $TFSI^-$, which facilitate $Li^+$ dissociation (Fig. 16a). At 20 °C, the lithium-ion conductivity of this composite electrolyte reaches $8.77 \times 10^{-4}$ S $cm^{-1}$, with a high lithium-ion transference number ($t_{Li^+}$) of 0.95. Meanwhile, PAF-142 forms a stable interface with the lithium anode, generating a solid electrolyte interphase (SEI) layer rich in inorganic components (*e.g.*, LiF and $Li_3N$) at the interface (Fig. 16b). This stable interface structure effectively inhibits lithium dendrite growth, enabling Li//Li symmetric batteries to operate stably for

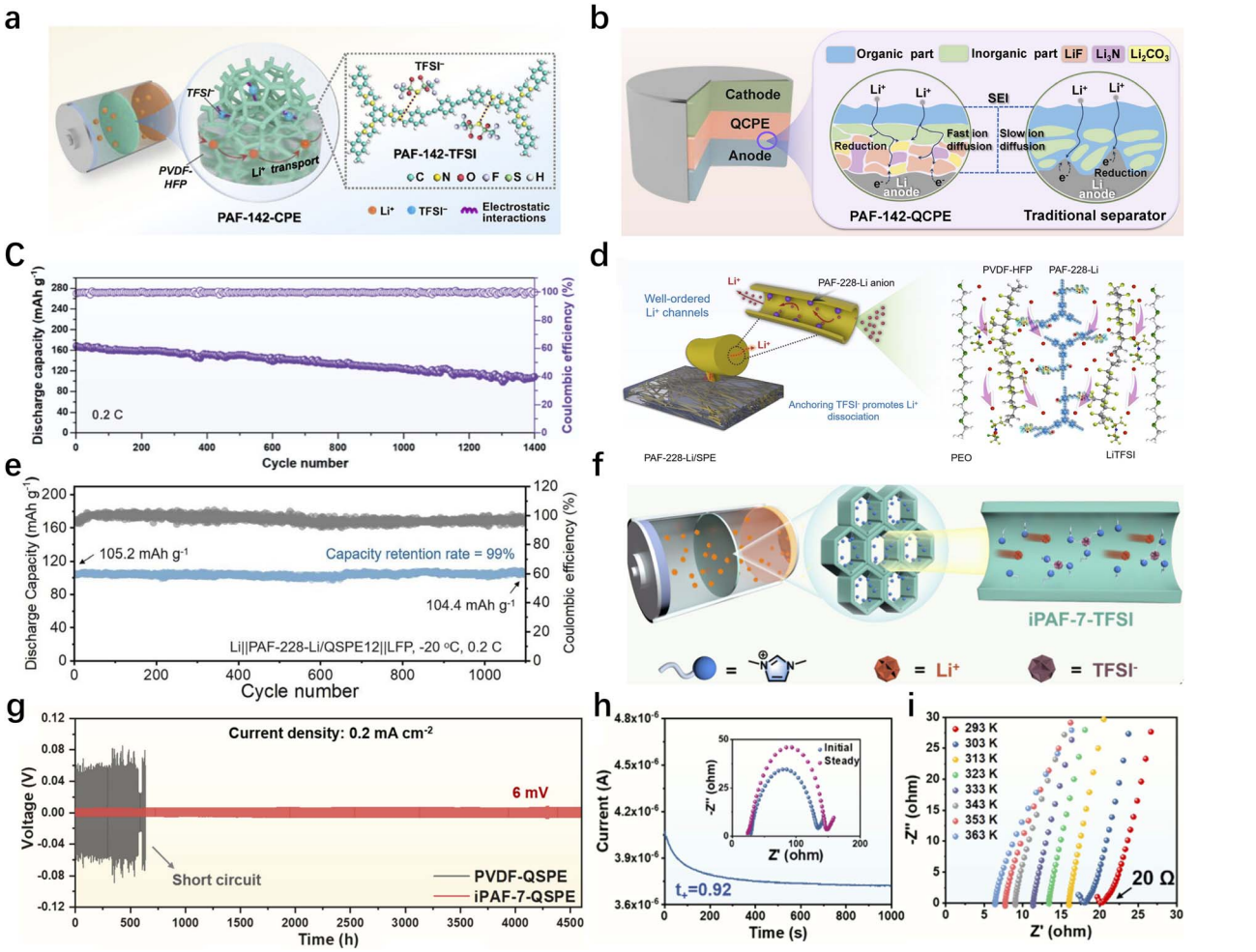


Fig. 16 (a) The structure of PAF-142-CPE. (b) Schematic diagram of lithium anode interface in traditional separator and PAF-142-QCPE. (c) Cycle performance and Coulomb efficiency of Li//PAF-142-QCPE//LFP cells at 0.2C.[19] Copyright 2025 Wiley-VCH GmbH. (d) Lithium-rich PAF-228-Li enabled dual $Li^+$ transport *via* porous channels and surface sites, and its uniform dispersion in PVDF-HFP formed continuous 3D ionic bridges. (e) Cycling performance of Li//PAF-228-Li/QSPE//LFP at 0.2C, −20 °C.[118] Copyright 2025 Elsevier B.V. (f) Schematic illustration of the interaction between iPAF-7 and LiTFSI. (g) Voltage profile of galvanostatic lithium plating/stripping of the symmetric Li//iPAF-7-QSPE//Li cells at a current density of 0.2 mA $cm^{-2}$. (h) CA curves of iPAF-7-QSPE. (i) EIS of stainless steel (SS) symmetrical cells with iPAF-7-QSPE from 20 to 90 °C.[119] Copyright 2024 American Chemical Society.

8500 cycles at a specific current density. In the Li//LFP battery system, the battery retains 63% of its initial capacity after 1400 cycles (Fig. 16c). The superior performance of PAF-142-based composite polymer electrolytes in enhancing lithium-ion conductivity, inhibiting lithium dendrite growth, and ensuring battery cycling stability provides an innovative solution for the development of high-performance lithium-ion battery electrolytes. It is expected to promote lithium-ion batteries to achieve new breakthroughs in key performance indicators such as energy density, safety, and cycle life.

The Sonogashira coupling reaction can efficiently construct conjugated frameworks containing alkynyl and aryl groups. By incorporating functional units such as lithium salts and acid-base responsive groups, it can be tailored for extreme scenarios (*e.g.*, low-temperature environments) and intelligent response applications. Zhu *et al.* synthesized PAF-228 *via* the Sonogashira coupling reaction using 2,5-dibromohydroquinone and 1,3,5-tris(4-ethynylphenyl)benzene as monomers.[118] After lithiation, it was converted into a single-ion conductor (PAF-228-Li), which was electrospun with PVDF-HFP into nanofibers, followed by infusing PEO/LiTFSI to form a SPE (Fig. 16d). This hierarchical design synergistically integrates the mechanical integrity and electrochemical stability of PVDF-HFP with the three-dimensional lithium-ion nanochannels of PAF-228-Li, while PEO/LiTFSI acts as an interfacial bridge to enable ultrafast $Li^+$ transport. The key advantage lies in the nanofiber matrix disrupting the crystallinity of PEO (the crystallinity of traditional SPEs typically limits their conductivity to $10^{-7}$ S cm$^{-1}$ and a narrow voltage window), thereby enabling excellent room-temperature electrochemical performance. The PAF-228-Li/PVDF-HFP electrolyte exhibits an ionic conductivity of $5.48 \times 10^{-4}$ S cm$^{-1}$, an electrochemical stability window of 4.85 V, and a high lithium-ion transference number ($t_{Li^+}$) of 0.76. Even at −20 °C, this SPE maintains a conductivity of $3.4 \times 10^{-4}$ S cm$^{-1}$ and can form a self-stabilizing LiF/$Li_3N$ interfacial phase, effectively inhibiting lithium dendrite growth. When applied in Li//PAF-228-Li/SPE12//$LiFePO_4$ batteries, it delivers an initial capacity of 100.5 mAh g$^{-1}$ at −20 °C (0.2C), with a capacity retention rate as high as 99.5% after 580 cycles, setting a new benchmark for low-temperature solid-state batteries (Fig. 16e).

Recently, Su *et al.* synthesized iPAF-7 *via* the Sonogashira cross-coupling reaction, using 1,3,5-triethynylbenzene and a bromide-functionalized imidazole derivative (iDBB) as monomers.[119] iPAF-7 is subjected to ion exchange with LiTFSI to obtain iPAF-7-TFSI, which is then blended with poly(vinylidene fluoride-*co*-hexafluoropropylene) (PVDF-HFP) to fabricate iPAF-7-SPE (Fig. 16f). After infiltrating iPAF-7-SPE with a small amount of plasticizer, a quasi-solid polymer electrolyte (iPAF-7-QSPE) was obtained. iPAF-7-QSPE possesses a dense structure and exceptional electrochemical stability, with an ionic conductivity as high as $7.92 \times 10^{-4}$ S cm$^{-1}$ (Fig. 16i) and a lithium-ion transference number of up to 0.92 (Fig. 16h). The Li//iPAF-7-QSPE//Li symmetric cell can operate stably for 4500 hours at a current density of 0.2 mA cm$^{-2}$, exhibiting excellent long-cycle performance, with a polarization voltage maintained at around 6 mV, which can effectively inhibit the growth of lithium dendrites (Fig. 16g). In addition, the LFP//iPAF-7-QSPE//Li battery delivers a discharge capacity of 167 mAh g$^{-1}$ at a current density of 0.2C, with a capacity retention rate of 89% after 600 cycles and a coulombic efficiency as high as 100%. This work presents an effective strategy for constructing anion acceptors based on ionic PAFs, providing valuable insights for the advancement of high-performance LIBs.

**3.4.3 Battery cathode materials.** As a class of porous materials with tunable topologies and ultrahigh specific surface areas, PAFs have emerged as promising iodine hosts for advanced zinc-iodine batteries, with PAF-1 standing out for its exceptional performance in suppressing the polyiodide shuttle effect and boosting battery cyclability.[120] PAF-1 possesses an ultrahigh specific surface area of 5600 m$^2$ g$^{-1}$, providing abundant sites for iodine loading, with an iodine loading capacity of up to 63 wt%. In zinc-iodine batteries, the shuttle effect of polyiodides is one of the key factors causing battery performance degradation. PAF-1 can effectively confine polyiodides within the electrode material through strong interactions between its benzene rings and polyiodides, significantly inhibiting the shuttle effect (Fig. 17a and b). In practical battery performance tests, PAF-1 exhibits outstanding performance: at a current density of 0.5C, its specific capacity reaches 328 mAh g$^{-1}$; when the current density is increased to 10C, the capacity retention rate remains 86% after 20 000 cycles (Fig. 17c and d). This phenomenally high capacity of $I_2$ @PAF-1 can be mainly attributed to the structural advantages of PAF-1. First, the large specific area of PAF-1 leads to significantly higher electrical double-layer capacitance (EDLC). Second, the evenly distributed micropores and confinement of polyiodides enhance the utilization of electrochemically active materials, resulting in maximized or even full release of the theoretical capacity of $I^-/I_2$. Compared with traditional carbon materials as iodine hosts, PAF-1 effectively solves the problem of rapid capacity decay caused by polyiodide dissolution, significantly improving the ultra-stable cyclability (Fig. 17e) and high energy power densities (Fig. 17f), thus providing a new material option for developing high-performance, long-life zinc-iodine batteries.

However, despite the series of remarkable research advances achieved to date,[121–126] the field still presents numerous challenges alongside opportunities. In future research, it is essential to further deepen the understanding of the mechanism underlying C–C coupling reactions. Through the precise design of novel monomers and the optimization of coupling pathways, more accurate regulation of the structure and performance of POPs can be achieved to further enhance the conductivity, materials stability, and utilization efficiency of active sites. More monomers with special electronic structures and geometric shapes can be explored. Through rational molecular design and optimization of reaction conditions, POPs with more ideal pore structures, electron transport pathways, and active sites can be fabricated. On the other hand, it is crucial to strengthen the close integration of basic research with practical applications, and accelerate the transformation of POPs materials based on C–C coupling reactions from laboratory research to industrial production and practical applications. In the field of high-energy-density batteries, efforts should be made to

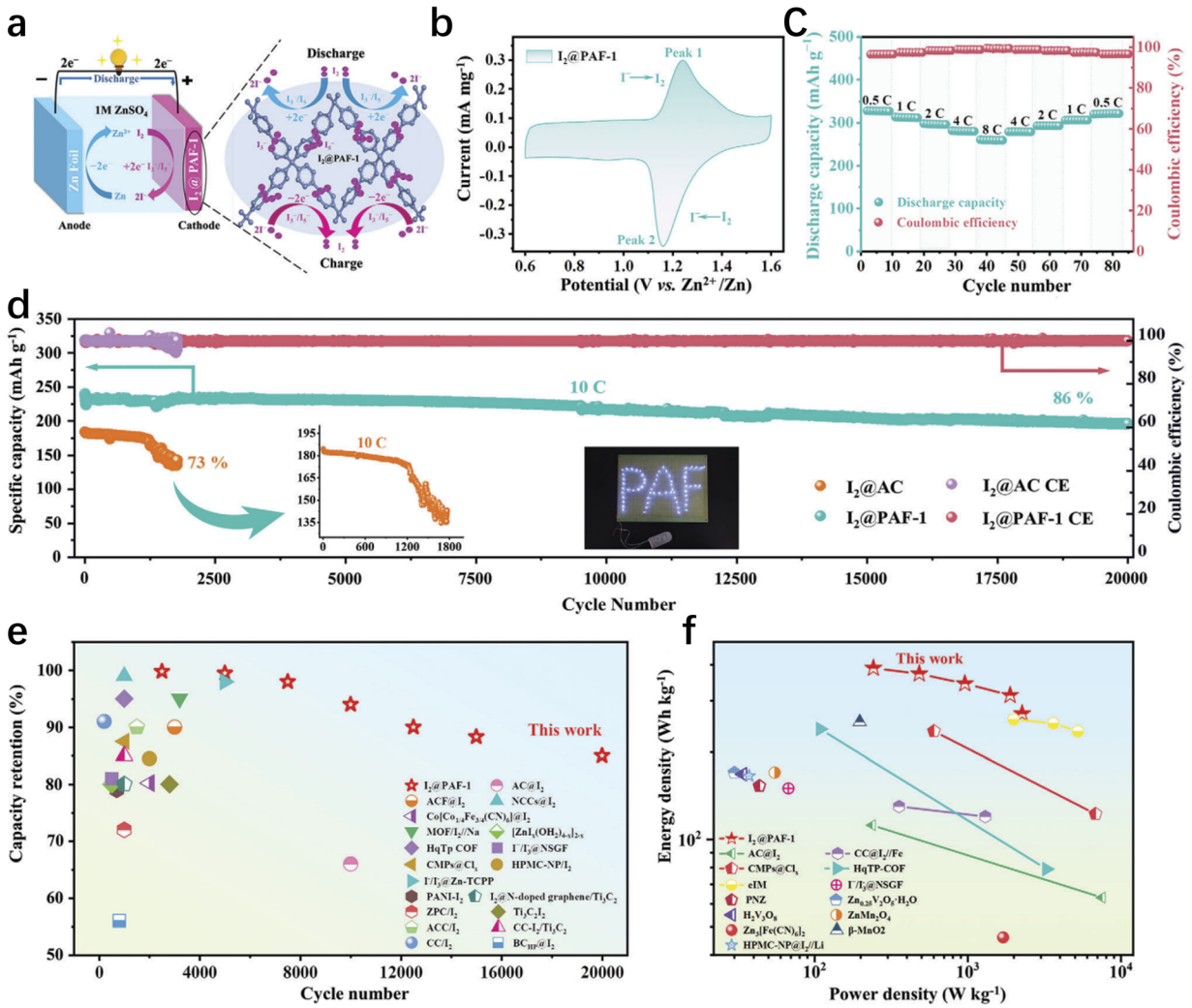


Fig. 17 (a) Schematic illustration of the configuration and storage mechanism of Zn–$I_2$@PAF-1 battery. (b) CV curve at a scan rate of 0.1 mV $s^{-1}$. (c) Rate performance (blue) and CE (red) of Zn–$I_2$@PAF-1 battery at 0.5–8 C. (d) Long-term cyclability of Zn–$I_2$@AC battery (orange), Zn–$I_2$@PAF-1 battery (blue), and the corresponding CEs at 10C. The inset is a paragraph of blue light-emitting diode powered by Zn–$I_2$@PAF-1 batteries. (e) Cyclability comparison of this study with recently reported metal (Li, Na, and Zn)–$I_2$ battery systems. (f) Ragone plots of recently reported AZIB systems and this study.[120] Copyright 2024 Wiley-VCH GmbH.

develop high-performance electrode materials and electrolyte systems that can meet the requirements of application scenarios such as electric vehicles and large-scale energy storage. In the field of high-efficiency catalysis, the application potential of POPs materials in critical reactions (*e.g.*, electrocatalytic carbon dioxide reduction and water splitting for hydrogen evolution) should be further explored, so as to provide practical technical solutions for addressing global challenges such as energy crisis and environmental pollution.

In addition, attention should also be paid to the sustainability and cost-effectiveness of these materials.[127–130] On the premise of guaranteeing material performance, efforts should be devoted to exploring greener and more economical synthetic routes and raw materials, so as to realize the coordinated development of materials science, environmental protection, and economic growth. Through continuous innovative research and interdisciplinary collaboration, more breakthroughs are expected in C–C coupling-derived POPs and their electrochemical applications, thereby injecting new vitality into the advancement of electrochemical technology and the development of related industries.

In electrochemical applications, the structure–performance relationship of POPs synthesized *via* carbon–carbon coupling reactions arises from the synergistic regulation of molecular design, porous properties, and electronic structure. From the perspective of molecular construction, we can adjust monomer types and linkage modes through different carbon–carbon coupling reactions. Such adjustments enable precise customization of the conjugation degree, functional site density, and flexibility of POP backbones. For example, germanium-based/silicon-based POPs fabricated *via* Eglinton coupling possess open-shell radical structures derived from conjugated diacetylene and narrow band gaps (1.46–1.64 eV), which reduce ion binding energy ($Li^+$ binding energy as low as −6.13 eV).

Combined with their specific surface areas of 368.8–779 $m^2 g^{-1}$ and hierarchical porous structures, they not only shorten ion diffusion paths but also enhance electron conduction efficiency. When used as anodes for sodium-ion/lithium-ion batteries, they can maintain a stable capacity of 112–200 mAh $g^{-1}$ even at a high current density of 20 A $g^{-1}$, with no obvious attenuation after 5000–10 000 cycles. In electrolyte systems, PAF-142 prepared *via* Yamamoto-type Ullmann coupling is functionalized with imidazolium cations, forming strong electrostatic interactions with $TFSI^-$ to promote $Li^+$ dissociation. Its stable porous framework forms a SEI layer rich in $LiF/Li_3N$ with the lithium anode, enabling the composite electrolyte to achieve an ionic conductivity of $8.77 \times 10^{-4}$ S $cm^{-1}$ and a lithium-ion transference number of 0.95, supporting stable cycling of symmetric batteries for 8500 cycles. The synergy between its three-dimensional lithium-ion nanochannels and PVDF-HFP nanofiber matrix disrupts PEO crystallinity, maintaining a conductivity of $3.4 \times 10^{-4}$ S $cm^{-1}$ even at −20 °C and enabling a battery capacity retention rate of 99.5% after 580 cycles. For cathode materials, PAF-1, with an ultrahigh specific surface area of 5600 $m^2 g^{-1}$ and uniform microporous structure, inhibits the shuttle effect through strong interactions between benzene rings and polyiodides, allowing zinc-iodine batteries to retain 86% of their capacity after 20 000 cycles at 10C. In summary, the electrochemical properties of POPs (conductivity, ion transport efficiency, cycling stability, storage capacity, *etc.*) are directly related to the structural characteristics mediated by carbon–carbon coupling reactions. Through precise regulation of monomer structure, coupling mode, functional modification, and porous parameters, directional matching between structure and electrochemical performance can be achieved.

# 4 Summary and outlooks

As elaborated above, a diverse range of POPs with exceptional performance have been successfully fabricated *via* five types of carbon–carbon coupling reactions, including $C(sp^2)$–C(sp) coupling, $C(sp^2)$–$C(sp^2)$ coupling, C(sp)–C(sp) coupling, $C(sp^2)$–$C(sp^3)$ coupling, and $C(sp^3)$–$C(sp^3)$ coupling. These materials can maintain their chemical structure even under harsh conditions, thus exhibiting broad application prospects in various fields such as gas adsorption, gas separation, catalysis, and electrochemistry. Furthermore, POPs developed *via* carbon–carbon coupling reactions have greatly promoted the development of materials science. Through diverse carbon–carbon coupling reactions, POPs with tailored structures and properties can be precisely synthesized to meet a wide range of application requirements. However, current research in this field still faces numerous key challenges, mainly focusing on four aspects: optimization of synthesis methods, greening of catalytic systems, precise structural regulation and defect management, and improvement of application performance alongside the expansion of new application fields.

In terms of the optimization of synthesis methods, there are still many urgent problems to be solved in the construction of POPs *via* C–C coupling reactions, among which the bottleneck of $C(sp^3)$–$C(sp^3)$ coupling reaction is the most prominent, mainly manifested in low reaction activity, frequent side reactions, and insufficient catalyst universality. These problems directly restrict the efficient preparation of POPs materials with complex structures and diverse functions. Although $Ni(COD)_2$ catalyst has been successfully applied in the $C(sp^3)$–$C(sp^3)$ coupling reaction for constructing POPs, achieving an initial breakthrough in this field, the reaction still has key problems such as harsh reaction conditions and incompletely clarified reaction mechanism, which require further in-depth research and optimization.

In terms of catalyst performance, the currently developed catalyst systems often have high catalytic activity only for specific substrates, with poor universality, making it difficult to adapt to monomers with complex structures; at the same time, catalysts are prone to deactivation during the reaction, leading to a significant decrease in reaction yield, which further limits the practicality of the reaction. Therefore, the development of catalysts with higher activity and selectivity, especially nickel-based or other non-noble metal catalysts for $C(sp^3)$–$C(sp^3)$ coupling reactions, has become one of the core research directions in this field. Specifically, the stability of the catalyst can be improved and the activation energy can be reduced by in-depth study of the Ni(0)/Ni(II) catalytic cycle mechanism and optimization of ligand design. Meanwhile, it is necessary to break through the limitations of traditional coupling reactions. In addition to the common Ullmann coupling and Yamamoto coupling, we should actively explore milder C–C coupling reaction types such as photocatalytic coupling and electrochemical coupling to achieve milder reaction conditions and broader substrate applicability. In addition, traditional POPs are mostly constructed based on rigid covalent bonds, and the introduction of flexible or rotatable chemical bonds/linking groups has become a highly promising emerging research direction. This method can not only maintain the structural rigidity of the material but also endow it with new functions (such as $CO_2$ capture capacity), which requires researchers to accurately balance the adjustability brought by flexible structures and the rigidity required by the material when designing synthesis routes, so as to achieve the synergistic optimization of structure and function.

The greening of catalytic systems is another important research direction. At present, a large number of coupling reactions (such as Pd(0)-catalyzed Sonogashira–Hagihara coupling reaction and Suzuki–Miyaura coupling reaction) rely on metal catalysts. This dependence often leads to practical problems such as increased difficulty in product purification, environmental pollution, and high catalyst recovery costs, which are contrary to the current concepts of green chemistry and sustainable development. Therefore, the development of environmentally friendly and sustainable metal-free or low-toxic catalytic systems with high catalytic activity and stability has become an urgent challenge. Currently, the construction of green catalytic systems still faces two core bottlenecks. First, the application limitation of green solvents. In environmentally friendly solvents such as water, supercritical $CO_2$, ionic liquids, or biomass-derived solvents, the solubility, reaction rate, and selectivity of substrates in C–C coupling reactions are often

affected to varying degrees, which need to be solved by optimizing reaction parameters and designing adaptive catalysts. Second, the performance shortage of non-noble metal catalysts. Compared with noble metal catalysts, cheap and easily available transition metal catalysts such as nickel, copper, and iron still have a large gap in catalytic efficiency and stability, which need to be compensated by means of ligand design and skeleton engineering. In response to the above bottlenecks, the optimization of solvent systems, the development of non-noble metal catalysts, and the application of immobilized catalysts have become important breakthroughs in the construction of green catalytic systems. In terms of solvent optimization, priority should be given to environmentally friendly solvents. For example, some Ullmann-type coupling reactions have been attempted in biomass-derived solvents, which effectively improved the sustainability of the reaction. In terms of the development of non-noble metal catalysts, nickel catalysts have become a current research focus due to their rich oxidation state chemistry and low cost, and their catalytic performance needs further optimization in the future. Furthermore, immobilizing catalysts on POPs or other suitable carriers can realize efficient recovery and recycling of catalysts, significantly reduce waste generation, and lower reaction costs.

Precise structural regulation and defect management play a decisive role in the performance of POPs. The structural characteristics of POPs, such as pore size, pore volume, specific surface area, and porosity, directly determine their performance in various application scenarios, while defects and disorders are common during the synthesis and subsequent use of POPs. Therefore, achieving precise structural regulation and effective defect management of POPs is the key to improving material performance and expanding their application scenarios. However, the synthesis of POPs is a complex multi-step and multi-variable process, and it is still a great challenge to precisely control their structure from the molecular scale to the macro scale (including key parameters such as pore size, pore connectivity, and crystallinity). At the same time, the generation of defects during polymerization is difficult to completely avoid. How to minimize harmful defects and rationally utilize beneficial defects to further optimize material performance is still an urgent problem to be solved. In response to the above problems, it can be promoted through three core research paths. First, skeleton engineering and monomer design. By designing organic monomers with specific connection points and conformations, the bonding mode and spatial structure of polymers can be precisely controlled, thereby achieving precise regulation of pore size distribution and porosity. Second, post-synthesis modification and functionalization. After the formation of the POPs skeleton, the surface chemical properties and pore environment can be further regulated by introducing specific functional groups such as hydroxyl groups, so as to enhance the adsorption or catalytic performance of the material for specific molecules. Third, defect characterization and regulation. Advanced characterization technologies such as high-resolution transmission electron microscopy and synchrotron radiation X-ray diffraction can be developed to deeply explore the types, distribution rules of defects in POPs and their impact on material performance, and then explore effective methods for defect control, providing theoretical support for material performance optimization. However, how to precisely design and synthesize POPs nanoparticles with specific properties to adapt to complex application scenarios remains a major challenge to be overcome.

At the application level, the core challenges faced by POPs focus on the improvement of performance and the optimization of long-term stability. With the advantages of adjustable porosity, low density, high specific surface area, diverse composition, easy post-functionalization, high carbon content, and excellent chemical and thermal stability, POPs have shown great potential in fields such as gas adsorption and separation, photocatalysis, electrochemistry, and energy storage. However, limited by their own performance shortcomings, their large-scale application is still severely restricted, and the main problems are concentrated in poor conductivity, insufficient selectivity and efficiency, difficulty in large-scale production, and lack of long-term stability. Therefore, balancing conductivity and porosity, developing large-scale synthesis routes, and exploring new application scenarios have become the key directions of future POPs application research. Specifically, relying on precise pore size regulation capabilities, POPs have unique advantages in gas separation fields such as $CO_2/N_2$ and $C_2H_6/C_2H_4$, but further breakthroughs in molecular engineering design and preparation technology are still needed to promote their practical application. In addition, the improvement of conductivity is the core demand for expanding the application of POPs in electronic and electrochemical fields. Most POPs materials have poor conductivity, which is the core factor limiting their application. The conductivity of POPs can be improved by introducing conductive skeleton units, or doping conductive materials, but attention should be paid to balancing the relationship between conductivity and the inherent high porosity and high specific surface area of the material. In the field of catalysis, it is necessary to improve the conversion rate and selectivity of catalytic reactions through structural optimization and functional modification. The expansion of new application fields provides a broad space for POPs research. At present, relying on their good biocompatibility and functionalization characteristics, POPs have broad application potential in biomedical fields such as drug delivery and biosensing. But the current key issues such as their biosafety, *in vivo* stability, and targeting still need further research to lay the foundation for their practical application in biomedical fields. In wastewater treatment, POPs, as new adsorbent materials, show excellent performance in removing heavy metal pollutants. In the field of visible light catalysis, POPs, as efficient metal-free photocatalysts, play an important role in organic synthesis, pollutant degradation, and water splitting reactions. At the same time, laboratory-scale POPs synthesis methods are often costly and difficult to achieve industrial production. Developing economically efficient and scalable synthesis routes is the key to the commercial application of POPs. In practical applications, the long-term stability and regeneration performance of POPs materials directly affect

their economic benefits and environmental friendliness, which also need to be focused on and optimized.

In summary, the research on constructing POPs based on C–C coupling reactions not only has important academic value but also broad application prospects, which is of great significance for promoting the development of materials science and related industries. In the future, it is necessary to deeply clarify the internal mechanism of C–C coupling reactions through interdisciplinary integration, focus on the above four core bottlenecks, and make precise efforts to achieve coordinated breakthroughs: on the one hand, develop new synthesis strategies, efficient green catalytic systems, and precise structural regulation methods to solve the key problems in synthesis and structural regulation; on the other hand, strengthen the research on the structure–performance relationship of POPs materials to break through the limitations of large-scale production and application stability. Through continuous technological innovation and research accumulation, promote the industrial application of POPs materials in key fields such as energy storage, environmental governance, and biomedicine, and inject new momentum into the sustainable development of materials science and related industries.

## Author contributions

D. Liu and G. Zhu conceived and directed this work and revised the manuscript. Y. Li wrote the manuscript. J. Zhao revised the manuscript and offered suggestions.

## Conflicts of interest

There are no conflicts to declare.

## Data availability

No primary research results, software or code have been included and no new data were generated or analysed as part of this review.

## Acknowledgements

This work is partially supported by the National Natural Science Foundation of China (No. 22475035 and 22071021).

## Notes and references

1 Q. Hao, Y. Tao, X.-S. Ding, Y.-J. Yang, J. Feng, R.-L. Wang, X.-M. Chen, G.-L. Chen, X.-M. Li, H. OuYang, X.-L. Hu, J. Tian, B.-H. Han, G.-S. Zhu, W. Wang, F. Zhang, B.-E. Tan, Z.-T. Li, D. Wang and L.-J. Wan, *Sci. China Chem.*, 2023, **66**, 620–682.

2 J.-X. Jiang, F. Su, A. Trewin, C. D. Wood, N. L. Campbell, H. Niu, C. Dickinson, A. Y. Ganin, M. J. Rosseinsky, Y. Z. Khimyak and A. I. Cooper, *Angew. Chem., Int. Ed.*, 2007, **46**, 8574–8578.

3 T. Ben, H. Ren, S.-Q. Ma, D.-P. Cao, J.-H. Lan, X.-F. Jing, W.-C. Wang, J. Xu, F. Deng, J. M. Simmons, S.-L. Qiu and G.-S. Zhu, *Angew. Chem., Int. Ed.*, 2009, **48**, 9457–9460.

4 J. Y. Lee, C. D. Wood, D. Bradshaw, M. J. Rosseinsky and A. I. Cooper, *Chem. Commun.*, 2006, **25**, 2670–2672.

5 P. M. Budd, B. S. Ghanem, S. Makhseed, N. B. McKeown, K. J. Msayib and C. E. Tattershall, *Chem. Commun.*, 2004, **2**, 230–231.

6 A. P. Côté, A. I. Benin, N. W. Ockwig, M. O'Keeffe, A. J. Matzger and O. M. Yaghi, *Science*, 2005, **310**, 1166–1170.

7 P. Kuhn, M. Antonietti and A. Thomas, *Angew. Chem., Int. Ed.*, 2008, **47**, 3450–3453.

8 J.-S. Sun, L.-P. Jing, Y.-Y. Tian, F.-X. Sun, P. Chen and G.-S. Zhu, *Chem. Commun.*, 2018, **54**, 1603–1606.

9 J.-X. Jiang, F. Su, H. Niu, C. D. Wood, N. L. Campbell, Y. Z. Khimyak and A. I. Cooper, *Chem. Commun.*, 2008, **4**, 486–488.

10 Z. Xie, Y.-B. Wei, X.-Y. Zhao, Y. Li, S.-Y. Ding and L. Chen, *Mater. Chem. Front.*, 2017, **1**, 867–872.

11 S.-L. Wang, C.-X. Zhang, Y. Shu, S.-L. Jiang, Q. Xia, L.-J. Chen, S.-B. Jin, I. Hussain, A. I. Cooper and B.-E. Tan, *Sci. Adv.*, 2017, **3**, e1602610.

12 S. Zhou, T.-Y. Qiu, H. Wang, B.-Y. Tang, Y. Su, T.-H. Nan, J.-C. Dong, Z.-H. Wang, D.-T. Liu and G.-S. Zhu, *Chem. Sci.*, 2024, **15**, 10830–10837.

13 D.-Q. Yuan, W.-G. Lu, D. Zhao and H.-C. Zhou, *Adv. Mater.*, 2011, **23**, 3723–3725.

14 S. Mane, Y.-X. Li, X.-Q. Liu, M.-B. Yue and L.-B. Sun, *ACS Sustainable Chem. Eng.*, 2018, **6**, 17419–17426.

15 S. Zhou, Z.-L. Liu, P.-P. Zhang, H.-Z. Rong, T.-T. Ma, F.-C. Cui, D.-T. Liu, X.-Q. Zou and G.-S. Zhu, *Chem. Sci.*, 2022, **13**, 11126–11131.

16 R. S. Sprick, J.-X. Jiang, B. Bonillo, S.-J. Ren, T. Ratvijitvech, P. Guiglion, M. A. Zwijnenburg, D. J. Adams and A. I. Cooper, *J. Am. Chem. Soc.*, 2015, **137**, 3265–3270.

17 L. Chen, Y. Yang and D.-L. Jiang, *J. Am. Chem. Soc.*, 2010, **132**, 9138–9143.

18 C.-C. Dong, J. Yu, X. Tao, H.-G. Wang and G.-S. Zhu, *Adv. Funct. Mater.*, 2024, **34**, 2410372.

19 T.-T. Ma, B. Fu, H. Feng, Y.-X. Li, Y.-H. Zhai, Y.-Y. Tian, Z.-N. Li and Z.-M. Su, *Angew. Chem., Int. Ed.*, 2025, **64**, e202501412.

20 M.-X. Sun, G. Tan, Z.-L. Dou, J. Song, X.-T. Qu, Y.-Y. Tian and G.-S. Zhu, *Chem. Sci.*, 2025, **16**, 22119.

21 J. Song, H.-T. Lei, L. Lin, M.-X. Sun, X.-Y. Han, Z.-L. Dou, Y.-Y. Tian and G.-S. Zhu, *Chem. Sci.*, 2025, **16**, 6231.

22 X.-Y. Zong, H.-N. Mi, F. Chen, X.-F. Guan, Y.-H. Liu, W. Hu, N.-W. Li, C.-Z. Jiang, Y.-F. Lu, G.-S. Zhu, W. Yan and J.-J. Zhang, *Angew. Chem., Int. Ed.*, 2025, **64**, e202509085.

23 L. Jing, Z.-H. Wang, Y.-J. Xie, J.-T. Jia, D.-T. Liu and G.-S. Zhu, *Sci. China Chem.*, 2026, DOI: 10.1007/s11426-025-3046-2.

24 J.-X. Jiang, F. Su, A. Trewin, C. D. Wood, H. Niu, J. T. A. Jones, Y. Z. Khimyak and A. I. Cooper, *J. Am. Chem. Soc.*, 2008, **130**, 7710–7720.

25 J.-X. Jiang, A. Trewin, F.-B. Su, C. D. Wood, H.-J. Niu, J. T. A. Jones, Y. Z. Khimyak and A. I. Cooper, *Macromolecules*, 2009, **42**, 2658–2666.
26 H.-P. Ma, H. Ren, X.-Q. Zou, F.-X. Sun, Z.-J. Yan, K. Cai, D.-Y. Wang and G.-S. Zhu, *J. Mater. Chem. A*, 2013, **1**, 752–758.
27 J.-Z. Yan, H. Ren, H.-P. Ma, R.-R. Yuan, Y. Yuan, X.-Q. Zou, F.-X. Sun and G.-S. Zhu, *Microporous Mesoporous Mater.*, 2013, **173**, 92–98.
28 Z. Yan, Y. Yuan, Y.-Y. Tian, D. Zhang and G.-S. Zhu, *Angew. Chem., Int. Ed.*, 2015, **54**, 14215.
29 H.-P. Ma, H. Ren, X.-Q. Zou, S. Meng, F.-X. Sun and G.-S. Zhu, *Polym. Chem.*, 2014, **5**, 144–152.
30 R.-R. Yuan, H. Ren, Z.-J. Yan, A.-F. Wang and G.-S. Zhu, *Polym. Chem.*, 2014, **5**, 2266–2272.
31 X.-S. Shen, M. Faheem, Y. Matsuo, S. Aziz, X. Zhang, Y.-H. Li, J. Song, Y.-Y. Tian and G.-S. Zhu, *J. Mater. Chem. A*, 2019, **7**, 2507–2512.
32 H. Zhang, Q. Huang, W.-J. Zhang, C.-Y. Pan, J. Wang, C.-X. Ai, J.-T. Tang and G.-P. Yu, *ChemPhotoChem*, 2019, **3**, 645–651.
33 T. Ben, C.-Y. Pei, D.-L. Zhang, J. Xu, F. Deng, X.-F. Jing and S.-L. Qiu, *Energy Environ. Sci.*, 2011, **4**, 3991–3999.
34 H. Ren, T. Ben, F.-X. Sun, M.-Y. Guo, X.-F. Jing, H.-P. Ma, K. Cai, S.-L. Qiu and G.-S. Zhu, *J. Mater. Chem.*, 2011, **21**, 10348–10353.
35 M.-P. Li, H. Ren, F.-X. Sun, Y.-Y. Tian, Y.-L. Zhu, J.-L. Li, X. Mu, J. Xu, F. Deng and G.-S. Zhu, *Adv. Mater.*, 2018, **30**, 1804169.
36 C.-Y. Pei, T. Ben, Y. Cui and S.-L. Qiu, *Adsorption*, 2012, **18**, 375–380.
37 C.-Y. Pei, T. Ben, H. Guo, J. Xu, F. Deng, Z.-H. Xiang, D.-P. Cao and S.-L. Qiu, *Philos. Trans. R. Soc., A*, 2013, **371**, 20120312.
38 X.-M. Liu, Y.-H. Xu and D.-L. Jiang, *J. Am. Chem. Soc.*, 2012, **134**, 8738–8741.
39 Y.-Y. Liu, Z. Ao, Q.-Q. Xu, D.-R. Zhu, C. Chen, X.-B. Wang, J.-G. Luo and L.-Y. Kong, *Bioorg. Chem.*, 2019, **87**, 409–416.
40 Y. Yuan, F.-X. Sun, H. Ren, X.-F. Jing, W. Wang, H.-P. Ma, H.-J. Zhao and G.-S. Zhu, *J. Mater. Chem.*, 2011, **21**, 13498–13502.
41 S. Meng, X.-Q. Zou, C.-F. Liu, H.-P. Ma, N. Zhao, H. Ren, M.-J. Jia, J. Liu and G.-S. Zhu, *ChemCatChem*, 2016, **8**, 2393–2400.
42 L. Zhang, J.-S. Sun, F.-X. Sun, P. Chen, J. Liu and G.-S. Zhu, *Chem. Eur. J.*, 2019, **25**, 3903–3908.
43 J. Weber and A. Thomas, *J. Am. Chem. Soc.*, 2008, **130**, 6334–6335.
44 L. Chen, Y. Honsho, S. Seki and D.-L. Jiang, *J. Am. Chem. Soc.*, 2010, **132**, 6742–6748.
45 Y.-F. Xu, C. Zhang, P. Mu, N. Mao, X. Wang, Q. He, F. Wang and J.-X. Jiang, *Sci. China Chem.*, 2017, **60**, 1075–1083.
46 J. Xu, F.-T. Yu, J.-L. Hua, W.-Q. Tang, C. Yang, S.-Z. Hu, S.-L. Zhao, X.-S. Zhang, Z. Xin and D.-F. Niu, *Chem. Eng. J.*, 2020, **392**, 123694.
47 Q. Chen, J.-X. Wang, F. Yang, D. Zhou, N. Bian, X.-J. Zhang, C.-G. Yan and B.-H. Han, *J. Mater. Chem.*, 2011, **21**, 13554–13560.
48 Q. Chen, M. Luo, P. Hammershoj, D. Zhou, Y. Han, B. W. Laursen, C.-G. Yan and B.-H. Han, *J. Am. Chem. Soc.*, 2012, **134**, 6084–6087.
49 C.-J. Sun, P.-F. Wang, H. Wang and B.-H. Han, *Polym. Chem.*, 2016, **7**, 5031.
50 Q. Chen, D.-P. Liu, J.-H. Zhu and B.-H. Han, *Macromolecules*, 2014, **47**, 5926–5931.
51 J.-H. Zhu, Q. Chen, Z.-Y. Sui, L. Pan, J.-G. Yu and B.-H. Han, *J. Mater. Chem. A*, 2014, **2**, 16181.
52 Q. Chen, D.-P. Liu, M. Luo, L.-J. Feng, Y.-C. Zhao and B.-H. Han, *Small*, 2014, **10**, 308–315.
53 L.-J. Feng, Q. Chen, J.-H. Zhu, D.-P. Liu, Y.-C. Zhao and B.-H. Han, *Polym. Chem.*, 2014, **5**, 3081.
54 Y. Tao, H. Liu, H.-Y. Kong, X.-Y. Bian, B.-W. Yao, Y.-J. Li, C. Gu, X.-S. Ding, L.-F. Sun and B.-H. Han, *J. Am. Chem. Soc.*, 2024, **146**, 16511–16520.
55 D.-H. Yang, Y. Tao, X.-S. Ding and B.-H. Han, *Chem. Soc. Rev.*, 2022, **51**, 761.
56 W.-G. Lu, D.-Q. Yuan, D. Zhao, C. I. Schilling, O. Plietzsch, T. Muller, S. Bräse, J. Guenther, J. Blümel, R. Krishna, Z. Li and H.-C. Zhou, *Chem. Mater.*, 2010, **22**, 5964–5972.
57 N. Naz, M. H. Manzoor, S. M. G. Naqvi, U. Ehsan, M. Aslam and F. Verpoort, *Appl. Mater. Today*, 2024, **38**, 102198.
58 P. A. Held, H.-Y. Gao, L.-C. Liu, C. Mück-Lichtenfeld, A. Timmer, H. Mönig, D. Barton, J. Neugebauer, H. Fuchs and A. Studer, *Angew. Chem., Int. Ed.*, 2016, **55**, 9777–9782.
59 C. D. Wood, B. Tan, A. Trewin, H.-J. Niu, D. Bradshaw, M. J. Rosseinsky, Y. Z. Khimyak, N. L. Campbell, R. Kirk, E. Stöckel and A. I. Cooper, *Chem. Mater.*, 2007, **19**, 2034–2048.
60 C. D. Wood, B. Tan, A. Trewin, F. Su, M. J. Rosseinsky, D. Bradshaw, Y. Sun, L. Zhou and A. I. Cooper, *Adv. Mater.*, 2008, **20**, 1916–1921.
61 B.-Y. Li, R.-N. Gong, W. Wang, X. Huang, W. Zhang, H.-M. Li, C.-X. Hu and B.-E. Tan, *Macromolecules*, 2011, **44**, 2410–2414.
62 V. Rozyyev, D. Thirion, R. Ullah, J. Lee, M. Jung, H. Oh, M. Atilhan and C. T. Yavuz, *Nat. Energy*, 2019, **4**, 604–611.
63 M. R. Prinsell, D. A. Everson and D. J. Weix, *Chem. Commun.*, 2010, **46**, 5743–5745.
64 Y.-X. Cai, X. Qian and C. Gosmini, *Adv. Synth. Catal.*, 2016, **358**, 2427–2430.
65 Y.-J. Liu, S.-H. Xiao, Y. Qi and F. Du, *Chem.–Asian J.*, 2017, **12**, 673–678.
66 L. Zou, M.-L. Long, H.-B. Zhou, W. Zhu, K. Zhang, Y.-M. Chen and F. Xi, *Polymer*, 2015, **64**, 196–201.
67 J. S. M. Lee and A. I. Cooper, *Chem. Rev.*, 2020, **120**, 2171–2214.
68 C. Corgnale, B. Hardy, R. Chahine, R. Zacharia and D. Cossement, *Appl. Energy*, 2019, **250**, 333–343.
69 B. Weinberger and F. D. Lamari, *Int. J. Hydrogen Energy*, 2009, **34**, 3058–3064.
70 K. O'Malley, G. Ordaz, J. Adams, K. Randolph, C. C. Ahn and N. T. Stetson, *J. Alloys Compd.*, 2015, **645**, S419–S422.

71 D. A. Gómez-Gualdrón, Y. J. Colón, X. Zhang, T.-C. Wang, Y.-S. Chen, J. T. Hupp, T. Yildirim, O. K. Farha, J. Zhang and R. Q. Snurr, *Energy Environ. Sci.*, 2016, **9**, 3279–3289.
72 K. C. Kim, *Int. J. Energy Res.*, 2018, **42**, 1455–1468.
73 Y.-X. Sun, T. Ben, L. Wang, S.-L. Qiu and H.-A. Sun, *J. Phys. Chem. Lett.*, 2010, **1**, 2753–2756.
74 M. Errico, C. Madeddu, D. Pinna and R. Baratti, *Appl. Energy*, 2016, **183**, 958–968.
75 D. S. Firaha and B. Kirchner, *ChemSusChem*, 2016, **9**, 1591–1599.
76 D. Gómez-Díaz, A. Muñiz-Mouro, J. M. Navaza and A. Rumbo, *AIChE J.*, 2021, **67**, e17071.
77 Q.-H.-Y. Wang, L. Lin, L. Jiang, Z.-H. Wang, Y.-N. Zhang, Q.-C. Han, X. Huang, C.-Y. Zhu, J.-T. Jia, Z. Bian and G.-S. Zhu, *Chem. Sci.*, 2025, **16**, 15121–15128.
78 B. Kiskan and J. Weber, *ACS Macro Lett.*, 2012, **1**, 37–40.
79 Z.-H. Wang, L. Jiang, J.-T. Jia and G.-S. Zhu, *Angew. Chem., Int. Ed.*, 2025, **64**, e202420746.
80 R. Dawson, D. J. Adams and A. I. Cooper, *Chem. Sci.*, 2011, **2**, 1173–1177.
81 Y.-H. Lin, J.-C. Dong, Q. Zhou, H. Zhang, H.-C. Jiang, Z.-Y. Wang, X. Zhao, G.-J. Ren, Q.-H. Pan, G.-S. Zhu and X.-Q. Zou, *Angew. Chem., Int. Ed.*, 2025, **64**, e202519421.
82 Y. Ma, F.-C. Cui, H.-Z. Rong, J. Song, X.-F. Jing, Y.-Y. Tian and G.-S. Zhu, *Angew. Chem., Int. Ed.*, 2022, **61**, e202113682.
83 X.-B. Liu, G.-S. Zhu, M.-Y. Li, H.-Z. Xing, S.-Y. Zhu, X. Liu and G.-S. Zhu, *Angew. Chem., Int. Ed.*, 2024, **63**, e202412408.
84 Z.-H. Wang, C. Cao, L. Jiang, Z.-H. Xing, J.-T. Jia and G.-S. Zhu, *Angew. Chem., Int. Ed.*, 2025, **64**, e202508924.
85 Y.-Q. Li, T. Ben, B.-Y. Zhang, Y. Fu and S.-L. Qiu, *Sci. Rep.*, 2013, **3**, 2420.
86 R. S. Sprick, B. Bonillo, M. Sachs, R. Clowes, J. R. Durrant, D. J. Adams and A. I. Cooper, *Chem. Commun.*, 2016, **52**, 10008–10011.
87 W.-J. Zhang, J.-T. Tang, W.-G. Yu, Q. Huang, Y. Fu, G.-C. Kuang, C.-Y. Pan and G.-P. Yu, *ACS Catal.*, 2018, **8**, 8084–8091.
88 Y.-F. Xu, N. Mao, C. Zhang, X. Wang, J.-H. Zeng, Y. Chen, F. Wang and J.-X. Jiang, *Appl. Catal., A*, 2018, **228**, 1–9.
89 V. R. Battula, H. Singh, S. Kumar, I. Bala, S. K. Pal and K. Kailasam, *ACS Catal.*, 2018, **8**, 6751–6759.
90 H.-J. Hou, X.-H. Zhang, D.-K. Huang, X. Ding, S.-Y. Wang, X.-L. Yang, S.-Q. Li, Y.-G. Xiang and H. Chen, *Appl. Catal., B*, 2017, **203**, 563–571.
91 L.-Z. Cao, C. Wang, H. Wang, X.-M. Xu, X. Tao, H.-Q. Tan and G.-S. Zhu, *Angew. Chem., Int. Ed.*, 2024, **63**, e202402095.
92 X.-M. Xu, H. Wang, Z.-W. Zhang, J.-L. Li, X.-M. Liu, X. Tao and G.-S. Zhu, *Nano*, 2024, **16**, 11138–11145.
93 H. Wang, L.-Z. Cao, X. Tao and G.-S. Zhu, *Angew. Chem., Int. Ed.*, 2025, **64**, e202502943.
94 Y.-X. He, L.-Z. Cao, H. Wang, F.-C. Cui and X. Tao, *Chem. Commun.*, 2025, **61**, 9892–9895.
95 J.-J. Shao, H. Wang, X. Tao and G.-S. Zhu, *Chem. Sci.*, 2025, **16**, 13267–13275.
96 Y.-T. Yang, Y. Xiao, L. Jiang, J.-H. Li, J.-L. Li, J.-T. Jia, C. T. Yavuz, F.-C. Cui, X.-F. Jing and G.-S. Zhu, *Adv. Mater.*, 2024, **36**, 2404791.
97 Y. Su, Z.-M. Wang, A. Legrand, T. Aoyama, N. Ma, W.-T. Wang, K.-I. Otake, K. Urayama, S. Horike, S. Kitagawa, S. Furukawa and C. Gu, *J. Am. Chem. Soc.*, 2024, **146**, 15479–15487.
98 B. Chen, B. Li, Y. Su, J.-L. Zhu, M. Gao, S.-H. Xiong, P. Wang, Z.-M. Wang, Q. Liao and C. Gu, *Angew. Chem., Int. Ed.*, 2025, **64**, e202515924.
99 Y. Su, B. Li, H. Xu, C.-Y. Lu, S.-D. Wang, B. Chen, Z.-M. Wang, W.-T. Wang, K.-I. Otake, S. Kitagawa, L.-B. Huang and C. Gu, *J. Am. Chem. Soc.*, 2022, **144**, 18218–18222.
100 Y. Su, Z.-M. Wang, A. Legrand, T. Aoyama, N. Ma, W.-T. Wang, K.-I. Otake, K. Urayama, S. Horike, S. Kitagawa, S. Furukawa and C. Gu, *J. Am. Chem. Soc.*, 2022, **144**, 6861–6870.
101 L. Chen, Y. Yang, Z.-Q. Guo and D.-L. Jiang, *Adv. Mater.*, 2011, **23**, 3149–3154.
102 Z.-G. Xie, C. Wang, K. E. Krafft and W.-B. Lin, *J. Am. Chem. Soc.*, 2011, **133**, 2056–2059.
103 J.-L. Wang, C. Wang, K. E. Krafft and W.-B. Lin, *ACS Catal.*, 2012, **2**, 417–424.
104 J.-X. Jiang, C. Wang, A. Laybourn, T. Hasell, R. Clowes, Y. Z. Khimyak, J.-L. Xiao, S. J. Higgins, D. J. Adams and A. I. Cooper, *Angew. Chem., Int. Ed.*, 2010, **50**, 1072–1075.
105 X. Du, Y.-L. Sun, B. Tan, Q.-F. Teng, X.-J. Yao, C.-Y. Su and W. Wang, *Chem. Commun.*, 2010, **46**, 970–972.
106 Y. Zhang, Y. Zhang, Y.-L. Sun, X. Du, J.-Y. Shi, W.-D. Wang and W. Wang, *Chem. Eur. J.*, 2012, **18**, 6328–6334.
107 L.-J. Feng, Q. Chen, J.-H. Zhu, D.-P. Liu, Y.-C. Zhao and B.-H. Han, *Polym. Chem.*, 2014, **5**, 3081–3088.
108 J.-Y. Zhao, X.-L. Wang, B.-Y. Tang, Y.-F. Li, D.-T. Liu and G.-S. Zhu, *J. Energy Chem.*, 2026, **114**, 536–545.
109 Y. Su, X.-L. Wang, M.-H. Zhang, H.-M. Guo, H.-Z. Sun, G. Huang and G.-S. Zhu, *Angew. Chem., Int. Ed.*, 2023, **62**, e202308182.
110 S. Zhou, Y. Su, G.-P. Li, X.-L. Wang, D.-T. Liu and G.-S. Zhu, *Colloids Surf., A*, 2023, **661**, 130960.
111 J. Yu, X.-P. Zhang, Y.-Y. Liu, L.-Q. Cheng, H.-G. Wang, F.-C. Cui and G.-S. Zhu, *Angew. Chem., Int. Ed.*, 2025, **64**, e202507570.
112 L.-Y. Yin, X.-Y. Guo, J.-F. Hu, K.-M. Yan, L. Liu, X.-Y. Shi, F.-C. Cui, G.-S. Zhu and N. Zhang, *Angew. Chem., Int. Ed.*, 2025, **64**, e202423265.
113 J.-H. Wang, X.-P. Zhang, Z.-L. Liu, J. Yu, H.-G. Wang, X.-L. Wu, F.-C. Cui and G.-S. Zhu, *Angew. Chem., Int. Ed.*, 2024, **63**, e202401559.
114 L. Liu, R.-H. Yu, L.-Y. Yin, N. Zhang and G.-S. Zhu, *Chem. Sci.*, 2024, **15**, 1924–1937.
115 E. Merino, E. Verde-Sesto, E. M. Maya, A. Corma, M. Iglesias and F. Sánchez, *Appl. Catal., A*, 2014, **469**, 206–212.
116 C.-C. Dong, J. Chu, L.-Z. Cao, F.-C. Cui, S. Liang, X.-T. Zhang, X. Tao, H.-G. Wang and G.-S. Zhu, *CCS Chem.*, 2023, **5**, 607–615.
117 H. Chen, J.-T. Fan, Y.-Q. Fu, C. L. Do-Thanh, X. Suo, T. Wang, I. Popovs, D.-D. Jiang, Y.-T. Yuan, Z.-Z. Yang and S. Dai, *Adv. Mater.*, 2021, **33**, 2008685.

118 C.-Z. Liu, Y.-H. Liu, L.-Y. Wang, Y.-T. Liu, H.-Y. Huo, S.-Y. Li, Z.-Y. Sun, W. Hu, Y.-F. Lu and G.-S. Zhu, *J. Energy Chem.*, 2025, **110**, 703–711.
119 T.-T. Ma, Z.-N. Li, R.-Y. Ma, H. Feng, Y.-H. Zhai, Z. Gao, Y.-Y. Tian and Z.-M. Su, *ACS Energy Lett.*, 2024, **9**, 4009–4017.
120 J.-F. Hu, Z.-F. Zhang, T. Deng, F.-C. Cui, X.-Y. Shi, Y.-Y. Tian and G.-S. Zhu, *Adv. Mater.*, 2024, **36**, 2401091.
121 J. Chu, Z.-L. Liu, J. Yu, L.-Q. Cheng, H.-G. Wang, F.-C. Cui and G.-S. Zhu, *Angew. Chem., Int. Ed.*, 2023, **63**, e202314411.
122 Y.-G. Jing, C. Wang, L. Chen, L. Liu, L.-Y. Yin, F.-C. Cui, N. Zhang, S.-P. Wen and G.-S. Zhu, *Angew. Chem., Int. Ed.*, 2023, **62**, e202301234.
123 D. Xie, Y. Sang, D.-H. Wang, W.-Y. Diao, F.-Y. Tao, C. Liu, J.-W. Wang, H.-Z. Sun, J.-P. Zhang and X.-L. Wu, *Angew. Chem., Int. Ed.*, 2022, **62**, e202216934.
124 J.-Y. Zhao, M.-H. Zhang, H.-M. Guo, X.-L. Wang and D.-T. Liu, *Rare Met.*, 2025, **44**, 6115–6124.
125 H.-G. Wang, Q. Wu, L.-Q. Cheng and G.-S. Zhu, *Coord. Chem. Rev.*, 2022, **472**, 214772.
126 Y.-Z. Guo, L.-Q. Cheng, X.-P. Zhang, M.-L. Qi, Y.-B. Wei, H. Sheng, X. Su, H.-G. Wang and L. Chen, *Angew. Chem., Int. Ed.*, 2025, **64**, e202510604.
127 Y. Sun, S.-Q. Li, G.-P. Li, Y. Su, M.-F. Sun, X.-L. Wang, J.-X. Wang, W.-S. Yu, X.-T. Dong and D.-T. Liu, *Chem. Eng. J.*, 2025, **524**, 169752.
128 S.-Q. Li, J.-X. Deng, Y. Sun, Y. Su, J.-X. Wang, W.-S. Yu, X.-T. Dong, D.-T. Liu and X.-L. Wang, *Mater. Today Chem.*, 2026, **52**, 103370.
129 X.-Q. Fu, G.-P. Li, Y. Su, M.-F. Sun, X.-L. Wang, J.-X. Wang, W.-S. Yu, X.-T. Dong and D.-T. Liu, *J. Energy Chem.*, 2024, **88**, 125–143.
130 G.-P. Li, X.-L. Wang, S.-H. Lv, J.-X. Wang, W.-S. Yu, X.-T. Dong and D.-T. Liu, *Adv. Funct. Mater.*, 2023, **33**, 2208288.